UNIVERSITY OF CALIFORNIA

Los Angeles

A Study of Hadronic Shower Punchthrough Originating From Incident Hadrons With Momentum From 10 to 300 GeV/c

A dissertation submitted in partial satisfaction of the
requirements for the degree Doctor of Philosophy
in Physics

by

David Aubrey Chrisman

1995

The dissertation of David Aubrey Chrisman is approved.

Edward J. Hoffman

Thomas Müller

Charles Whitten

Muzaffer Atac, Committee Co-Chair

David B. Cline, Committee Co-Chair

University of California, Los Angeles

1995

DEDICATION

Contents

List of Figures

List of Tables

ACKNOWLEDGMENTS

I have had the good fortune and honor to do my post graduate studies at UCLA and I would like to thank all the professors and students who have helped me along the way. In particular, I am grateful to my co-advisor Muzaffer Atac for all he taught me during our many hours in the laboratory together. I am also indebted to my other co-advisor David B. Cline, for giving me an opportunity of a lifetime, to come and complete my post doctoral research at CERN. Professor Cline has been an enthusiastic supporter of RD5 from its inception and also of my research as a part of RD5.

I was also fortunate to collaborate with Jun Park on research devoted to developing a scintillating fiber tracking system. The results of that research, presented in an appendix to this dissertation, would not have been possible without his guidance and hard work.

My thanks go to Jim Kolonko, for all the work he does to keep our group running smoothly.

I am indebted to Stanislaw Otwinowski, a UCLA colleague stationed at CERN, for his guidance and friendship. Stan was helpful from the very first day I arrived in Geneva. We have had many interesting and fruitful discussions concerning my research and he was kind enough to proofread much of this dissertation.

I would like to express my gratitude to all my colleagues in the RD5 collaboration who contributed so much of their time and effort to this research. From the very beginning I felt welcome in the collaboration and only have good memories of all the work we have done together. I thank especially, Ernst Radermacher, who's constant leadership and support was invaluable. The contributions of the following people are enthusiastically acknowledged: Gyorgy Bencze, Anna Di Ciaccio, Roger McNeil,

Mohammad Mohammadi and Hans Reithler. I am also grateful to Carmen Albajar, Chris Lyndon and Paul Porth, for their expert simulation of the RD5 detector.

I deeply appreciate the generosity and patience of Grzegorz Wrochna, who contributed substantially to this research. He was always able to find time in his busy day to discuss this research and help solve whatever problem was at hand.

Much of this research would not have been completed without the help of my collaborator and friend Thomas Moers. Thomas and I worked together on the RD5 data analysis and the simulation of the CMS detector.

A special thanks goes to my *chere amie* Carine Diver, for all the happy times we have shared together. Meeting Carine is the most exciting discovery I have made (scientific or otherwise) since coming to CERN.

[redacted].

VITA

May, 1989	B.S. Physics University of California Los Angeles, California
1989-1992	Research Assistant (at UCLA) University of California Los Angeles, California
1992	M.S., Physics University of California Los Angeles, California
1992-Present	Research Assistant (at CERN) University of California Los Angeles, California on the RD5 Experiment

PUBLICATIONS

"Electromagnetic Secondaries in the Detection of High Energy Muons" C. Albajar *et al* , **CERN PPE/94-204**, *Submitted to Zeitschrift für Physik C*

"Beam Test of a 12-layer Scintillating-Fiber Charged-Particle Tracking System", B. Abbott *et al* , Nucl. Instr. and Meth. **A339** (1994) 155-160.

"Measurement of Hadron Shower Punchthrough in Iron", M. Aalste *et al* , Zeitschrift für Physik **C60** (1993) 1-10.

"Tracking with Scintillating Fibers and Visible Light Photon Counters", M. Atac *et al* , Nucl. Instr. and Meth. **A320** (1992) 155-160.

"Scintillating Fiber Tracking at the SSC Using Visible Light Photon Counters", M. Atac *et al* , Nucl. Instr. and Meth. **A314** (1992) 56-62.

"Development of a High Resolution Scintillating Fiber Gamma Ray Telescope", P. Antich *et al* , Nucl. Instr. and Meth. **A297** (1990) 514-520.

ABSTRACT OF THE DISSERTATION

A Study of Hadronic Shower Punchthrough Originating From Incident Hadrons With Momentum From 10 to 300 GeV/c

by

David Aubrey Chrisman

Doctor of Philosophy in Physics

University of California, Los Angeles, 1995

Professor Muzaffer Atac, Co-chair

Professor David B. Cline, Co-chair

Muons will provide the experimental signature for many of the most interesting and rare physical processes to be studied at future hadron colliders, such as the LHC. Particles originating from hadronic shower punchthrough will be a major source of background to the muon signal in LHC experiments. A detailed characterization of muon backgrounds and a deep understanding of processes which obscure the accurate measurement of muons is therefore essential, first in the design of such experiments and then later in the analysis of data.

A detailed study of hadronic shower punchthrough was conducted by the RD5 collaboration at CERN. The RD5 detector was designed to simulate a slice of a typical collider detector, thus mimicking the experimental environment which will

be encountered at the LHC. The RD5 detector is composed of tracking detectors, a calorimeter (10λ absorber thickness) and a muon spectrometer. The calorimeter was installed inside a superconducting magnet, with a maximum 3 T field, in order to investigate the effect of a strong magnetic field on hadronic punchthrough.

The total punchthrough probability of hadronic showers, as a function of absorber depth, and the momentum and angular spectrum of punchthrough muons, was measured for several different types of incident hadron (π^-, π^+, K^+ and p) and wide range of incident hadron momenta (10 to 300 GeV/c). Measurements were made with the absorber in a magnetic field ranging from 0 to 3 T.

The measurement of total punchthrough reached a depth of 31λ, farther than measured by previous experiments. The momentum and angular spectrum was measured for punchthrough muons which reached to at least 20λ. The momentum resolution ($\Delta p/p$) ranged from -8.5%, $+10\%$ at 30 GeV/c, to -18%, $+27\%$ at 300 GeV/c. The angular resolution was about 1 mrad. The momentum was given for a reference plane at 10λ. The measurements were compared with a GEANT-based simulation of the RD5 detector.

The general agreement between the simulation and all aspects of the punchthrough study in RD5 gave us confidence that this simulation could be used to make accurate predictions when applied to the design of a LHC detector. A simulation study of the CMS detector was conduced to predict the impact of several sources of background muons on the CMS muon system.

Chapter 1

Introduction

The science of Elementary Particle Physics is concerned with describing Nature at its most fundamental level, to discover the fundamental building blocks of matter and to describe the forces which mediate their interactions. This approach has historically sought to describe Nature from the bottom up, so to speak, by explaining complex and disparate natural phenomena in terms of theories based on a small set of fundamental laws. Looking back over the centuries, one can imagine that this progression towards a correct and comprehensive theory of Nature is like marching up a tall mountain, with brilliant men and women stationed along the path to show us the way, men and women who were able to go beyond the wisdom they were taught and imagine how Nature *might* be. From our experience with walking in the mountains, however, it is well known that whenever we think we have made it to top of the trail and can begin our easy decent, there is actually another even taller peak waiting for us just ahead. We particle physicists may be at such a point in our journey of understanding.

The Standard Model (SM) of electroweak and strong interactions describes all known elementary particle phenomena. This model is a great success and has been confirmed by all existing experimental evidence. This theory has been tested with

high accuracy at the e^+e^- colliders LEP, at CERN, and SLC, at the Stanford Linear Collider Center (SLAC). The CDF collaboration at FNAL has recently reported experimental evidence for the Top quark, one of the last undiscovered particles in the SM. This evidence has provided further support for this model. However, in spite of all the success of the SM, the opinion among many physicists is that, because it still leaves many unanswered questions and leads to some contradictions when its predictions are extrapolated to higher energies, it is probably far from being an ultimate theory of Nature.

It is frequently stated that the SM contains 21 free parameters, that is, there are 21 parameters which must be determined by measurement and are not derived from the underlying theory. Among these 21 parameters are the lepton and quark masses. We do not know why there are 3 generations of quarks and leptons. Is electroweak symmetry breaking correctly described by the postulated Higgs mechanism? What is the nature of the Dark Matter in the universe? We cannot begin to answer these questions until we make new measurements at higher energies. The goal of the Large Hadron Collider (LHC), which is currently being built at CERN, is to provide these data by extending our observations into a realm of unprecedented high energy.

1.1 Objectives and Outline of this Dissertation

The purpose of this dissertation is to describe in detail the properties of hadronic shower punchthrough. Particles originating from hadronic punchthrough will be a major source of background to the muon signal at the LHC. Muons will provide the experimental signature for many of the most important and rare physical processes to be studied at the LHC; consequently, a deep understanding of muon backgrounds and processes which will obscure the accurate measurement of muons is essential, first

for the design of such experiments, and then later in the analysis of data.

In order to set the stage for this investigation, a brief description of the SM will be presented. This is followed by a description of the LHC and a description of the search for the Higgs boson, which will illustrate the importance of measuring final state muons. Next, we describe the Compact Muon Solenoid (CMS), one of the general purpose collider detectors being built at the LHC.

In Chapter 2, a discussion of the prompt muon signal and of several different sources of background muons will be discussed. In Chapter 3, the measurement of hadronic shower punchthrough in experiment RD5 is described. This includes a description of the data sample, the analysis method and the Monte Carlo simulation of the RD5 detector. This dissertation is concluded, in Chapter 4, by a Monte Carlo simulation study of charged particle backgrounds affecting the performance of the CMS muon system. The simulation results are compared with the experimental results of RD5 wherever possible.

When work on this dissertation began, the design and construction of the Superconducting Super Collider (SSC) was well underway and research and development on the detector subsystems to be employed there was progressing. In Appendix A, we describe research which was performed to develop a scintillating fiber tracking system for the Solenoid Detector Collaboration (SDC).

1.2 The Standard Model

In the Standard Model [1] matter is composed of elementary fermions, called leptons and quarks. These particles are considered elementary in the sense that they themselves cannot be subdivided. These particles interact via three forces: electromagnetic, weak and strong. These forces are mediated by a set of particles called

bosons, which are also considered elementary. The gravitational force has not yet been integrated into the SM, however, the weakness of the gravitational force, relative to the other forces in the SM, makes its effect negligible when we consider elementary particle interactions in our laboratories.

1.2.1 Elementary Particles and Interactions

The leptons and quarks are spin $\frac{1}{2}$ fermions which are grouped into three families, 2 leptons and 2 quarks per family (see Table 1.1). We don't know why there is more than one family, however, limits on the number of families have been set by experiments at LEP. From direct searches for new heavy quarks and leptons, it was found that, if fourth generation particles exist, their mass should be greater then $m_Z/2$. Also at LEP, by measuring the width of the Z^0, the number of light neutrinos (N_ν) have been "counted", there being one neutrino per family. The current result is $N_\nu = 2.983 \pm 0.025$ [2]. Evidence for the Top quark (t), the last quark in the SM to be discovered, was recently reported by the CDF collaboration at FNAL [3].

Table 1.1: The elementary quarks and leptons are grouped into 3 families.

	1	2	3	charge
leptons	ν_e	ν_μ	ν_τ	0
	e	μ	τ	-1
quarks	u	c	t	$+\frac{2}{3}$
	d	s	b	$-\frac{1}{3}$

The three fundamental interactions in the SM are mediated by spin 1 gauge bosons. The massless photon (γ) couples to the electromagnetic current and is the quantum of the electromagnetic field. There are three massive gauge bosons ($W^\pm, Z^0$)

mediating the weak interaction. The strong interaction is mediated by eight massless gluons which couple to the color charge.

Electromagnetism has been understood on the classical level since the mid 19th century due to the work of Maxwell. Electromagnetic interactions among elementary particles are described precisely by a gauge theory called Quantum Electrodynamics (QED) [4]. All particles which carry electric charge couple to the electromagnetic field. This interaction is responsible for most of the phenomenon we experience in our daily life: heat, light, radio signals, electricity, chemistry, almost every common phenomenon except gravity.

Theories of the weak interaction date back to the work of Fermi in the 1930's. The original model for the weak interaction was the so-called 4-fermion interaction [5] which accurately described processes at low energy, for example nuclear beta decay. However, this theory of a point like interaction broke down when its predictions were extrapolated to higher energies. In the modern theory of weak interactions (the electroweak theory of Glashow, Salam and Weinberg [6]), the 4-fermion interaction is replaced by the exchange of the massive Intermediate Vector Bosons (IVB) ($W^{\pm} \approx 80\,\mathrm{GeV}/c^2$, $Z^0 \approx 91\,\mathrm{GeV}/c^2$). This theory makes correct predictions concerning weak processes which occur at high energy and also provides a mechanism by which QED and the weak interaction are unified into an *electroweak* interaction.

In Table 1.1, the particles in each family are arranged in doublets of a quantum number called *weak isospin.* In the electroweak theory, the charged IVBs ($W^{\pm}$) induce transitions within a weak isospin doublet. In the case of leptons, the transitions are straightforward; for example, a muon will decay into a muon neutrino and a virtual W, the interaction being confined to one family. The charged current interaction among quarks is complicated by the fact that the weak isospin eigenstates are a mixture of the

physical mass eigenstates. As a consequence of this mixing, inter-family transitions among quarks can occur, for example, a charm quark (c) can decay into either a strange (s) or a down (d) quark. The probability for such transitions is contained in the Cabibbo, Kobayashi, Maskawa (CKM) [7] matrix. The degree to which this inter-family mixing occurs is not predicted by the theory and must be determined experimentally. The neutral IVB, Z^0, mediates the neutral current interactions, for example, $\nu_\mu e^- \rightarrow \nu_\mu e^-$. Inter-family neutral current transitions are suppressed by the Glashow-Iliopoulos-Maiani (GIM) mechanism. There are no tree-level flavor-changing (inter-family) neutral current interactions observed in Nature.

In the 1970's, a gauge theory describing the strong interaction was developed called Quantum Chromodynamics (QCD) [8]. The "charge" in QCD is *color*, of which there are three kinds, frequently called red, blue and green, as well as three anti-colors appropriately called anti-red, anti-blue and anti-green. One of the main differences between quarks and leptons is that quarks are subject to all the interactions, including the strong force, while the leptons are not subject to the strong force. The strong interaction is mediated by 8 massless gluons. The gluons also carry color charge and can therefore interact among themselves. Color seems to be absolutely conserved and confined within a region of space of dimension $\sim$ 1fm. No free colored objects have ever been observed. Hadrons are colorless bound states of quarks. A combination of color and anti-color or of three complementary colors form a color neutral "white" state. The $q\bar{q}$ states are called mesons; the qqq states are called baryons.

One of the main unanswered questions within the SM, is that of the actual mechanism for symmetry breaking in electroweak phenomenon. Within the electroweak theory, the Higgs Mechanism [9] was invented to account for the masses of the vector bosons and also to cancel divergences that occur in the scattering cross-section of lon-

gitudinally polarized IVBs, when extrapolated to high energies. The theory requires at least one Higgs particle, but there may be more. The interactions of the Higgs particle, as well as its width for a given mass, can be predicted, but its mass cannot.

1.3 The Large Hadron Collider

The search for the SM Higgs is one of the primary motivations for constructing the Large Hadron Collider (LHC). The current limit on the Higgs mass, set by experiments at LEP, is $m_{\mathrm{H}} > 60\,\mathrm{GeV}$ [10]. An upper bound can be set by theoretical arguments. If the Higgs mass is too large then the WW scattering amplitude violates the unitarity limit. This suggests that if the SM can be described by "simple" perturbation theory, then $m_{\mathrm{H}} < 1.2\,\mathrm{TeV}$ [11].

The LHC will be built in the existing LEP tunnel at CERN. The circumference of the tunnel is about 26.7 km. Two proton beams will be accelerated and collided head on with a center of mass energy of 14 TeV. The peak collision energy is dictated by the maximum possible magnetic field strength which will hold the protons in their orbit. Using superconducting magnets, with fields of 8.36 Tesla, will allow proton beams to be accelerated up to 7 TeV, per proton. The maximum luminosity will be $10^{34}\ \mathrm{cm}^{-2}\mathrm{s}^{-1}$. The high collision center of mass energy and high luminosity are required in order to create massive particles which have small production cross-sections relative to the cross-sections of background processes.

A proton circulating in the LHC can be thought of as being a broad band beam of quarks, antiquarks and gluons, where the total particle momentum is shared among the proton constituents. Therefore, multi-TeV proton beams will be required in order to reach constituent collision energies well above 1 TeV, and thus have enough energy available to produce Higgs bosons at the upper end of the expected mass range.

Figure 1.1 shows the energy dependance of some characteristic production cross-sections and event rates we expect at the LHC. We see the production cross-section for the Higgs boson ($m_H = 500\,GeV$) is 11 orders of magnitude below the total cross-section. The high luminosity allows the detection of rare Higgs decay modes, characterized by event signatures which are easily distinguishable from the enormous background. Also, at high luminosity, we can benefit from rare collisions where colliding constituents take a relatively large fraction of the energy of the proton, thus, for a given beam energy, high luminosity extends the effective energy in the constituent frame.

1.3.1 Standard Model Higgs Search at the LHC

In the years before the start of the LHC, the energy of the LEP beams will be increased. The maximum center of mass energy for e^+e^- collisions at LEP 200 will be about 176 GeV. If it turns out that $m_H \leq m_Z$, the Higgs boson may be found at LEP 200. The mass range $m_H > m_Z$ is where the search is taken over by LHC experiments.

The Higgs coupling to other particles is proportional to their mass; therefore, in its production and decay, the Higgs coupling to the heaviest available particle will predominate. Feynman diagrams of the dominant Higgs productions mechanisms, in p-p collisions at the LHC, are shown in Figure 1.2. The Higgs boson is produced through gluon-gluon fusion, via a virtual t quark loop, or through WW/ZZ fusion.

In the low mass region ($90\,GeV < m_H < 130\,GeV$) the largest Higgs decay branching ratio is into $b\bar{b}$. However, at the center of mass energy and high luminosity planned for the LHC this decay mode will surely be overwhelmed by the QCD $b\bar{b}$ pair-production background (see Figure 1.1). It is a general feature of the Higgs search

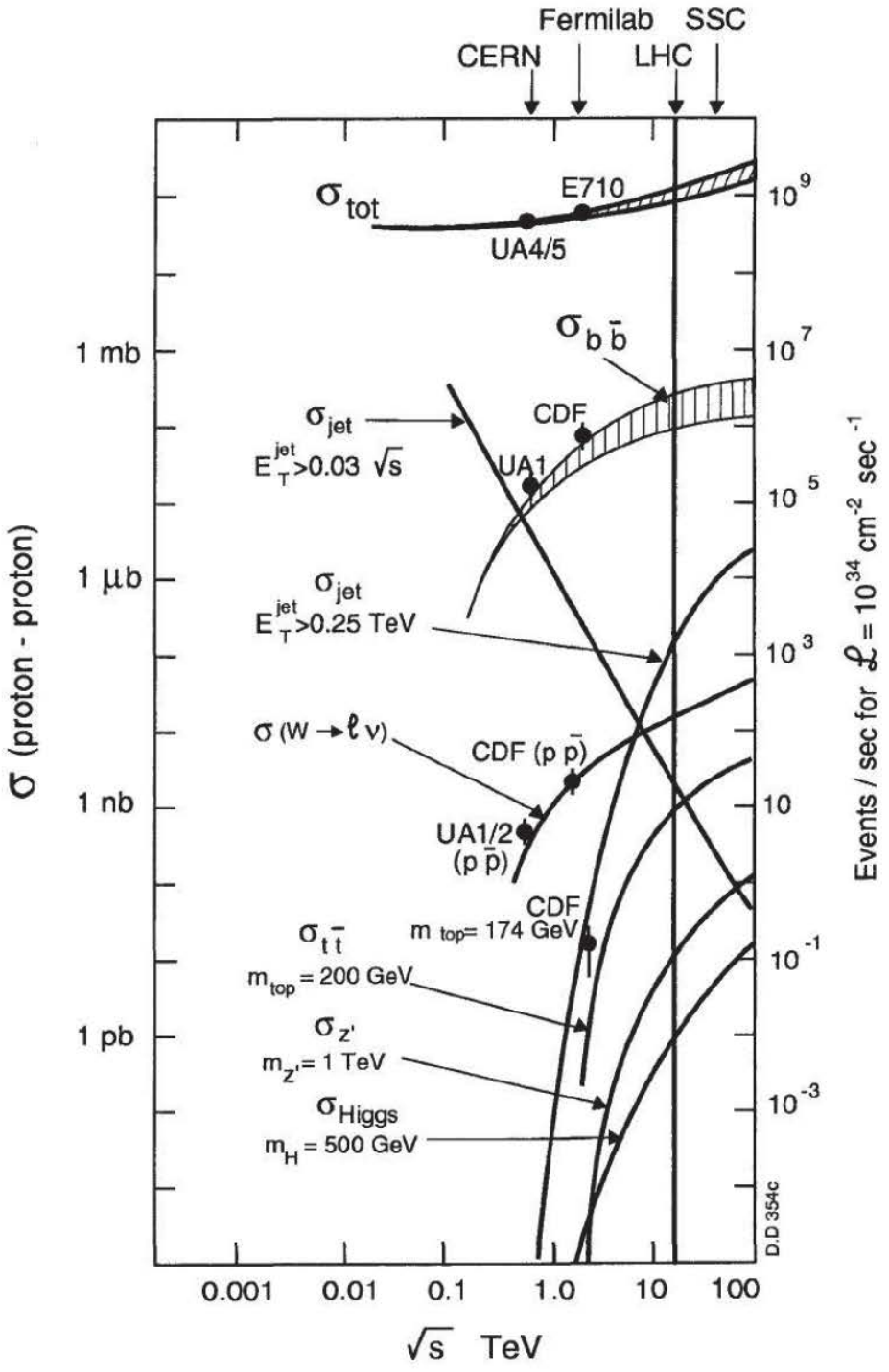

Figure 1.1: Cross-sections and event rates at hadron colliders.

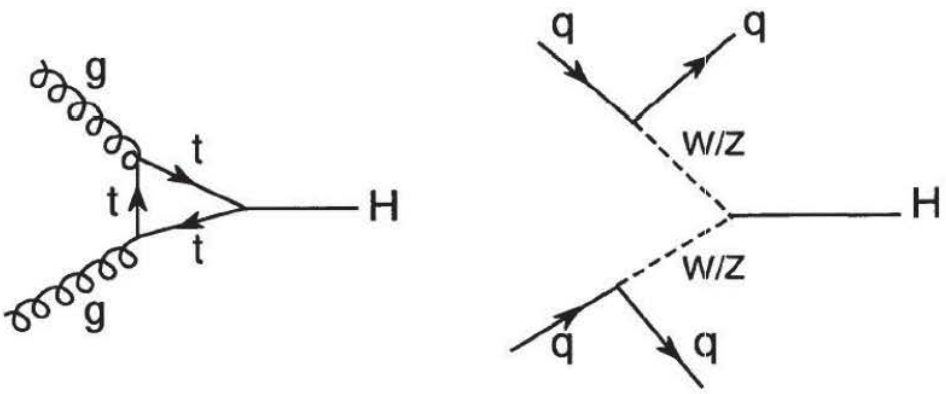

Figure 1.2: Feynman diagrams of the dominant Higgs productions mechanisms in p-p collisions at the LHC: gluon-gluon fusion, via a virtual t quark loop, (left diagram) and WW/ZZ fusion (right diagram).

at the LHC, in the intermediate and high mass range as well, that the hadronic final states of the Higgs boson will be very difficult to separate from backgrounds. For the low mass Higgs, H$\rightarrow \gamma\gamma$ is expected to be the most favorable search channel. Due to high photon backgrounds this will be a difficult experiment and will require an excellent electromagnetic calorimeter to be successful.

In the intermediate mass range (130 GeV $< m_{\mathrm{H}} < 2m_{\mathrm{Z}}$) the decay mode, H$\rightarrow$ZZ* $\rightarrow$ $4l^{\pm}$, looks most promising. The Higgs decays into an on-shell Z and an off-shell Z, with each Z boson decaying into two leptons, muons or electrons. The main backgrounds are from $t\bar{t}$ and Zb$\bar{\mathrm{b}}$ production.

The high mass range ($m_{\mathrm{H}} > 2m_{\mathrm{Z}}$) is expected to be the easiest mass range for detection of the Higgs boson. Here again we search for final state leptons (H$\rightarrow$ZZ$\rightarrow$ $4l^{\pm}$) requiring that the leptons form two oppositely charged pairs and that each pair have an effective mass within a specified window centered on m_{Z}. This requirement reduces the non-resonant background coming from $t\bar{t}$ production. The largest remaining

background comes from SM ZZ production.

For a Higgs mass of 500 GeV and luminosity of $10^{34}\text{cm}^{-2}\text{s}^{-1}$ it is estimated that $\sim 10^5$ Higgs will be produced per year. However, the decay channel most favorable for its discovery, $H \rightarrow ZZ \rightarrow 4\mu^{\pm}$, has a small branching ratio ($R \approx 3 \times 10^{-4}$). Therefore, searches for this most favorable decay mode may still be limited by statistics even at the highest luminosities.

If the Higgs boson is not found at the LHC this does not mean the experiment was not a success. The Higgs mechanism just happens to be the most widely agreed upon theoretical guess to account for the electroweak symmetry breaking. As previously mentioned, from a phenomenological analysis of WW scattering at high energy, it was found that, in the absence of a Higgs boson, the perturbative cross-section violates unitarity at energies on the order of 1 TeV. This is due to the growth of the longitudinal scattering amplitudes. Therefore, if the Higgs is not found, some new physics phenomenon, for example a new interaction which fulfils the role of the Higgs, must happen in the 1 TeV energy range.

The search for the SM Higgs is by no means the only physics of interest to be explored at the LHC. Other areas of interest include Supersymmetry (including Supersymmetric Higgs particles), search for new heavy vector bosons, study of the top quark, and b-physics, including measurement of CP violation in the B^0-$\overline{B}^0$ system and searches for rare B-decays, to name only a few. A detailed review of the physics potential of the LHC can be found in reference [12].

1.4 The Compact Muon Solenoid

There are two general purpose collider detectors being designed for the LHC: ATLAS [13] and The Compact Muon Solenoid (CMS) [14]. The measurements charac-

terizing hadronic punchthrough, which are presented below, are general results and may be applied to any experiment. However, when investigating the impact of muon backgrounds on LHC detectors, it is useful to make reference to a particular detector design. Throughout this dissertation, we use the CMS detector for this purpose.

CMS is a general purpose collider detector, but as the name suggests, it is optimized to measure muons. The design priorities of CMS have been set to achieve:

i) a very good and redundant muon system,

ii) the best possible electromagnetic calorimeter consistent with i),

iii) and a high quality central tracker to achieve i) and ii).

A schematic of the CMS detector is presented in Figure 1.3. The central part of the detector consists of a central tracker, electromagnetic calorimeter (EC) and hadronic calorimeter (HC), all inside of a solenoidal magnet. The solenoidal field has a maximum strength of 4 T. There are four muon measurement stations behind the hadronic calorimeter. The stations are labeled MS1-MS4 in the barrel and MF1-MF4 in the end-cap. The muon chambers are embedded in an iron return yoke (labeled RY1-RY3 in the barrel and RF1-RF3 in the end-cap). The magnetic field strength in the return yoke is 1.8 T. The very forward calorimeter (VF) is located behind the end-cap muon chambers.

1.4.1 Muon System

The muon system should fulfil several basic tasks: muon identification, trigger, momentum measurement and measurement of the muon's position in space. Furthermore, the number of tracks in the central tracker in front of the calorimeter is very

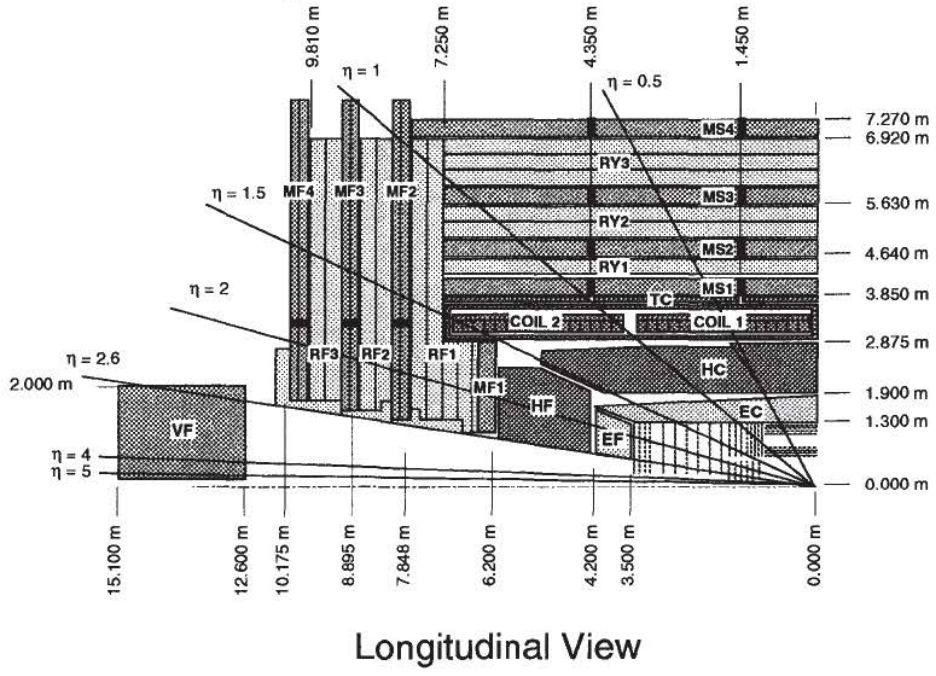

Figure 1.3: Schematic of the CMS detector. The barrel muon stations are labeled MS1-MS4. The forward muon stations and labeled MF1-MF4. The hadronic calorimeter (HC) and electromagnetic calorimeter (EC) are located inside a solenoidal magnet. The very forward calorimeter (VF) is located behind the end-cap muon chambers.

large and there are frequently jets near the muon. To obtain an unambiguous matching between the track in the central tracker and in the muon chamber, a good stand alone measurement of position, direction and momentum in the muon chambers is essential.

The muon system should be able to provide a precision momentum measurement over a wide range, from a few GeV/c to a few TeV/c. The high field solenoid magnet and the iron return yoke, which also serves as an absorber for muon identification, ensures the performance of this task. The muon momentum may be measured in three independent ways:

- sagitta measurement in the inner tracker,
- bending angle measurement after the coil and
- sagitta measurement in the return yoke.

The best momentum resolution is obtained when all three methods are combined.

There are four muon stations interleaved with the iron return yoke in both the barrel and the end-cap. Each station consists of multi-layer muon chambers. In the barrel region, where the particle flux is low ($\sim$ 1 Hz/cm^2) and there is no appreciable magnetic field in most areas, each station is composed of drift tubes [15]. This chamber consists of 12 layers of drift tubes arranged in three Super Layers of 4 planes each: the two outer Super Layers measure the coordinate in the bending plane and the middle Super Layer the coordinate along the beam line.

Muon measurement in the end-cap muon stations will be provided by Cathode Strip Chambers (CSC). This technology is able to provide precise spatial and timing information in the presence of high magnetic fields and high particle fluxes. CSCs are multiwire proportional chambers with the cathode plane segmented into strips.

There are 6 drift gaps per chamber. The end-cap chambers will be trapezoidal shaped with radial cathode strips. The precision coordinate in CSC chambers is derived from a determination of the center of gravity of the charge induced on the cathode strips when an avalanche is formed on an anode wire.

In MF2, MF3 and MF4, the anode wires will be oriented at right angles to the cathode strips. The chambers in MF1 are located in a region where the magnetic field has a strength of 3.8 T and is oriented perpendicular to the chamber. The anode wires of the chambers in MF1 will be tilted at an angle of 27° in order to compensate for the Lorentz drift of the ionization in the magnetic field.

In addition to the chambers in each station providing precise position measurements and first level trigger, there will also be Resistive Plane Chambers [16] solely dedicated for the first level muon trigger. These chambers will assign a bunch crossing to the track candidates and measure roughly their momenta.

The dead spaces between chambers in each station has been kept to a minimum. This insures that each muon always crosses at least three stations. The number of stations and the number of layers per station provide a high degree of redundancy. For example, even if the muon track measurement in one station is obliterated by the presence of a muon-induced electromagnetic shower, the other 3 stations will still be available to provide the muon measurement.

1.4.2 Tracking

The design goal of the central tracking system is to reconstruct isolated high p_T tracks with an efficiency of better than 95% and high p_T tracks within jets with an efficiency of better than 90% over the pseudorapidity range $|\eta| < 2.6$. The momentum resolution required for isolated charged leptons in the central rapidity region is $\Delta p_T/p_T \approx 0.1$.

This will allow the measurement of the lepton charge up to $p_T \approx 2$ TeV.

Pattern recognition at high luminosity will be challenging. At a luminosity of 10^{34} cm^{-2}s^{-1}, interesting events will be superimposed on a background of about 500 soft charged tracks from $\approx$ 20 minimum bias events occurring in the same bunch crossing. Solid state pixel and microstrip as well as gas microstrip detectors can provide the necessary granularity and precision. Strip lengths on the order of 10 cm are needed to maintain cell occupancy below 1%. This high granularity leads to a large number of channels ($\approx 10^7$).

The innermost layers of the central tracker will be composed of high resolution silicon pixel detectors. These detectors provide three dimensional space points suitable for the high track density close to the interaction vertex and guarantee high precision for secondary vertex detection and flavor tagging.

The pixel detector will be followed by several layers of silicon microstrip detectors. High spatial precision and time resolution combined with adequate radiation hardness make silicon detectors ideal for the intermediate tracking region. The outer tracking layers employ microstrip gas chambers (MSGC). The fast charge collection from the thin gas volume ensures good time resolution. Good spatial resolution in the less congested outer region is provided by detectors with a coarser pitch (200μm) than that of the silicon detectors (50μm).

1.4.3 Calorimetry

The physics channel which imposes the strictest performance requirement on the electromagnetic calorimeter (EC) is the low mass Higgs (90 GeV $< m_{\mathrm{H}} <$ 130 GeV) decaying into two photons. The energy resolution must be sufficient to detect this signal above other di-photon backgrounds. To achieve this CMS has chosen an EC

using lead tungstate ($PbWO_4$) crystals.

In order to determine from which of the primary vertices the photons originate, the photon direction must also be measured. This requires that the photon shower be measured at two depths in the EC. This will be carried out using a preshower detector consisting of a single plane of silicon strip detectors with a pitch of 2 mm, placed behind $\approx 3X_0$ of lead.

The di-photon background coming from π^0 decay may be reduced if one can resolve each photon. This can be done by choosing an appropriately fine transverse segmentation of the crystals. A transverse segmentation of $\Delta\eta \times \Delta\phi = 0.0145 \times 0.0145$ is sufficient for π^0 rejection in the barrel. In the end-cap, for a given π^0 p_T, the two photons fall closer to each other but have higher energies than in the barrel. The most efficient way to reject π^0's in the end-cap is to use a preshower detector consisting of two orthogonal planes of 2 mm silicon strip detectors placed after $\approx 3X_0$ of lead.

The hadronic calorimeter (HC) surrounds the EC and acts in conjunction with it to measure the energies and directions of particle jets, and to provide hermetic coverage for measuring missing transverse energy. The active elements of the barrel and end-cap HC consists of plastic scintillator tiles with wavelength-shifting fiber readout. Layers of these tiles alternate with layers of copper absorber to form the sampling calorimeter structure.

The HC must have good hermeticity, good transverse granularity, moderate energy resolution and sufficient depth for hadron shower containment. CMS has chosen a lateral granularity of $\Delta\eta \times \Delta\phi = 0.087 \times 0.087$ for $|\eta| < 2.0$. This granularity is sufficient for good di-jet separation and mass resolution. The calorimeter readout must have a dynamic range from 20 MeV to 2 TeV to allow the observation of single muons in a calorimeter tower while maintaining adequate response for the highest

energy hadronic showers.

There are two main physics motivations for a very forward calorimeter (VF) which covers the pseudorapidity range $3.0 \leq |\eta| \leq 5.0$. The first is to improve the measurement of missing transverse energy. The second is to identify very forward jets, which characterize several important physics processes. For example, if the SM Higgs does not exist, or if it is extremely massive, the study of longitudinal IVB scattering will be important and require the detection of very forward jets.

The very forward region will have a very high rate and high radiation dose; consequently, the VF must have a very fast response time and be radiation hard. To achieve this, the CMS baseline design calls for a modular iron/gas sampling calorimeter based on Parallel Plate Chambers (PPC). The VF/PPC if inherently radiation hard, since an exchangeable active medium - a nonflammable, hydrogen less, circulating gas - is used.

Chapter 2

The Muon Signal at the LHC

2.1 Prompt Muons

The so-called *prompt muons* originate from physics processes close to the collision vertex. The sources of prompt muons are decays of heavy quarks (charm, bottom and top), W and Z decays and Drell-Yan processes. The rate, at all transverse momenta, is dominated by charm and bottom decays. The inclusive rate of prompt muons at the LHC has been calculated by Monte Carlo programs (for example see Reference [17] and Section 4.1 below). Estimates of the muon rate (at $\mathcal{L} = 10^{34}\text{cm}^{-2}\text{s}^{-1}$) in the barrel region of a typical LHC detector range from about 5×10^4 Hz to greater than 10^5 Hz. It is the job of the first-level muon trigger system to reduce this rate to a level which is compatible with the bandwidth of the data acquisition system. In the CMS detector, the full available bandwidth of 100 kHz should be shared among various triggers. Thus the maximal rate allowed for the signal muon trigger is of the order 3 kHz.

The measurement of muons consists of several parts: identification, trigger and measurement of their momentum and position in space. In general, muons are iden-

tified as minimum ionizing particles penetrating deeply through matter. In collider detectors, muon measurement stations are installed behind calorimeters, which in addition to measuring energy, absorb photons, electrons and hadrons.

2.2 Muon Backgrounds

Background muons can be divided into two catagories: 1) real muons and 2) processes which can fake muon tracks or which obscure the accurate measurement of muon trajectories. Sources of real background muons include muons coming from π and K decays in a tracking volume in front of a calorimeter (*decay muons*) and muons from hadronic punchthrough. Processes which can fake real muons or obscure muon measurement include uncorrelated neutrons and gammas and electromagnetic secondaries induced by the high energy muons themselves. Each of these processes will be discussed in more detail below. A detailed study of the effect of neutrons and gammas and muon-induced electromagnetic secondaries is not the main goal of this dissertation, however, these backgrounds have an impact on the design of LHC detectors, so a discussion of these topics is included. Cosmic rays and so-called "non-interacting" hadrons can also fake the prompt muon signal, but they are not expected to contribute significantly to the trigger rate and will not be considered further here.

2.2.1 Decay Muons

The source of decay muons are hadrons which emerge from the collision vertex and decay in flight before they reach the calorimeter. The majority of charged hadrons produced in p-p collisions are π and K mesons ($\sim$ 80%) while the remainder is composed of protons, neutrons and other heavy baryons. (For more details see Section 4.1.) The

rate of decay muons follows directly from the charged hadron rate. The probability for a hadron to decay before reaching the calorimeter is proportional to the path length between the interaction vertex and the calorimeter; this is determined by the size of the tracking volume. In the CMS detector, the distance from the interaction vertex to the calorimeter increases from 1.3 m at $\eta = 0$ to a maximum of 3.7 m at $\eta = 2.0$.

In Chapter 4, we estimate by Monte Carlo simulation the charged particle rate in the CMS muon system due to decay muons. In addition, we give the momentum distribution of decay muons as measured in the first muon station of CMS and the combined trigger rate due to decay muons and punchthrough muons.

2.2.2 Hadronic Punchthrough

The vast majority of charged hadrons produced at the LHC will not decay in the central tracking volume but will interact in the calorimeter. Hadrons loose energy while passing through matter by electromagnetic processes until they undergo a "hard" nuclear interaction. The mean free path for nuclear interactions (also called the nuclear interaction length, λ) of a pion in iron is about 16.8 cm. The probability of interaction is constant throughout the material, so it follows that the probability of passing through a given length of material without interaction is exponentially falling with increasing thickness. The first hard interaction initiates a hadronic cascade composed mainly of charged and neutral mesons ($\pi^{\pm}$, π^0, $K^{\pm}$, K^0, $\overline{K}^0$). The total energy of the hadronic cascade is then quickly absorbed. For the highest momentum hadrons foreseen at the LHC, 95% of the energy will be absorbed in about 10λ of iron.

So-called *hadronic punchthrough* consists of all hadronic shower debris which exit an absorber. This includes secondary muons which come from the decay of pions

and kaons in the hadronic shower cascade. With increasing thickness of absorber the relative contribution of secondary muons, which are less easily absorbed, increases and dominates for absorber thickness greater than about 10λ. Therefore, in this text when we speak of *punchthrough particles*, we mean punchthrough muons and all other particles exiting an absorber. Likewise, when we refer to *punchthrough muons*, we refer only to the muon component.

From the previous discussion, we see that hadronic punchthrough does not represent a significant leakage of hadronic energy, but rather that hadronic shower debris which *punch through* the calorimeter, and enter the muon system, will contribute to the overall charged particle rate in the muon chambers and that punchthrough muons will contribute to the muon trigger rate. This background was present in previous experiments at hadron colliders. For example, the UA1 collaboration installed sizeable shielding, beyond the normal calorimeter shielding, in front of the muon chambers to keep the number of punchthrough events at a tolerable level. Because of the unprecedented high design luminosity and center of mass energy planned for the LHC, the punchthrough contribution to muon trigger rates and the charged particle flux reaching the muon chambers must be carefully estimated.

The main goal of the RD5 experiment at CERN [18] is to measure the total punchthrough probability of hadronic showers and the momentum and angular spectrum of punchthrough muons, over a wide range of incident hadron momenta and for several different kinds of incident particle, in order to verify the predictions made by Monte Carlo programs and provide data for parameterization. The RD5 detector simulates a portion of a typical collider detector; therefore, we are able to study punchthrough phenomena in an experimental environment similar to that which will be encountered in experiments at the LHC, including the presence of a strong magnet field.

In Chapter 3 below we present a detailed description of the punchthrough measurements and simulations conducted in RD5. In Chapter 4 we estimate by Monte Carlo simulation the charged particle rate in the CMS muon chambers due to punchthrough particles and give the momentum distribution of punchthrough muons as measured in the first muon station of CMS. In addition, the trigger rate of a trigger system which employes an angular cut to distinguish background muons from the prompt muon signal is given. Wherever possible the Monte Carlo results are compared with the experimental results of RD5.

Previous measurements and simulation of hadronic punchthrough phenomena can be found in the literature. A. Bodek [19] has made an extensive review of existing data (as of 1985) and given scaling laws for different absorber materials so that data from one experimental setup can be more easily applied to another. A parameterization of the total punchthrough probability was made by F. Lacava [20]. Such parameterization can be the basis of fast simulation programs. A detailed simulation of hadronic punchthrough based on the GHEISHA shower simulation program was made by H. Fesefeldt et al. [21]. The momentum spectrum of punchthrough muons was measured by D. Green et al. [22].

2.2.3 Neutrons and Gammas

At the LHC, the radiation level inside and surrounding the collider detectors will be very large. The increase in muon chamber occupancy due to the hits produced by a large number of neutral particles can affect chamber efficiency, pattern recognition algorithms and muon trigger rates.

The dominant source will be hadrons produced via p-p collisions at the interaction vertex which interact in the calorimeters, the beam pipe and in a collimator which will

shield the first superconducting quadrupole just upstream of CMS. The neutrons are produced as a component of the hadronic shower. Unlike charged particles, neutrons can travel long distances and loose energy through numerous elastic collisions. As a result of this lengthy scattering process, these neutrons form a "gas" of slow particles widely distributed inside and around the detector and are uncorrelated with the bunch crossing time of the primary hadron.

Neutrons can produce hits in gaseous detectors by scattering off light nuclei. The maximum recoil energy increases for lighter nuclei and is largest for hydrogen. Usually the recoil protons cannot escape solid material, so the n-p scattering contribution can be reduced by avoiding hydrogenated gases in detectors. Neutrons can also produce hits in detectors through neutron capture, followed by gamma de-excitation. The gammas interact in the sensitive volumes of the detector through photoelectron production, Compton scattering and e^+e^- pair production.

Hadrons emerging from the collision vertex at $\eta \leq 2.5$ will interact in the barrel or end-cap calorimeters. The neutrons produced in the calorimeters are expected to leak back into the central tracking volume. In the literature this is referred to as *neutron albedo*. The high radiation level due to primary charged hadrons coming from the interaction vertex, coupled with the neutron albedo, will affect the long term performance of the silicon tracking detectors. The effect of hadron fluxes on the central tracker of CMS has been studied [23].

The hit rate due to neutrons and gammas in the three innermost muon stations of CMS is expected to be small, compared to the charged particle rate, because the chambers are embedded in the iron return yoke which acts as an efficient shield against fast neutrons. The real problem is expected in MS4 and MF4, which are exposed to neutrons from outside of the detector. Hadrons produced at $\eta > 2.5$,

and those trapped by the central magnetic field, will interact in the very forward calorimeter (see Figure 1.3) and in a copper collimator just up stream of the very forward calorimeter. Neutrons produced in the very forward calorimeter, collimator and beam pipe will enter the experimental hall and ultimately produce hits in the outer muon chambers.

The radiation environment in and around CMS has been studied by several groups [24, 25, 26] and they have proposed a shielding configuration which can reduce the neutron background in the most affected regions of the detector by 2 to 3 orders of magnitude. The shielding will surround primarily the very forward calorimeter and copper collimator. The shielding is composed of materials with a high hydrogen content, such as concrete or polyethylene, which slow the neutrons to thermal energies. The external surface of this shield can then be covered with a boron doped material in order to efficiently capture thermalized neutrons without copious gamma production. An additional high Z material, such as lead, should also be present to absorb gammas which happen to escape the other shielding. Neutron production in the beam pipe can be reduced by constructing the beam pipe of beryllium and keeping its thickness to a minimum.

The effect of random hits from neutrons and gammas on the CMS muon trigger has also been studied [27, 28]. It is expected that some combination of random hits could by chance satisfy the trigger criteria and increase the overall trigger rate. Also, random hits in coincidence with a real muon track could lead to a mis-measurement of the real muon momentum. For the trigger algorithm studied, this causes low p_T, highly curved muon tracks, to look more like straight tracks and thus increase their apparent momentum.

It was found that, for the shielding configuration studied, the trigger rate due

to neutral particles producing random hits in the muon system, and random hits associated with real muons, was well below the trigger rate due to prompt muons, down to the lowest trigger thresholds. This study also took into account the intrinsic noise of the RPCs, which were used as the trigger detector, and the electronic noise of the front-end readout. It should be pointed out, however, that the trigger rate due to neutrals rises as the third power of the background hit rate, therefore, if the particle fluxes are underestimated by a factor 5, the false trigger rate could exceed the real one. This fact underlines the importance of accurately understanding the neutral background.

2.2.4 Muon-induced Electromagnetic Secondaries

While passing through matter muons loose energy through the processes of ionization, bremsstrahlung, direct e^+e^- pair production and photonuclear interactions. The cross-section for the photonuclear interaction is one order of magnitude smaller than the cross-sections for bremsstrahlung and pair production and will be less important for the muon energy range expected at the LHC. At energies below a few tens of GeV, muon energy loss is dominated by the process of ionization which is described by the Landau theory. Some of the electrons liberated by the process of ionization may themselves have sufficient energy to create further ionization or electromagnetic (e.m.) showers. These electrons are referred to as *knock-on electrons* or *δ-electrons*. As the muon energy increases, radiative losses begin to dominate over ionization. At the muon energy of about 330 GeV the total energy loss is twice the ionization loss [29].

Some fraction of high energy muons will loose a significant part of their energy by radiating hard photons and electron pairs which will initiate e.m. showers. The

consequence of these so-called "catastrophic" energy losses can be two fold. First, if the energy loss occurs in the calorimeters or, in the case of the CMS detector, in the iron of the return yoke, this will result in a incorrect measurement of the muon energy. If the shower does occur in one of the calorimeters it may be possible to correct for this energy deposition later and save the muon measurement. This would not be possible for an e.m. shower occurring in the return yoke. Secondly, the muon-induced e.m. shower could overlap the active layers of the muon detectors and thus obscure the measurement of the muon track. This will compromise the muon momentum measurement. Furthermore, in order to obtain an unambiguous matching between the track in the central tracker and in the muon chamber, a good stand alone measurement of position, direction and momentum in the muon chambers is essential.

The experiments at the LHC must be able to measure muons with energies up to several hundred GeV, so it is important that the effects of muon-induced e.m. secondaries are studied and, where possible, methods are found which will diminish their damaging effect. One such study has been made by the RD5 collaboration. In this study [30], the production of e.m. secondaries by muons, with momenta from 10 to 300 GeV/c, was measured using several detectors foreseen for the LHC. The studies were made with different geometries, i.e. detectors at various distances from the absorber, and different detector types, such as, a silicon beam telescope (SiBT) [31, 32], and gaseous detectors such as, Honeycomb Strip Chamber (HSC) [33], Wall-Less Drift Chamber (WLDC) [34], Drift Tubes with Bunch Crossing Identification (DTBX) [15] Cathode Strip Chambers (CSC) [35] and Resistive Plate Chambers (RPC) [16] foreseen as a muon trigger detector.

While the detailed conclusions of this study depend on the particular detector technology in question, one can draw some general conclusions concerning ways to re-

duce the damaging effect of muon-induced e.m. secondaries. First of all, results from each technology were compared with a GEANT-based detector simulation. In each case the simulation and measured data agreed well in both the number of secondaries produced and in their spatial distribution with respect to the location of the primary muon track. The success of the simulation gives us confidence that the simulation can be used to make predictions concerning new detector configurations.

It was found that placing the muon detector some distance from the iron absorber, would allow the e.m. secondaries to be well separated from the muon track. For a 2-track resolution of 2 mm and the detector placed at a distance $d \geq 15$ cm from the iron, it was found that the number of spoiled track segments was significantly reduced. On the other hand, if one has space constraints and cannot move the detector so far away from the iron, making the detector body of massive aluminium reduces the number of disturbing hits by absorbing soft secondaries or scattering them considerably. This was studied with a WLDC-like geometry with chamber walls about 1 cm thick.

A further general result is that, of the 5 detector technologies studied, all were able to recognize the presence of e.m. secondaries in one multi-layer chamber forming a muon measurement "station". They all succeed in identifying the track segment and even the individual cell affected by such a secondary, even far beyond the 2-track resolution limit. Affected track segments can thus be reliably removed from the muon reconstruction. In many cases only 1-2 layers of a station are affected. Instead of discarding the whole track segment in the station, one can remove the affected hits only. Simulation demonstrated that by removing the spoiled hits and re-fitting the track, about 75% of the reconstructed tracks which originally failed the precision criteria could be rescued.

Chapter 3

Measurement and Simulation of Hadronic Shower Punchthrough in Experiment RD5

The RD5 collaboration at CERN [18] was formed to study topics related to muon detection at future hadron colliders. These topics included: measurement of the total punchthrough probability of hadronic showers, measurement of angular and momentum distributions of punchthrough muons and to demonstrate the advantage of a strong magnetic field in efficiently suppressing punchthrough particles. In addition, RD5 has conducted muon trigger studies, investigated the influence of electromagnetic secondaries on muon measurement and tested various types of large area muon detectors. An overview of the RD5 experimental program can be found in two status reports [36, 37].

In Section 3.1 the RD5 detector is described. Next, in Section 3.2, and the experimental method used to measure total punchthrough is described, followed by a description of the Monte Carlo simulation program. In Section 3.2.3, we present the

results of measurements of the total punchthrough probability of hadronic showers as a function of depth in an absorber in a magnetic field ranging from 0 to 3 T. The lateral distribution of shower particles and the shower particle multiplicity measured at two absorber depths is also presented. The influence of the magnetic field on these measured quantities is shown and the measurements are compared with the results of the Monte Carlo simulation.

In addition to the measurement of total punchthrough, another important part of the RD5 experimental program is the measurement of the momentum and angular spectrum of punchthrough muons. In Section 3.3 the results of these measurements are presented along with a description of the data analysis method.

This chapter in concluded, in Section 3.4, with a summary and discussion of the results.

3.1 The RD5 Detector

A schematic view of the RD5 detector, located in the CERN North Area H2 beam, is shown in Figure 3.1. The detector was designed to simulate a CMS-like detector [14], having a silicon tracker, a calorimeter and muon measurement stations. Each muon station consists of drift chambers and Resistive Plate Chambers (RPCs). The set-up includes two magnets, a superconducting magnet (M1), with a maximum 3 T field, and a toroidal magnet (M2) operated at 1.5 T. The magnet M1, which contains a tracking calorimeter (TRACAL), simulates the strong solenoidal field of CMS, while magnet M2 simulates the CMS return yoke.

A stainless steel/gas tracking calorimeter (TRACAL) is installed inside M1. TRACAL [38] consists of stainless steel plates interleaved with Honeycomb Strip Chambers (HSC)[33], which can measure tracks accurately. Each chamber has an active area of

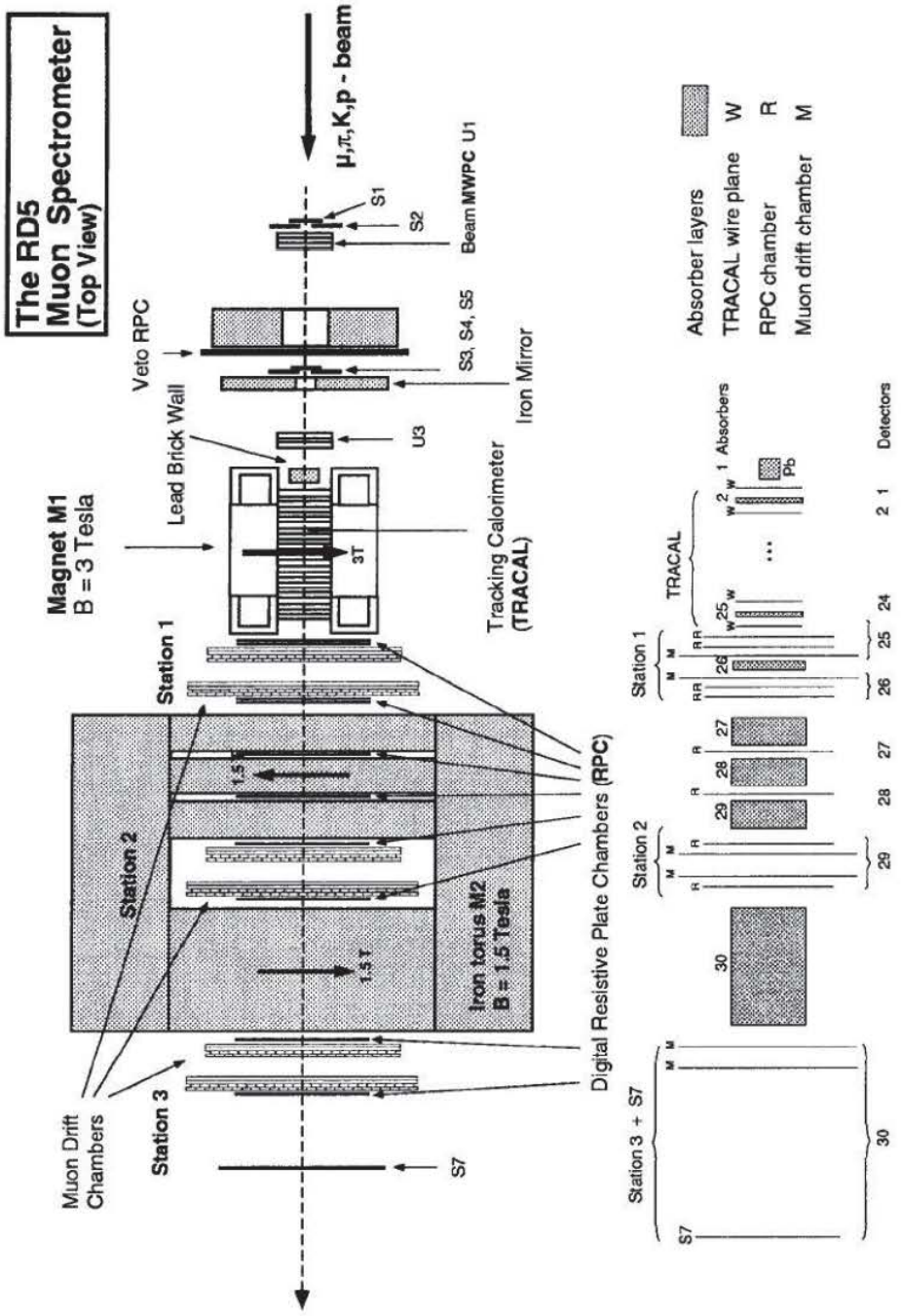

Figure 3.1: Schematic view of the RD5 detector in its 1993 configuration.

$0.6 \times 0.8\,\mathrm{m}^2$, with 26 mm gaps between the absorbers. The HSCs are made of mylar foil with copper readout strips. The foil is folded so that the folds are perpendicular to the strips. Two folded foils are put together with double-sided adhesive tape resulting in hexagonal cells. In the center of each hexagonal cell a wire is strung. The main purpose of TRACAL is to identify muon contamination in the hadron beam.

In order to facilitate its installation inside M1, TRACAL was separated into two units. Between the first 13 HSC chambers, the absorbers (stainless steel plates $0.8 \times 1.0\,\mathrm{m}^2$) were 40 mm thick, thus totaling 12 times 0.25λ. Where λ is one interaction length. The next 12 gaps between the HSC chambers were filled with plates each 80 mm thick giving another 12 times 0.5λ. The total absorption power of TRACAL is thus about 9λ. In front of TRACAL a lead brick wall of about one interaction length (29 X_0) was installed to simulate the absorption of an electromagnetic calorimeter.

The magnet M1 [39] is composed of two parallel superconducting coils without a yoke. In the RD5 coordinate system, the axis of the two coils is oriented along the z-direction, transverse to the beam direction. The beam is along the x-direction. In the region between the two coils, the magnetic field is oriented predominately in the z-direction. At the maximum field of 3 T, the radial component is less than 0.67 % in the region near the beam line. In Figure 3.2, the magnitude of the magnetic field, $|B_z|$, is plotted as a function of x and z. TRACAL sits at the origin of the coordinate system and extends to ± 1.1 m in the x-direction and ± 0.4 m in the z-direction. One sees that the field strength varies significantly over the length of TRACAL, along the beam-line, falling to about 50% of its maximum value at ± 1.1 m. The bending power of M1 can be expressed as $\int \vec{B} \times d\vec{l}$, evaluated over the length TRACAL and along the beam axis (-110 cm $\leq x \leq +110$ cm, $y = 0, z = 0$). The result of this integral, calculated numerically using a magnetic field map of M1, is 5.2 T·m. In contrast, a

uniform 3 T field over the length of TRACAL would have a bending power of 6.6 T·m.

The absorber magnet (M2) [40] is a 1.5 T iron magnet constructed as a closed magnetic circuit, 1.8 to 2 m thick, made up of 0.2 m thick steel plates. Two 88 mm slots are provided in the upstream section to insert Resistive Plate Chambers (RPCs) [16]. The $0.9 \times 4.8\,\mathrm{m}^2$ inner area enclosed by the iron circuit has been dimensioned to accept a muon measurement station.

In order to measure the trajectories of the muons in the RD5 spectrometer with high accuracy six muon drift chambers from the UA1 experiment [41] were installed, two in every muon station. In each station the two chambers are mounted 0.6 m apart to provide a good determination of the muon direction. Each muon station covers an area of $3.2 \times 3.8\,\mathrm{m}^2$. Each chamber is made of crossed layers of long drift tubes, each 150 mm wide and 45 mm thick. The detection efficiency of each tube is about 99 % over the whole drift volume. It was found that the spatial and angular errors of the track segments in each chamber are about 1 mm and 1 mr in each projection, while the intrinsic track resolution of a single chamber is about 250 μm.

RPCs are mounted on either side of the muon drift chambers to form a muon measurement station. They are also mounted in the iron slots in the first half of magnet M2. These chambers are used for muon trigger studies and, together with the drift chambers, for muon track reconstruction. Each plane measures $2 \times 2\,\mathrm{m}^2$ and has 64 readout strips of 30 mm pitch. The planes are coupled in pairs providing one measurement in the horizontal projection, z, and one in the vertical projection, y. Furthermore, for the study of hadronic punchthrough, there needs to be an efficient veto against hits produced by off-time and halo muons. A veto wall, that covers the entire area of the muon drift chambers, was built with an array of RPCs and placed 1.2 m upstream of the magnet M1.

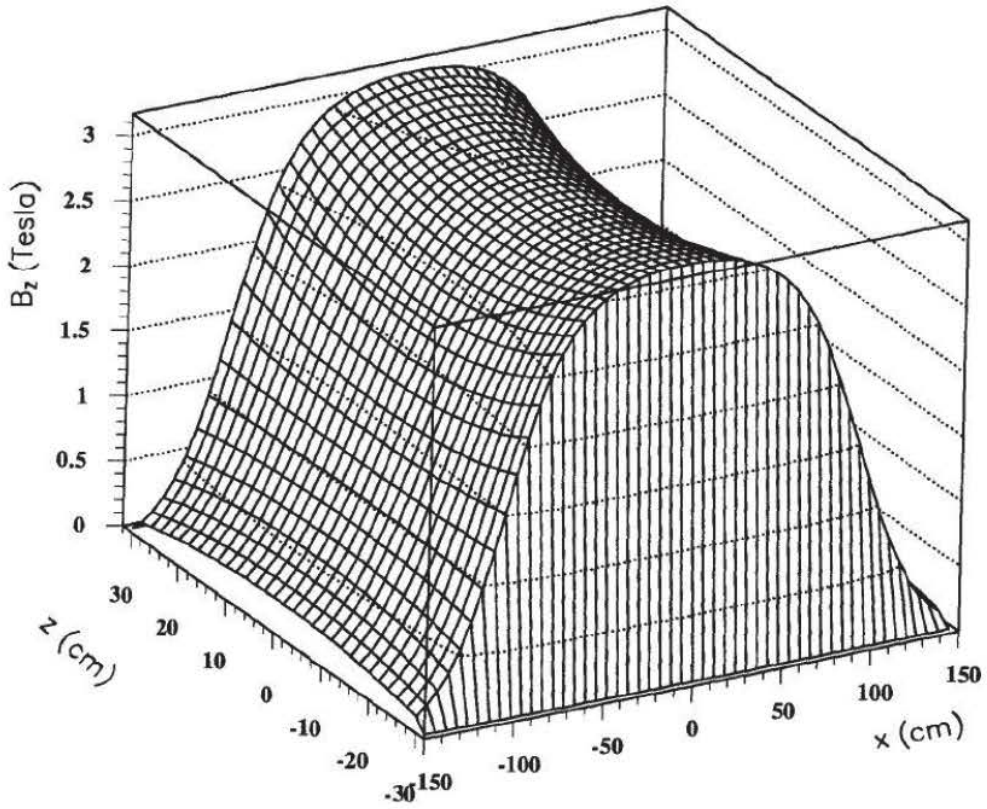

Figure 3.2: The z-component of the magnetic field in M1, plotted as a function of x and z. The x-direction is parallel the beam, while the z-direction is transverse to the beam.

The RD5 trigger system (see Figure 3.1) consists of scintillators S1 and S5 for the beam definition and S4a-b for beam size determination. The system of counters S2 and S3, together with the RPC veto wall described above, form a veto system against beam halo particles. It is ensured that there are no other particles crossing the 4×4 m^2 area of the RPC wall within $\pm 2\mu s$ around the triggering one.

Two trigger modes were used for the measurement of total punchthrough: a minimum bias trigger (MB) and a ten lambda (10λ) trigger. The minimum bias trigger consisted of scintillators S1 and S5 in anti-coincidence with the veto system, thus flagging a single particle entering the detector. The 10λ trigger consisted of the minimum bias trigger with the additional requirement that there was at least one hit in the RPC counters in the muon station 1, at an absorber depth of 10λ.

The multiwire proportional chambers (MWPCs) [42], referred to as U1 and U3, were used to define the incident beam. The chambers have 5 active planes with 128 gold plated wires in each plane. The wire diameter is $20\,\mu$m and the wire pitch is 2 mm. Each wire plane has its own orientation with respect to the horizontal (+30°,+30°,90°,-30°,-30°). The cathode planes, which alternate with the sensitive planes in 8 mm gaps, are made of $100\,\mu$m diameter wires spaced by 1 mm. The chambers U1 and U3 are positioned at 1 m and 17.5 m, respectively, upstream of TRACAL and rotated by 90° with respect to each other.

A Cerenkhov counter CEDAR, being a standard H2 beam equipment, was used for running with positive pions, kaons and protons in order to distinguish various kinds of particles.

3.2 Measurement of Total Punchthrough

3.2.1 Data Sample and Analysis Method

During the 1991 run period, data were taken with negative muon and pion beams. The beam momenta were 30, 40, 50, 75, 100, 200 and 300 GeV/c. The muon data were used to characterize the muon contamination in the pion beam and for detector calibration. The results of the analysis of 1991 data have been previously published [43].

In 1992 and 1993, the RD5 data set was expanded and also included negative pions of momentum 10 and 20 GeV/c as well as positive hadrons (π^+, K^+ and protons) of momentum 30 to 300 GeV/c. Data were also taken with the M1 magnet at full field (3 Tesla) and at half field. For each beam momentum and magnetic field setting, data with a muon beam was also taken and was used for background subtraction and detector calibration. A detailed account of the analysis of the 1992/1993 RD5 data set is presented below.

The π^- beam used by RD5 contained from 2 to 10% of primary muons, depending on the beam momentum. This muon contamination comes from pion decays in flight upstream of the detector. The positive beam consisted of a mixture of different particles, which had to be selected by the CEDAR trigger. However, muons and pions could not be separated and so the π^+ beam contained a similar contamination as the π^- beam. The CEDAR counter, located some 100 m upstream, could also not completely reject the muons from kaon decays. Thus, the only pure beam was the proton beam. The high muon contamination in the hadron beams requires one to use careful background subtraction procedures.

A pion punchthrough event and a muon event in the RD5 detector are shown in Figures 3.3 and 3.4, respectively. In Figure 3.3, one sees a large shower in the

calorimeter, originated by the 50 GeV/c pion, and a penetrating track reaching muon Station 2. In the x-y projection, the penetrating track is seen bending in the 1.5 T field of magnet M2. The x-z projection is in the non-bending plane. In Figure 3.4, one sees the relatively straight minimum ionizing track of a 50 GeV/c muon penetrating the entire RD5 setup. The dotted line on each figure shows the result of the muon track reconstruction (for details see Section 3.3.1).

We define the *total punchthrough probability* at a given depth x as the ratio of the number of events with at least one hit in the detector at the depth x over the total number of events. This definition should be distinguished from the *integral punchthrough probability*, which is defined as the number of hits measured at a depth x divided by the total number of events. The integral punchthrough probability is equal to the total punchthrough probability times the average number of hits per event.

The data analysis method consists of the following steps:

- Check the number of tracks in MWPCs. For each trigger, all events with more than one track in MWPCs, U1 and U2, are excluded from the analysis. This requirement excludes particles which begin to shower before the calorimeter.
- Measurement of the penetration depth of each event (see text below).
- Subtraction of the muon contamination present in the pion beam (see text below).

During data taking, the 10λ trigger was used in order to increase measurement statistics at absorber depths greater than 10λ. For example, the number of signal events reaching Station 3 (31λ) was increased by a factor 2 to 7 (depending on the total event statistics collected) over the statistics with the MB trigger alone. The

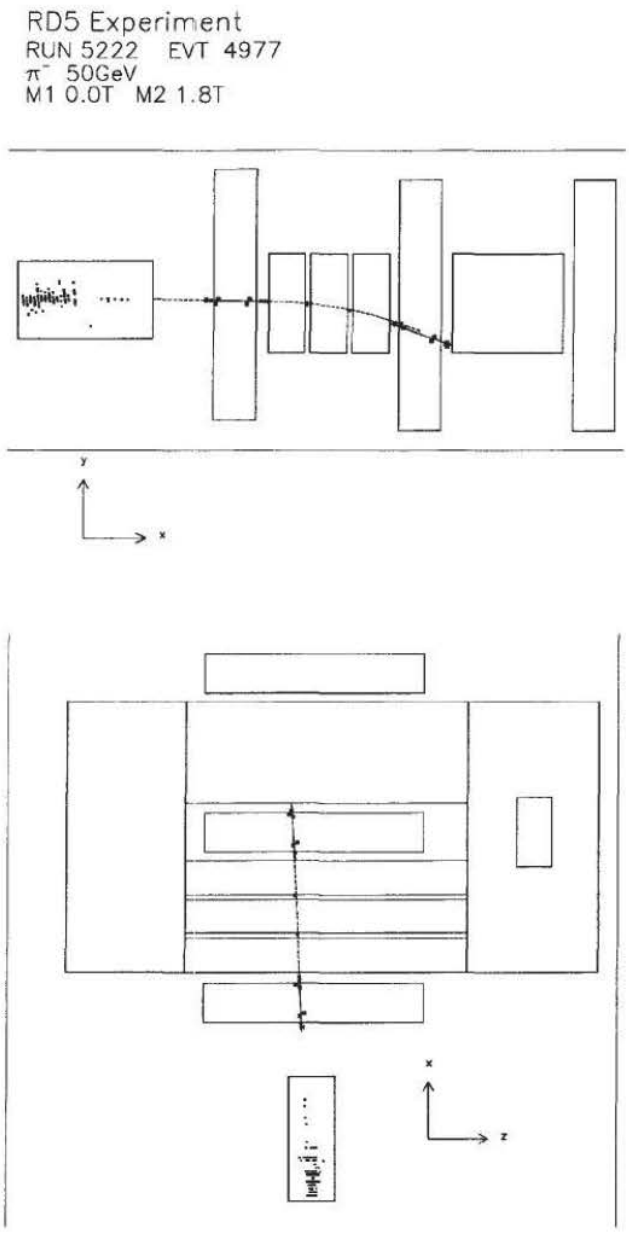

Figure 3.3: Pion punchthrough event in RD5.

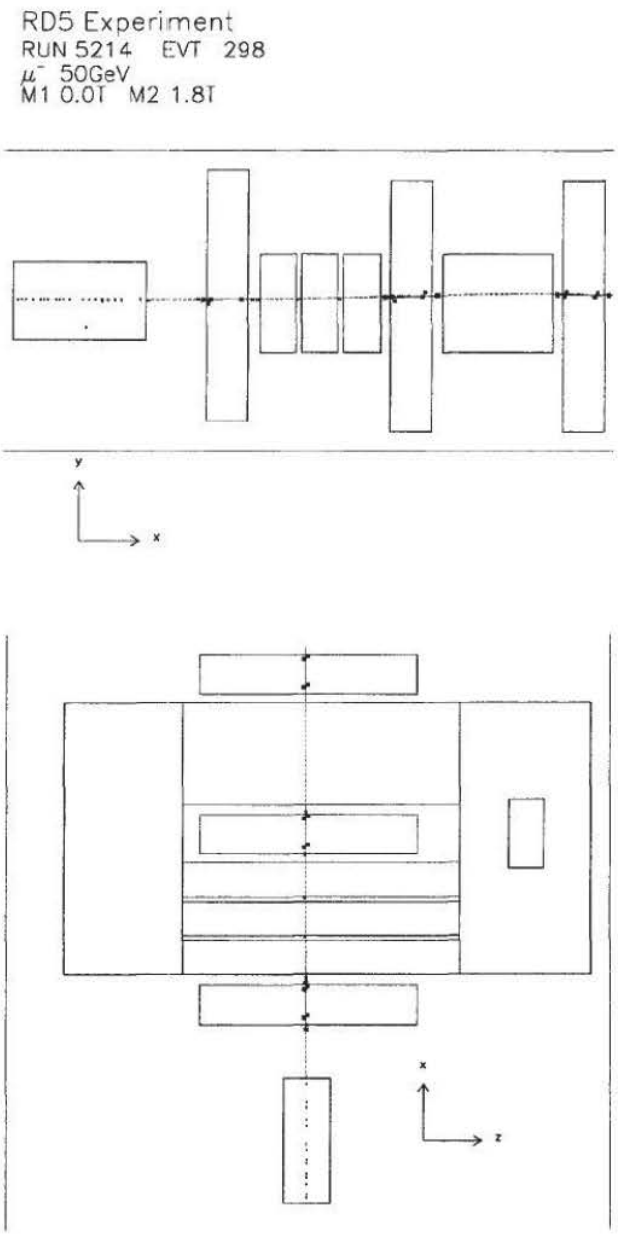

Figure 3.4: Muon event in RD5.

correct trigger normalization for the data taken with the 10λ trigger, was found by counting the number of 10λ triggers which occur as a subset of the minimum bias triggers. After the results obtained with the 10λ trigger condition had been properly normalized, the two sets of results (MB and 10λ) were combined by a weighted average. The event statistics used in the present measurement of total punchthrough are presented in Tables 3.1 and 3.2, for the MB and 10λ trigger condition, respectively.

Table 3.1: Event statistics with minimum bias trigger (MB) used in the analysis to measure total punchthrough.

momentum	particle type			
[GeV/c]	π^-	π^+	K^+	proton
	Event statistics, M1 field 0 T			
10	69000			
20	61000			
30	101000	86000		
50	77000			
100	103000	70000	39000	68000
200	35000			
300	36000	61000		30000
	Event statistics, M1 field 1.5 T			
30	83000			
100	77000	65000		
300	37000			
	Event statistics, M1 field 3 T			
10	59000			
20	83000			
30	85000	85000		
50	79000		90000	
100	53000	37000	52000	46000
200	50000			
300	40000	45000		43000

Table 3.2: Event statistics collected with ten lambda trigger (10λ) used in the analysis to measure total punchthrough.

momentum [GeV/c]	particle type			
	π^-	π^+	K^+	proton
	Event statistics, M1 field 0 T			
10				
20	28000			
30	50000	53000		
50	44000			
100	52000	31000	11000	45000
200	14000			
300	13000	30000		20000
	Event statistics, M1 field 1.5 T			
30	42000			
100	27000	12000		
300	20000			
	Event statistics, M1 field 3 T			
10				
20				
30		43000		
50	32000		40000	
100	26000	20000	25000	31000
200	23000			
300	28000	16000		14000

Penetration Depth

There are 31 absorber depths d in the RD5 setup, each separated by single or grouped detector elements. The sequence of absorber layers and detector elements is presented schematically at the bottom of Figure 3.1. It should be noted that the absorber material at depth 26 is the sum of the chamber walls and chamber support structures in Station 1.

Let us denote the existence of a hit in a particular detector i by h_i, where $h_i = 0$ means no hits in the i-th detector and $h_i = 1$ means at least one hit in the i-th detector. A hit in detector i is weighted appropriately, given the efficiency f_i and noise level g_i of that detector. The detector efficiencies are measured using muons from the dedicated muon runs. The detector noise levels are measured by triggering at random within the pion beam.

For each possible penetration depth d and event j, the probability P_d^j to obtain a given hit pattern is calculated:

$$P_d^j = \prod_i [\theta(d-i)h_i f_i + \theta(d-i)(1-h_i)(1-f_i) + \theta(i-d)h_i g_i + \theta(i-d)(1-h_i)(1-g_i)]$$

where d is the absorber depth, 1 to 31, and i ranges over all detector elements (see bottom of Figure 3.1). $\theta(y)$ is a step function defined in the following way:

$$\theta(y) = 1 \text{ for } y \geq 0$$

$$\theta(y) = 0 \text{ for } y < 0$$

This analysis allows the different types of chambers present in RD5 to be treated in a consistent way. For any given event, the depth d having the highest probability P_d^j is called the range R of the event. This variable is used in the analysis to separate

pions from the muon contamination, but not to calculate the final punchthrough probability, as it will be explained below.

For the distribution of penetration depth the average probability $\overline{P_d}$ is calculated, where

$$\overline{P_d} = \frac{1}{N} \sum_{j=1}^{N} \frac{P_d^j}{\sum_{k=1}^{31} P_k^j}$$

and N is the total number of events. The distribution of this variable reduces the weight of ambiguous events (i.e. an event with two or more depths having similar probabilities). For example, it is possible to have the following hit pattern: 1 1 1 1 1 1 1 0 1 0 0 0 0 0 0. This pattern represents 7 hit chambers, a chamber with no hit, and then another hit chamber. The ambiguity arises if one must choose chamber number 7 or number 9 as the final hit chamber. One does not know if the hit in chamber 9 is definitely due to noise or if no hit in chamber 8 is due to an inefficiency. The penetration depth distribution weights properly all these cases thus enabling one to avoid arbitrarily choosing one penetration depth over another. Figure 3.5 shows the unnormalized penetration depth distributions for 100 GeV/c muons and pions. In Figure 3.5 b) one sees a broad bump corresponding to pion induced hadronic showers stopping in TRACAL or inside the absorber magnet, and a peak, at penetration depth 31, containing events penetrating through the whole detector; this peak contains primary muons events, but also contains punchthrough particles from pion showers. The sharp peak at measurement point 27 occurs because the thickness of absorber materials are not uniform throughout the detector. This peak corresponds to those particles which leak out of TRACAL, thus producing a hit at point 26, but then stop in the thick iron plate at the beginning of the absorber magnet M2.

After the removal of background events due to primary muons and halo muons, the pion penetration depth distribution (Figure 3.5 b) is integrated to obtain the final

punchthrough probabilities.

Subtraction of Muon Contamination

Muon events in RD5 are characterized by one clean minimum-ionizing track (see Figure 3.4) penetrating the entire detector. However, there are frequently additional hits in TRACAL due to δ - ray production and other electromagnetic processes induced by the muon. This is reflected in having at least one TRACAL layer with a large hit multiplicity. In addition, there could also be random hits due to noise. In contrast, pion showers (see Figure 3.3) typically have a high hit multiplicity in many TRACAL layers and a larger spread.

In order to separate the pion events from the muon contamination, an algorithm was developed which examines the array of hit TRACAL wires, and for each event, removes from the array the hits which correspond to the characteristics of a typical muon event. After this procedure, an excess of remaining hits should be characteristic of a pion shower.

The array of hit TRACAL wires, h_{ij}, is defined as follows:

$h_{ij} = 0$ means no hits in the j-th wire of TRACAL layer i

$h_{ij} = 1$ means at least one hit in the j-th wire of TRACAL layer i

The algorithm which removes hits from the TRACAL hit array consists of the following steps:

i) To account for the hits due to high-energy-loss electromagnetic processes, all hits are removed from the TRACAL layer having the highest multiplicity.

ii) Accidental hits (e.g. hits due to noise) are removed from the hit array by rejecting hits in the TRACAL layer i having the largest spread, defined by rms(i),

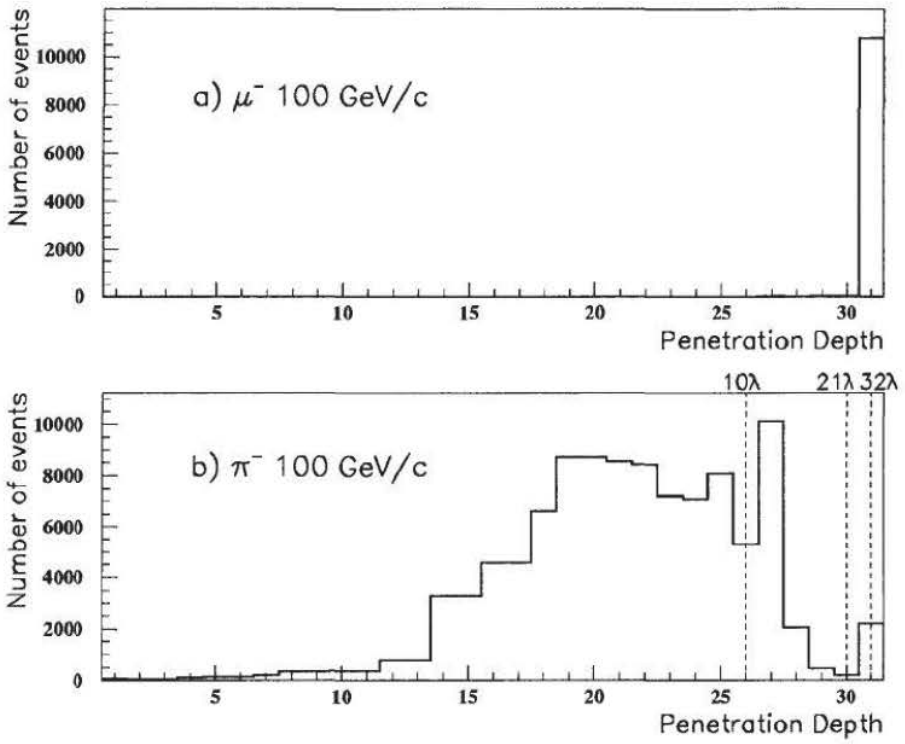

Figure 3.5: Penetration depth distribution of a) 100 GeV/c muons and b) 100 GeV/c pions. The depth scale used is the sequence of absorber materials in RD5 which is presented schematically at the bottom of Figure 3.1. The vertical lines indicate the depth in interaction lengths λ. Note that the amount of absorber material is not the same in all layers.

where

$$\mathrm{rms}^2(i) = \sum_j h_{ij}(j - \langle j \rangle_i)^2 \quad \text{and} \quad \langle j \rangle_i = \frac{\sum_j h_{ij} j}{\sum_j h_{ij}}.$$

The sum is over the wires (j) in the i-th layer.

ii) To subtract the primary minimum-ionizing track, hits are removed from the cluster (up to 3 neighboring hits) closest to the beam line in each chamber.

From the remaining hits a variable called *activity* (A) is calculated as follows:

$$A = \sum_i \mathrm{rms}^2(i)$$

where the sum is over all TRACAL layers. A is a measure of the shower spread and hit multiplicity.

The range (R) vs. activity (A) are plotted in Figure 3.6 for 100 GeV/c muons and pions. Most muon events have an activity $A = 0$ and the maximum range $R = 31$ and are separated from the pion events which have a larger activity and shorter range.

In Figures 3.7 a) and b), the activity distribution of all 100 GeV/c muons and pions are plotted. In Figure 3.7 a), most of the muon events are confined to the region near $A = 0$, however there is a long tail of muon events with high activity. It was found by visual scanning that these are muons accompanied by multiple δ - rays or an electromagnetic shower. In Figure 3.7 b), a peak at $A = 0$, assumed to be due to muon contamination, is clearly seen in addition to a broad peak at higher activity assumed to originate from pion showers. The origin of these two components becomes evident if one considers the activity distribution as a function of absorber depth.

In Figure 3.7 c), d) and e), the activity distribution of only those particles stopping before Station 1 ($R \leq 10\lambda$), between Station 1 and 2 ($10\lambda < R \leq 20\lambda$) and

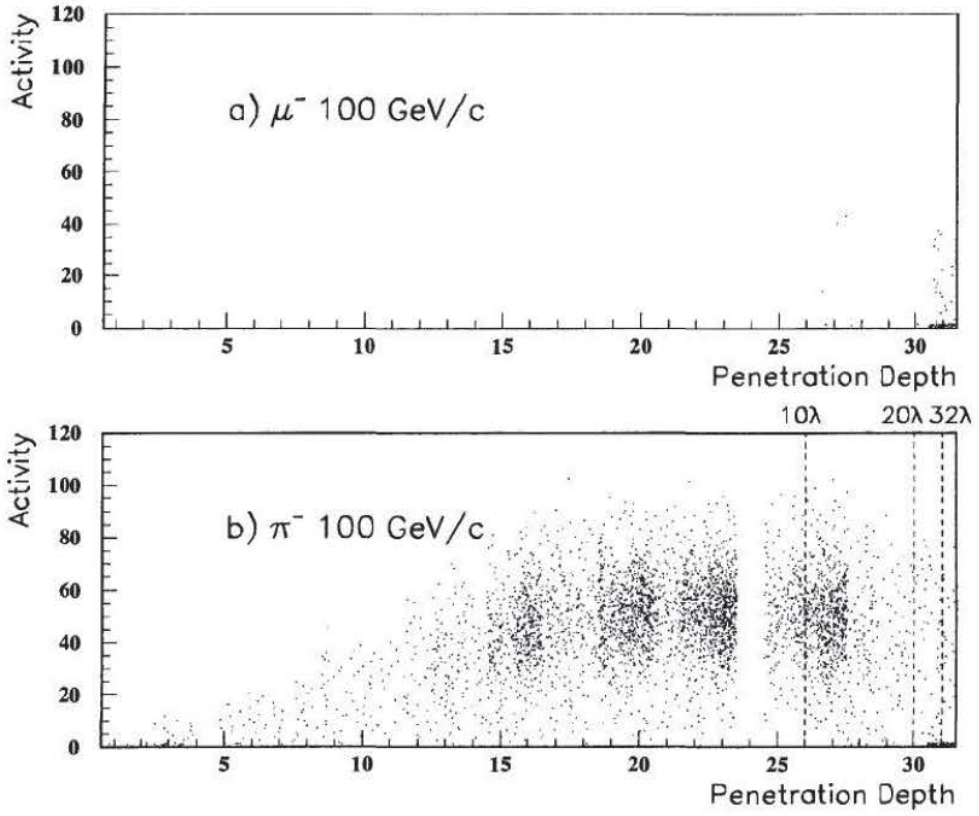

Figure 3.6: The distribution of range (R) and activity (A) for a) 100 GeV/c muons and b) 100 GeV/c pions. The vertical dotted lines indicate the range in interaction lengths λ.

after Station 3 ($R > 30\lambda$) are plotted, respectively. Going from Figure 3.7 c) to d) the height of the histogram reduces considerably, reflecting the absorption of pion showers, while the peak presumably due to the muon contamination is absent. In Figure 3.7 e), the peak at $A = 0$ is present indicating that these events are indeed muons penetrating the entire detector; one also sees a further reduction in the peak due to pion showers. By making a cut at $A = 20$ one is able to effectively exclude the muon background. The number of additional pion events in the region $A < 20$ is estimated by first assuming that the shape of the distribution in 3.7 e) is similar to the shape of the distribution in 3.7 d), therefore, the fraction of events with $A < 20$ should be the same in both cases. This correction factor is applied to determine the total number of pion events penetrating to this absorber depth. The number of muon events with activity $A > 20$ can be estimated by counting the fraction of muon events with $A > 20$ in Figure 3.7 a). This correction factor is also applied to the data.

The efficiency of the RPCs in the veto wall was about 95%, thus not all halo muons were rejected. In addition there were some muons entering the detector at large angles outside of the area of the veto wall. An additional muon background comes from the presence of halo muons which occurred in coincidence with normal hadronic showers. These events are characterized by having a large hadronic shower in the calorimeter followed by a muon track reaching Station 3. Events were identified as halo and rejected from the analysis if the muon track did not point back to the calorimeter. For the π^- beam (depending on the beam momentum), 30% to 40% of all tracks reaching Station 3 did not point back to the calorimeter. For the π^+ beam the fraction was about 10%. These numbers were verified by visually scanning a sample of all events reaching Station 3 (100 events of each data set).

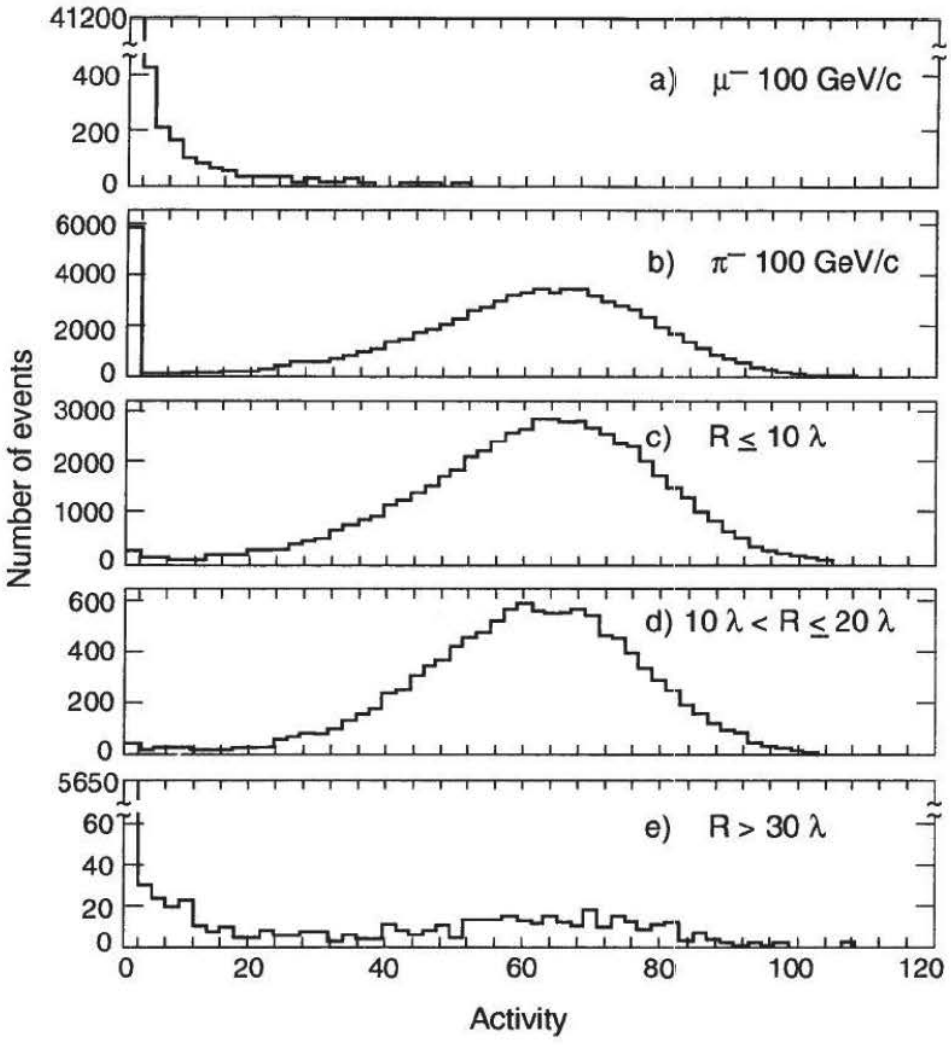

Figure 3.7: The distribution of activity (A) for a) 100 GeV/c muons, b) 100 GeV/c pions, c) only those pions stopping before Station 1 ($R \leq 10\lambda$), d) between Station 1 and 2 ($10\lambda < R \leq 20\lambda$) and e) after Station 3 ($R > 30\lambda$).

For momenta less than 100 GeV/c, the pion beam also contained a small electron contamination. The amount of contamination was estimated from the number of particles which stopped in the 29 X_0 lead brick wall installed in front of TRACAL and was measured to be less than 0.05 % at 30 GeV/c. The lead was not instrumented; consequently, it was not possible to determine the exact nature of the particles stopping there. This uncertainty was included in the estimate of the total systematic error in the punchthrough probability.

3.2.2 Description of Monte Carlo Simulation

Simulations of the RD5 experiment [44] have been performed for five different momenta of π^- beam and one momentum of K^+. A primary purpose of the simulation is to validate the GEANT code, so that confidence may be held in its predictions concerning detector designs that are based on this widely used simulation program. The detectors included in the simulation were TRACAL, the RPCs, and the muon drift chambers. Also included in the simulation were both magnets (M1 and M2), the lead brick in front of TRACAL and some concrete supports for magnet M2. The simulation accounted for the 1.5 T field of M2 and two different field conditions of M1, 0 and 3 T.

GEANT version 3.21 [45] was used for the simulation. Hadronic interactions were treated with the hadronic shower generators GHEISHA [46] and FLUKA [47], for 10, 30, 50, 100 and 300 GeV/c negative pions, and GHEISHA, for 50 GeV/c positive kaons. The number of events generated for each momentum value, particle type and magnetic field value are presented in Tables 3.3 and 3.4.

All charged particle hits were digitized and written to a file in the same format as the real data; these data were then processed with the same analysis program

Table 3.3: Number of π^- and K^+ events generated using GEANT 3.21 and hadronic shower generator GHEISHA.

momentum [GeV/c]	Magnetic field strength	
	0 T	3 T
	Event statistics, π^-	
10	14500	16500
30	10800	12400
50	7500	8100
100	7400	13400
300	3100	3400
	Event statistics, K^+	
50	9000	8040

Table 3.4: Number of π^- events generated using GEANT 3.21 and hadronic shower generator FLUKA.

momentum [GeV/c]	Magnetic field strength	
	0 T	3 T
	Event statistics, π^-	
10	14500	19500
30	12000	10000
50	10560	8100
100	6600	8200
300	2400	3000

used for the real data. The digitization of TRACAL detectors took into account the honeycomb cell structure surrounding the wires (see Ref. [38]), and encoded the drift time for the wires and induced charge for the strips. The RPC digitization encoded a bit for each hit strip, just as for the real data, and drift times were digitized for the muon drift chambers.

The GEANT energy cuts used were 1 MeV for all types of particles in the absorbers, and 10 keV for electrons and gammas in the sensitive volumes of the detectors. The lower cuts in the sensitive volumes allowed neutral particles to interact and produce low-energy electrons which could then be counted as hits. The GEANT flags used to control physics processes were all set to 1. The beam spot, as measured by the MWPCs, was found to be well represented by a gaussian distribution.

Detector Acceptance Simulation

For depths less than 10λ (< 1.69 m iron eq.), the geometrical acceptance of the RD5 detector is determined by the size of TRACAL. Each stainless steel plate in TRACAL covers an area $0.8 \times 1.0\,\mathrm{m}^2$. For depths greater than 10λ, the geometrical acceptance is determined by the height of magnet M2, which covers the area between 0.8 m above and below the beam line. The limited acceptance is particularly evident when one turns on the magnet M1. With the M1 field at 3 T, particles may exit the calorimeter at large angles and be deflected outside the acceptance of magnet M2. In order to estimate the losses due to the finite detector acceptance, an additional GEANT simulation was run in which the size of TRACAL and magnet M2 were expanded to cover the entire area ($3.2 \times 3.8\,\mathrm{m}^2$) of the muon drift chambers. Negative pions were generated with incident momentum of 30, 100 and 300 GeV/c. Data were generated with M1 at 0 T and 3 T.

The simulated data were first analyzed accepting all hits recorded over the entire area of TRACAL and the muon drift chambers. Next, the same data were reanalyzed, excluding all hits which lay outside the area defined by the actual RD5 detector. The loss due to detector acceptance was estimated by calculating the difference between the punchthrough probability at a given depth obtained from the simulation with the enlarged geometry, and the punchthrough probability at that same depth obtained from the simulation with the normal RD5 geometry.

It was found that the acceptance loss inside of TRACAL, for both M1 field conditions, was very small (averaging less that 1% but increasing with depth inside the absorber). The showers were well contained within the calorimeter volume. For the detectors behind TRACAL, i.e. muon stations 1, 2 and 3, the acceptance losses were larger. For the data with M1 at 3 T the loss at muon station 1 was found to be $7.3 \pm 1.4\%$ and increased to about 50% at muon station 2.

3.2.3 Results

Total Punchthrough Probability of Hadronic Showers

In Figures 3.8, 3.9, 3.10 and 3.11 we present the total punchthrough probability of hadronic showers as a function of meters of equivalent iron for negative and positive pions, positive kaons and protons. The results with M1 at full field (3 T) and M1 off (0 T) are compared. The numerical values of these measurements and additional measurements taken with M1 at half field (1.5 T) are presented in Appendix B.

These curves are characterized by two distinct regions. For example, consider the 100 GeV/c π^- data (Figure 3.9). For depths less than about 3 m iron eq., the curve has a steep slope which represents the absorption of the hadronic component of the shower as a function of increasing absorber depth. For depths greater than

3 m iron eq. the curve flattens out; this represents the ranging out of penetrating punchthrough muons produced as a component of the hadronic shower.

The total punchthrough probability of 10 GeV/c negative pions, for both field conditions (3 T and 0 T), and 20 and 30 GeV/c negative pions, for a M1 field of 3 T, was only measured up to the level of Station 1 (approximately 10λ). This is because of background muons - coming from pion decay upstream of the detector - in the data sample, which were not removed by our muon subtraction algorithm. We regard as muons those events having one minimum ionizing track in TRACAL and a penetration depth up to Station 3 (see Section 3.2 for details). For a large number of muons in the lower momentum pion beams, this definition fails because many of these muons are bent by the magnetic field outside the acceptance of Station 3. The fraction of background muons lost from the 10 GeV/c pion beam was estimated by analyzing the 10 GeV/c muon data. It was found that 30% of these muons were bent out of the acceptance of the detector between Station 2 and Station 3 while another 5% were lost between Station 1 and Station 2.

Next, we compare the total punchthrough probability of positive pions and kaons. In Figure 3.12, one sees that the punchthrough probability of 100 GeV/c positive pions is less than that of positive kaons, for a given depth. This difference is explained by the fact that the π^+ and K^+ inelastic cross sections per nucleon, at 100 GeV/c, are about 23 mb and 17 mb, respectively [48]. On average, positive pions will have a primary hard interaction earlier in TRACAL, relative to positive kaons, and, as a result, have a larger amount absorber available after the primary interaction to stop the remaining shower. Furthermore, kaon-induced showers will contain more secondary kaons which have a higher probability to decay [49].

In Figures 3.13, 3.14 and 3.15 we compare the total punchthrough probability of

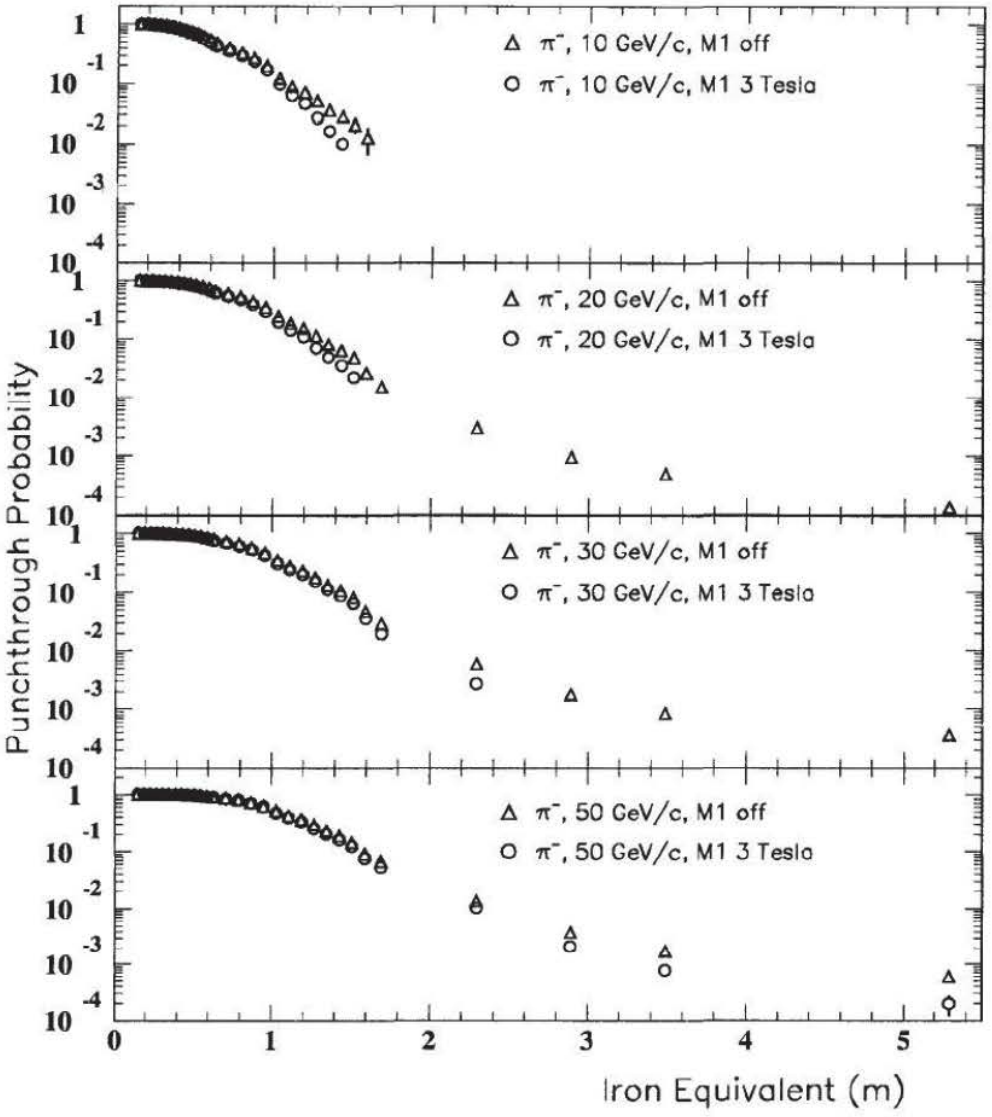

Figure 3.8: Total punchthrough probability as a function of meters of equivalent iron for 10, 20, 30 and 50 GeV/c negative pions. We compare data taken with the M1 field at 3 T and M1 off.

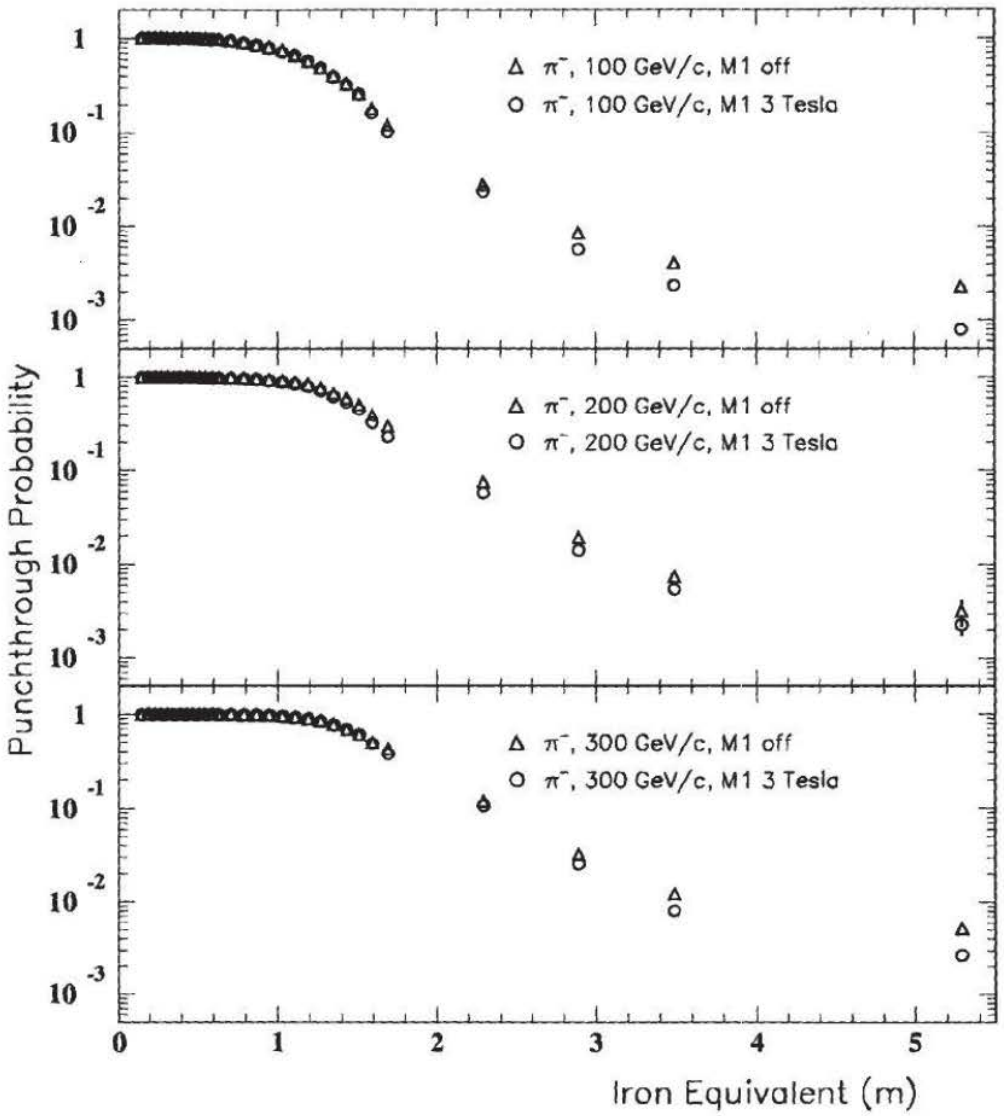

Figure 3.9: Total punchthrough probability as a function of meters of equivalent iron for 100, 200 and 300 GeV/c negative pions. We compare data taken with the M1 field at 3 T and M1 off.

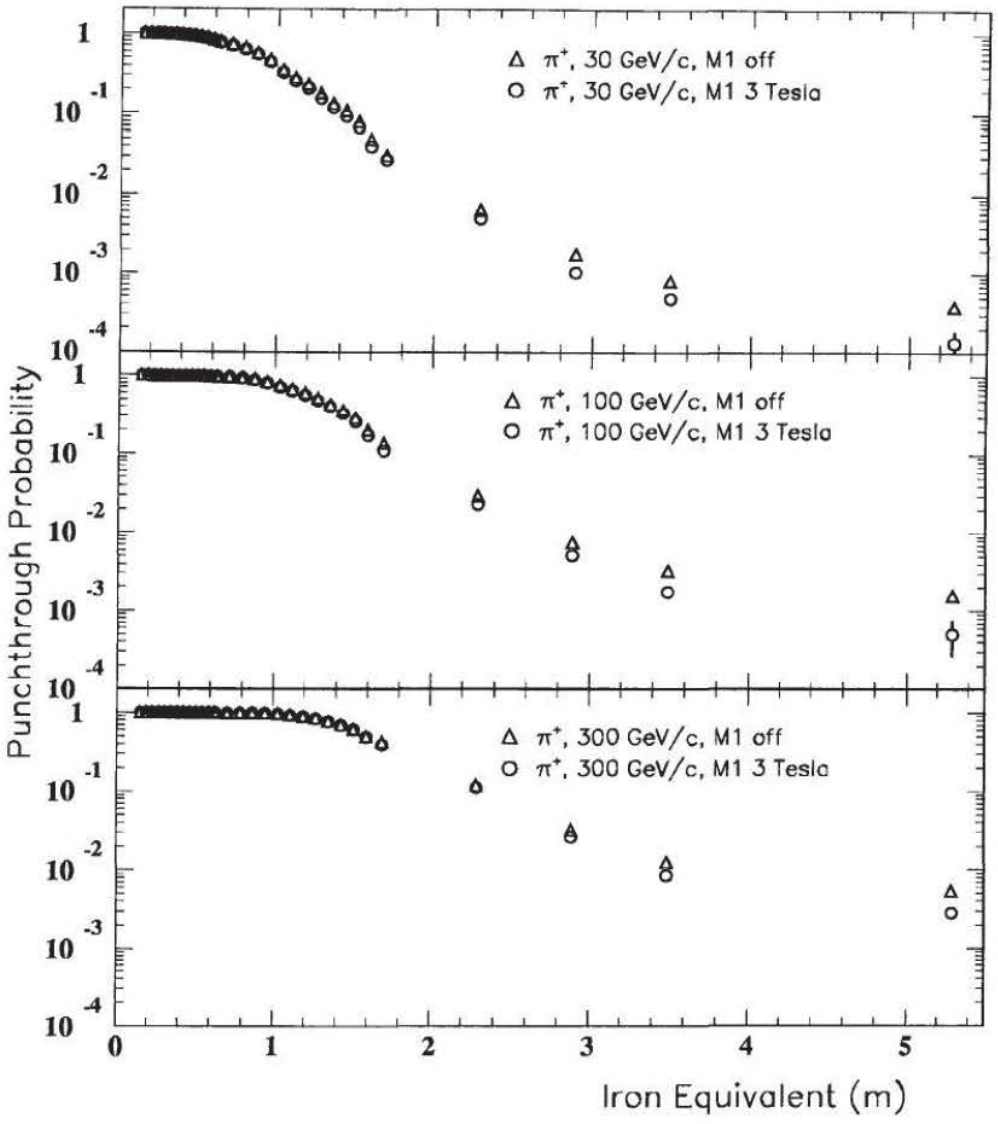

Figure 3.10: Total punchthrough probability as a function of meters of equivalent iron for 30, 100 and 300 GeV/c positive pions. We compare data taken with the M1 field at 3 T and M1 off.

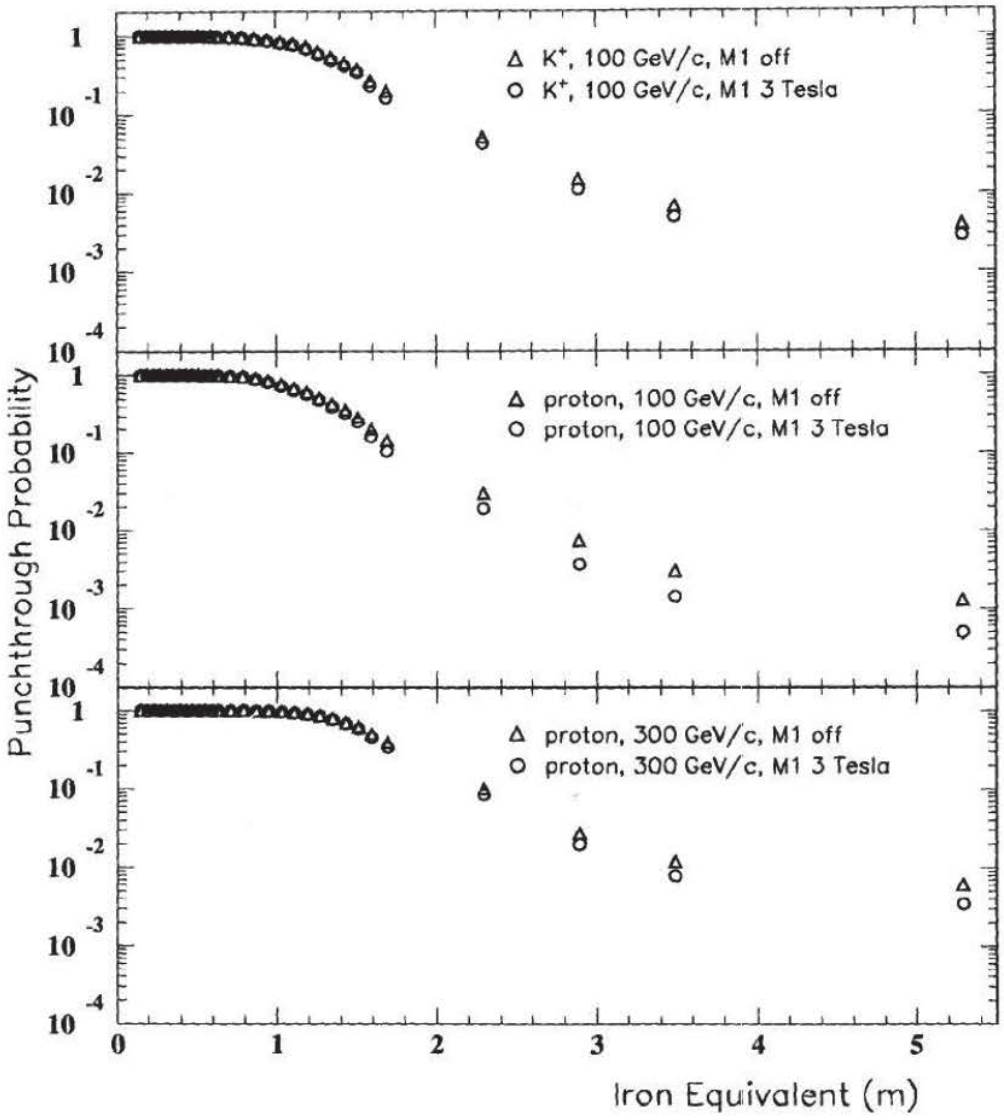

Figure 3.11: Total punchthrough probability as a function of meters of equivalent iron for 100 GeV/c positive kaons and 100 and 300 GeV/c protons. We compare data taken with the M1 field at 3 T and M1 off.

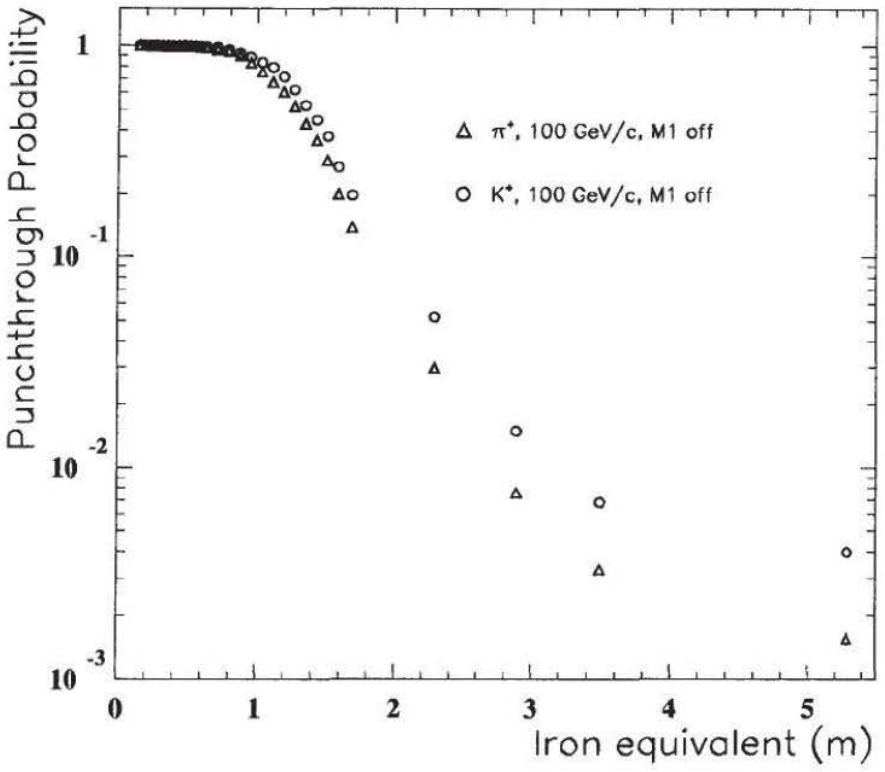

Figure 3.12: The total punchthrough probability, as a function of meters of equivalent iron, of 100 GeV/c positive pions and positive kaons are compared.

simulated negative pions with the real data. The solid line indicates the simulation results with M1 at full field and the dotted line with M1 off. The statistical errors for the simulated data are shown at the last bin. The errors on all preceding bins are smaller. Figures 3.13 and 3.14 show the results obtained with hadronic shower generators GHEISHA and FLUKA, respectively. In Figure 3.15 we present the results obtained with both GHEISHA and FLUKA compared with 10 GeV/c negative pion data. The scale of Figure 3.15 only extends to 2 m of iron equivalent in order to magnify the area of interest for 10 GeV/c data. The agreement between both hadronic shower generators and the real data is good, with FLUKA exhibiting a somewhat better agreement at low momentum, i.e. 10 and 30 GeV/c.

The total punchthrough probability of 50 GeV/c positive kaons is compared, in Figure 3.16, with results obtained using GHEISHA. The real data were taken with M1 at full field.

Finally, we investigate the muon composition of the punchthrough showers as a function of absorber depth. In Figure 3.17, the muon component of simulated showers originating from 50 GeV/c negative pions is indicated by the dashed line. The particle identification information was recorded while running the simulation. The dashed line indicated the proportion of simulated events with a muon present either at that depth or a greater depth. Both hadronic shower generators predict that hadronic punchthrough dominates until about 10λ (1.6 m iron equivalent), and punchthrough muons at greater depths.

Further properties for hadronic showers were investigated, including, the shower lateral distribution, as measured by TRACAL wires, and the total charged particle multiplicity as measured by TRACAL wires and RPC strips.

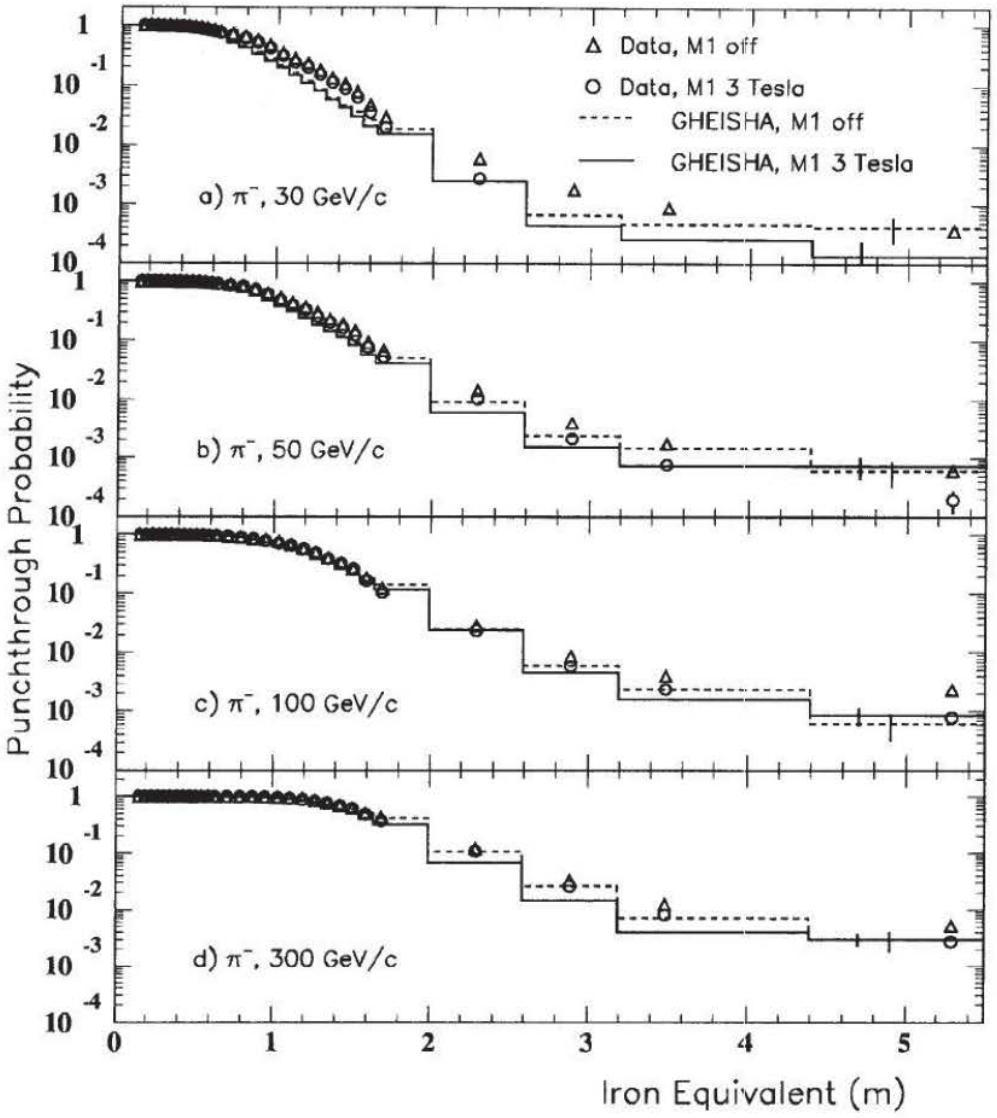

Figure 3.13: The total punchthrough probability as a function of meters of equivalent iron of 30, 50, 100, and 300 GeV/c simulated negative pions are compared with the results of analysis of real data. Hadronic interactions were simulated using GHEISHA. The statistical error for the simulated data is shown for the last bin.

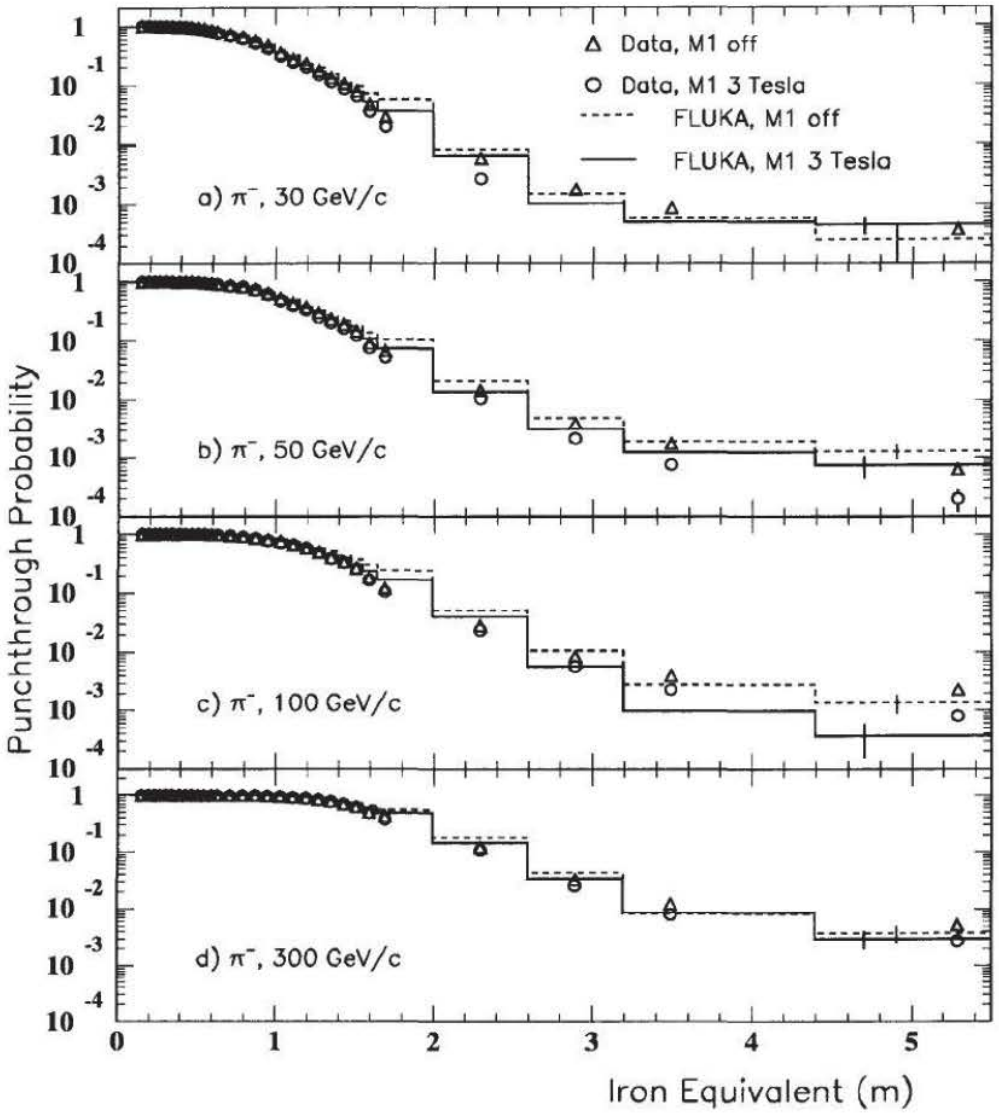

Figure 3.14: The total punchthrough probability as a function of meters of equivalent iron of 30, 50, 100, and 300 GeV/c of simulated negative pions are compared with the results of analysis of real data. Hadronic interactions were simulated using FLUKA. The statistical error for the simulated data is shown for the last bin.

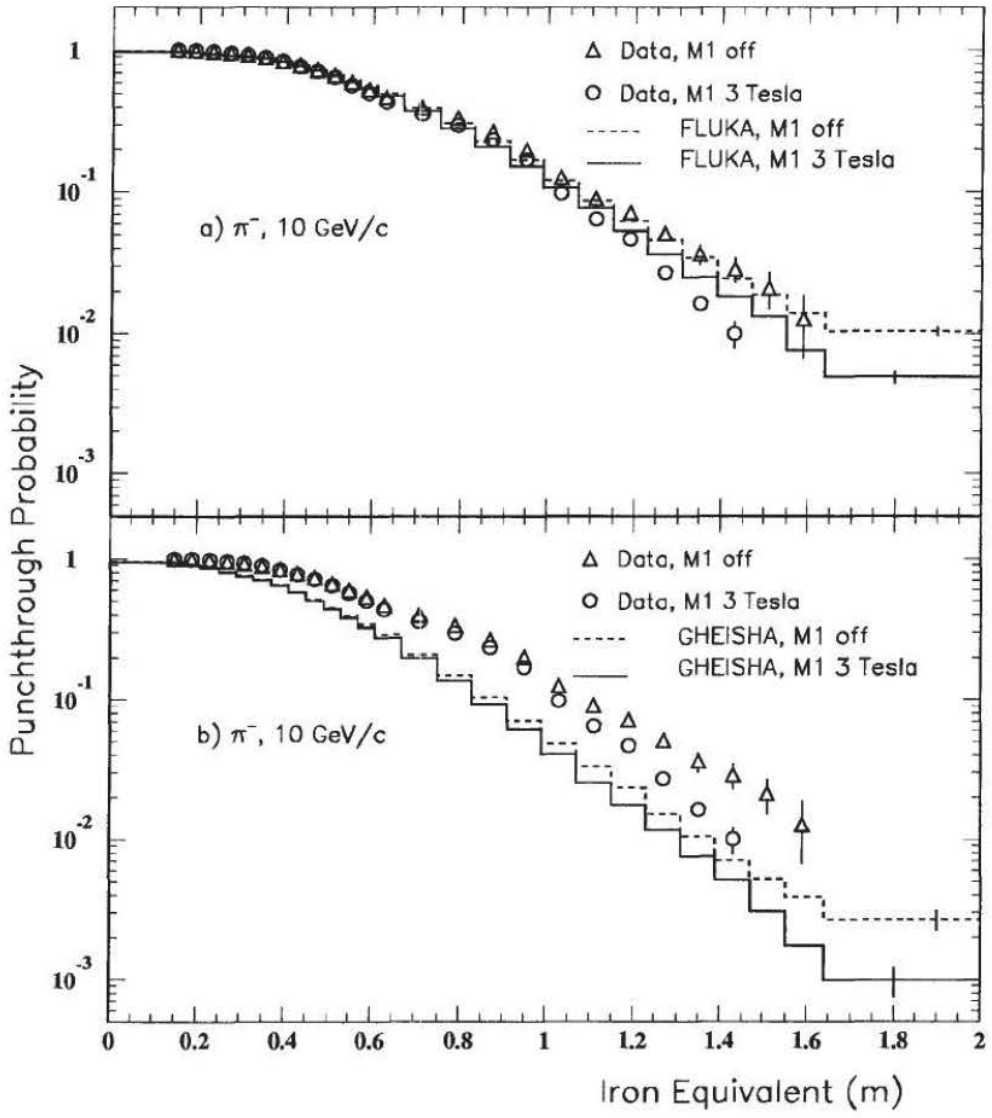

Figure 3.15: The total punchthrough probability as a function of meters of equivalent iron of 10 GeV/c simulated negative pions is compared with the results of analysis of real data. In a) hadronic interactions were simulated using FLUKA, in b) using GHEISHA. The statistical error for the simulated data is shown for the last bin.

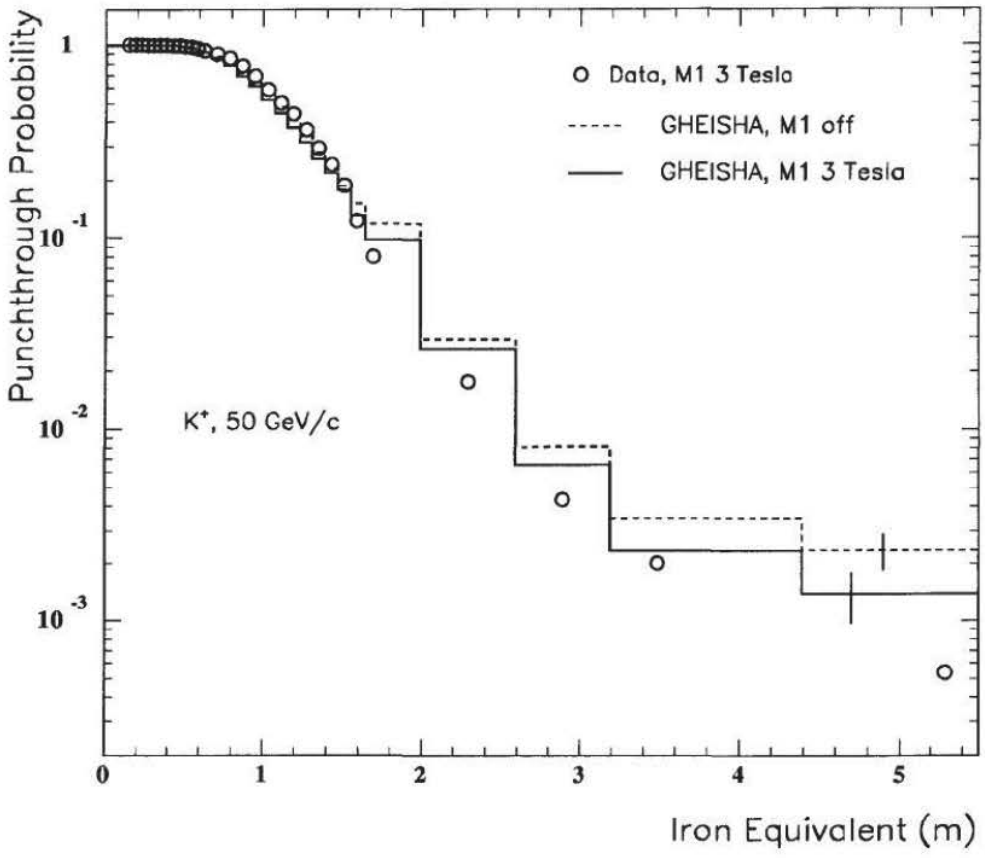

Figure 3.16: The total punchthrough probability as a function of meters of equivalent iron of 50 GeV/c simulated positive kaons is compared with the results of analysis of real data. Hadronic interactions were simulated using GHEISHA. The statistical error for the simulated data is shown for the last bin.

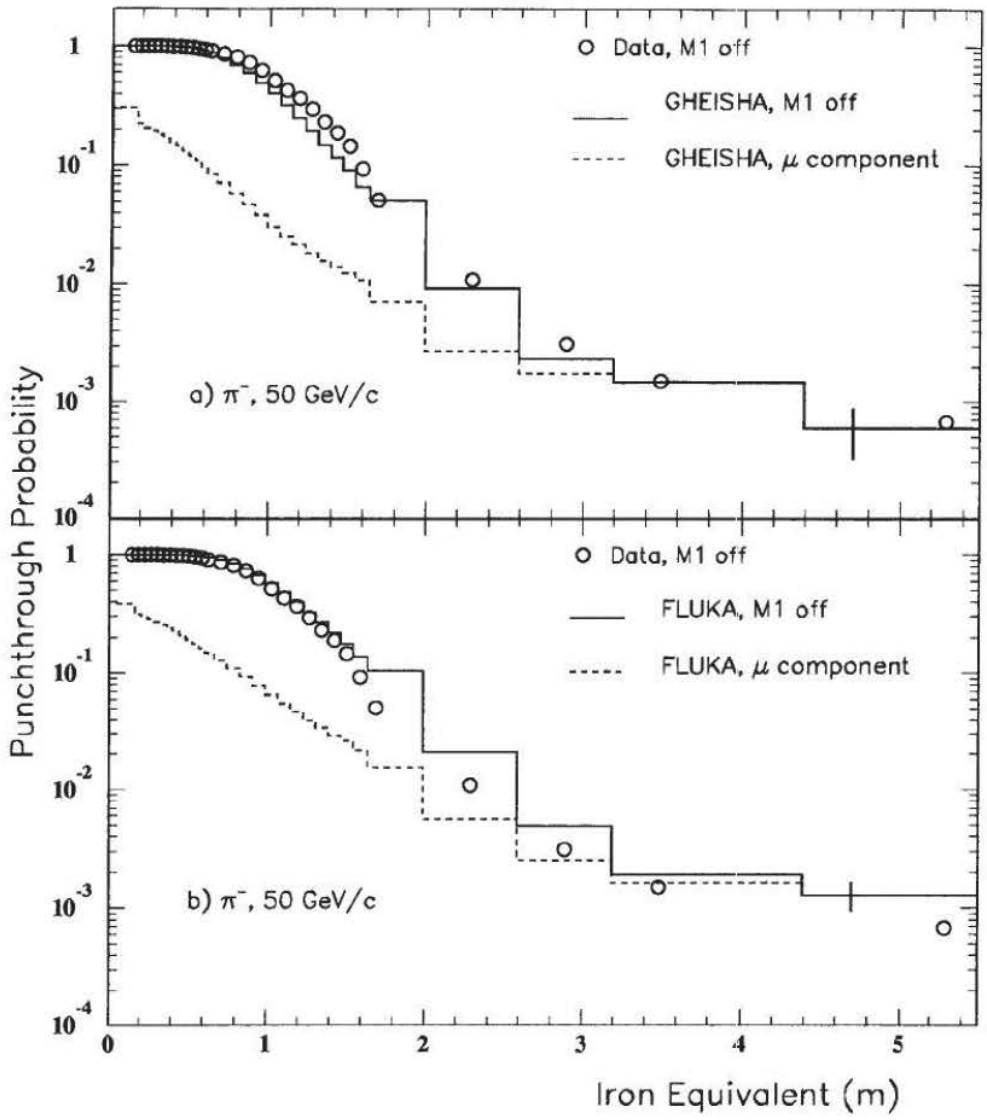

Figure 3.17: The total punchthrough probability, as a function of meters of equivalent iron, of 50 GeV/c simulated negative pions is plotted as a solid line with the muon component indicated as a dashed line. In a) hadronic interactions were simulated using GHEISHA, in b) using FLUKA. The statistical error is shown for the last bin.

Shower Lateral Distributions

Figure 3.18 shows the distribution of hit wires in TRACAL layers 8 and 21, at about 2.5λ and 7.5 λ, respectively. These layers were chosen to be representative of the shower at two different points: at the beginning and end of the shower development. The simulation results obtained with GHEISHA and FLUKA are compared with real data. The incident beam particles were 50 GeV/c negative pions and the magnet M1 was off. Each TRACAL layer consisted of 48 anode wires strung in the center of drift cells; the wire pitch is 12.7 mm. As seen in Figure 3.18 a), only the 32 central wires of layer 8 were instrumented. Figure 3.19 shows the same distribution just described but with the M1 field at 3 T. On each figure, 0 cm indicates the nominal beam position. The wire hit distributions in Figures 3.18 and 3.19 have all been normalized by the total number of events in order to better compare their shapes. It is seen that the simulation results agree well with the real data.

Shower Multiplicity Distribution

Figure 3.20 shows the TRACAL hit wire multiplicity in layers 8 and 21 for 50 GeV/c negative pions compared with predictions of the simulation. The histograms are normalized by the total number of events in order to better compare their shapes. Figure 3.21 shows the same distributions for M1 at 3 T. The number of events with zero multiplicity are not shown. As before, these layers were chosen to be representative of the shower at two different points: at the beginning and end of the shower development.

The multiplicity of hit RPC strips is presented in Figure 3.22 for 30, 50, 100 and 300 GeV/c negative pions as the incident particles. The RPC chambers used were in muon station 1, at a depth of 10λ. Again, the number of events with zero multiplicity

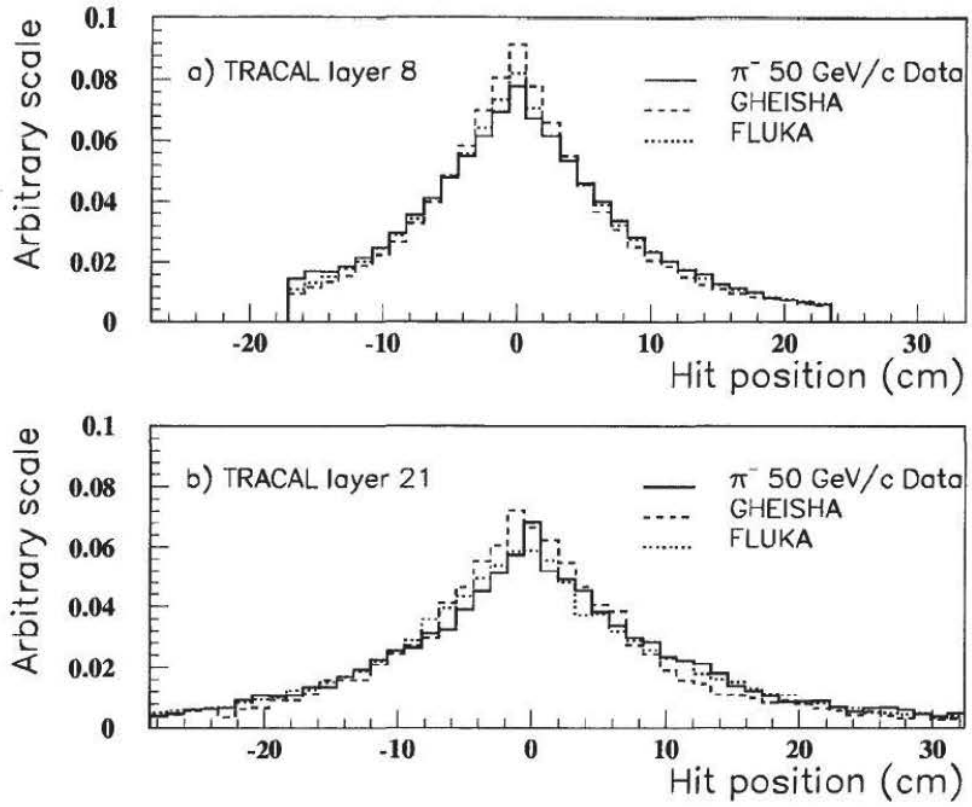

Figure 3.18: Hit profile of TRACAL wires, for data taken with M1 off, at a) layer 8 ($\approx 2.5\lambda$), and b) layer 21 ($\approx 7.5\lambda$). The real 50 GeV/c negative pion data (solid line) is compared with data simulated using GHEISHA (dotted line) and FLUKA (dashed line) to simulate hadronic interactions. The wire pitch is 12.7 mm. The histograms have been normalized by the total number of events.

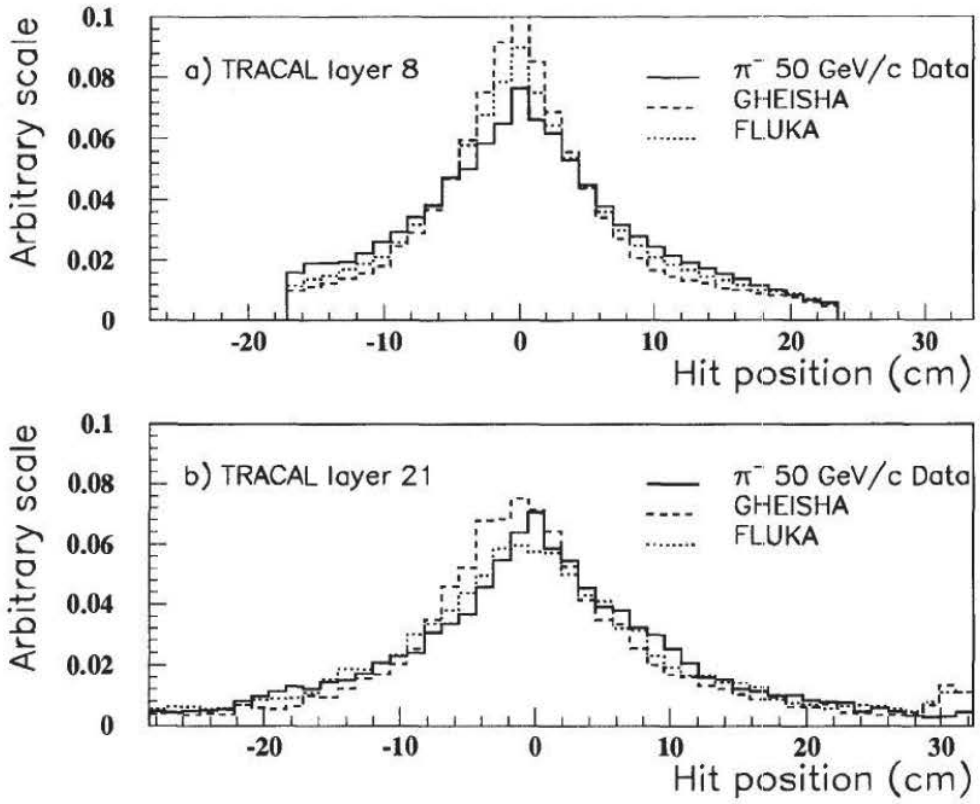

Figure 3.19: Hit profile of TRACAL wires, for data taken with a M1 of 3 T, at a) layer 8 ($\approx 2.5\lambda$), and b) layer 21 ($\approx 7.5\lambda$). The real 50 GeV/c negative pion data (solid line) is compared with data simulated using GHEISHA (dotted line) and FLUKA (dashed line) to simulate hadronic interactions. The wire pitch is 12.7 mm. The histograms have been normalized by the total number of events.

are not shown. The experimental results are compared with the GEANT simulation. Both hadronic shower generators, GHEISHA and FLUKA, were used. The agreement of both hadronic shower generators is good. The apparent disagreement in Figure 3.22 d), for RPC strip multiplicity greater than 30, is due to a lack of statistics for the simulated data.

We continue the investigation of the multiplicity of hit RPC strips in muon station 1 by imposing the further requirement that each punchthrough event also reaches Station 2, at a depth of about 20λ. The results are presented in Figure 3.23, for 30, 50, 100 and 300 GeV/c negative pions as the incident particles. We can remark that the punchthrough particles reaching Station 2, which originate from 30 GeV/c pion showers, are mainly muons. From the analysis of 30 GeV/c muon data, it was found that muons produce on average 1.5 hit RPC strips. Therefore punchthrough particles reaching Station 2 which originate from 30 GeV/c incident pions are characteristically muons when emerging from the calorimeter. In contrast, for the 300 GeV/c pion data, the particles reaching Station 2 are accompanied in Station 1 by a large number of additional hits, possibly soft hadrons and electrons, the remnant of the primary hadronic cascade.

3.3 Momentum and Angular Distribution of Punchthrough Muons

While the momentum and angular distributions of prompt and decay muons can be readily calculated, the same calculation for muons generated in a hadronic cascade is more complicated and involves supplementary shower generators. In RD5 we measured these distributions for punchthrough muons that reach a depth of at least $20\,\lambda$.

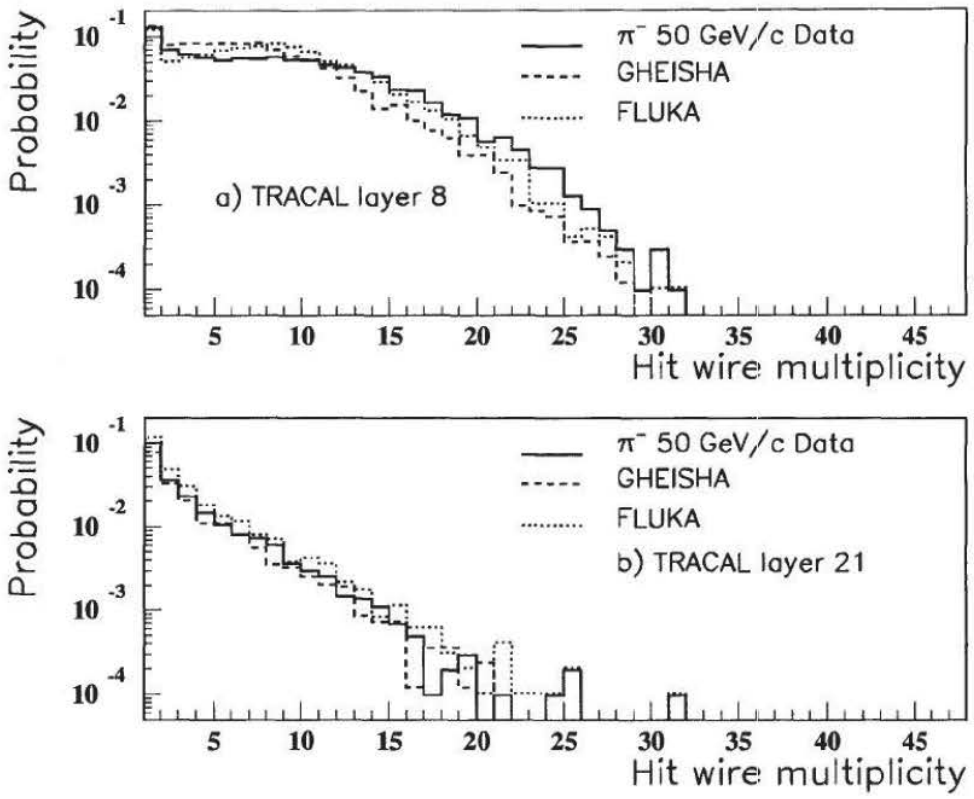

Figure 3.20: Multiplicity of hit TRACAL wires, for data taken with M1 off, at a) layer 8 ($\approx 2.5\lambda$), and b) layer 21 ($\approx 7.5\lambda$). We compare real 50 GeV/c negative pion data (solid line), with data simulated using GHEISHA to (dotted line) and FLUKA (dashed line) to simulate hadronic interactions. The number of events with zero multiplicity are not shown. The histograms have been normalized by the total number of events.

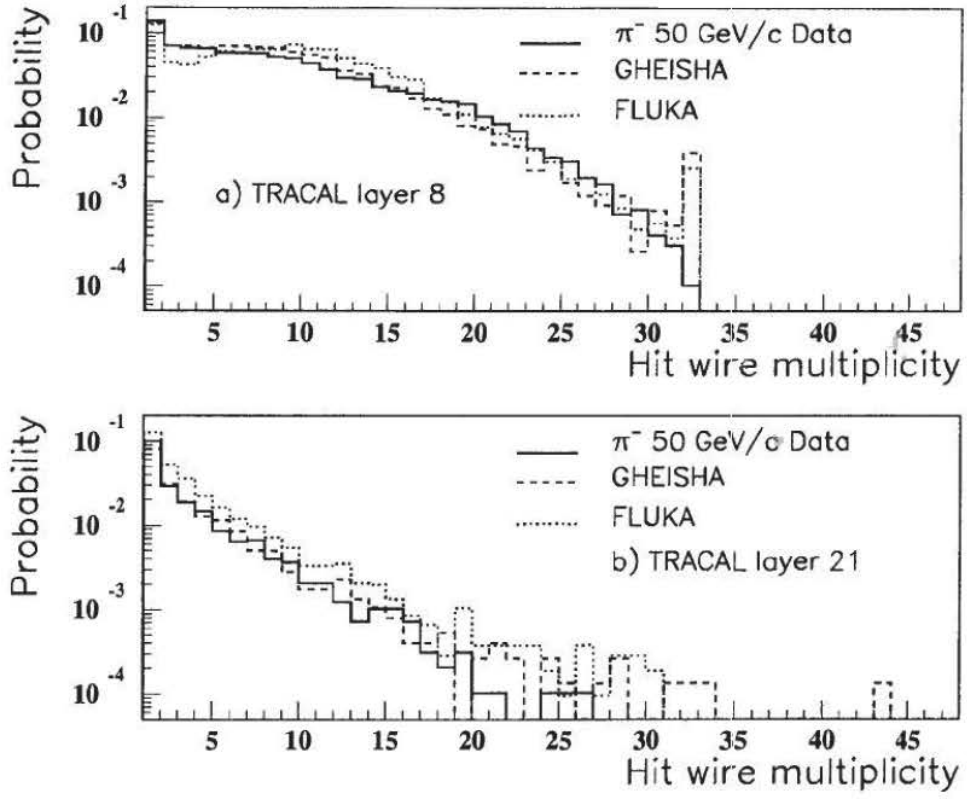

Figure 3.21: Multiplicity of hit TRACAL wires, for data taken with the field of M1 at 3 T, at a) layer 8 ($\approx 2.5\lambda$), and b) layer 21 ($\approx 7.5\lambda$). We compare real 50 GeV/c negative pion data (solid line), with data simulated using GHEISHA to (dotted line) and FLUKA (dashed line) to simulate hadronic interactions. The number of events with zero multiplicity are not shown. The histograms have been normalized by the total number of events.

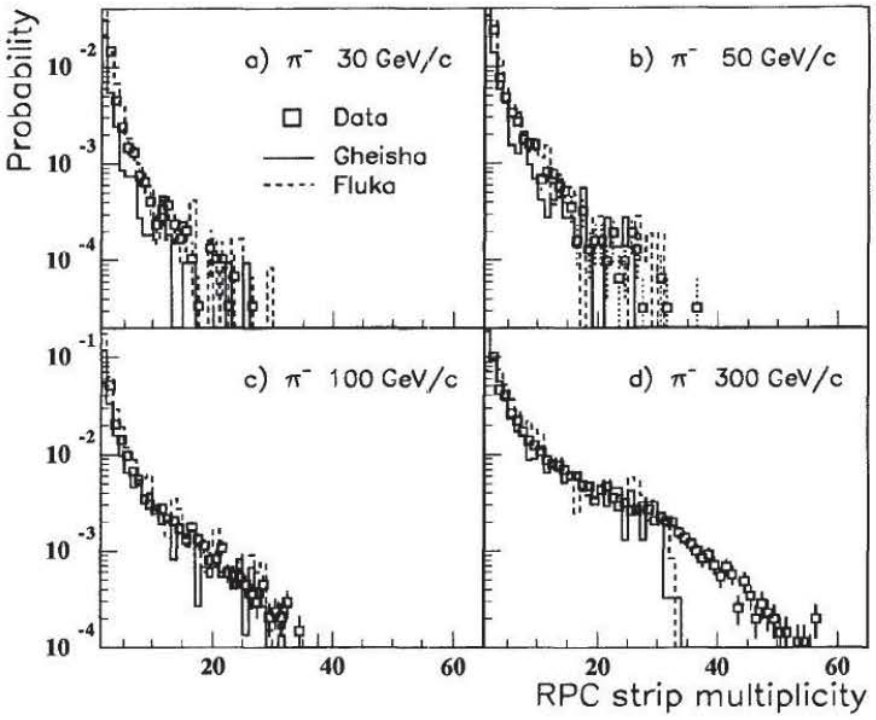

Figure 3.22: Multiplicity of hit RPC strips in Station 1 ($\approx 10\lambda$) from showers originating from negative pions of momenta a) 30 GeV/c, b) 50 GeV/c, c) 100 GeV/c and d) 300 GeV/c. The data were taken with the magnet M1 off. We compare the results from analysis of real data (open squares) with data simulated using GHEISHA (solid line) and FLUKA (dashed line) to simulate hadronic interactions. The number of events with zero multiplicity are not shown. The histograms have been normalized by the total number of events.

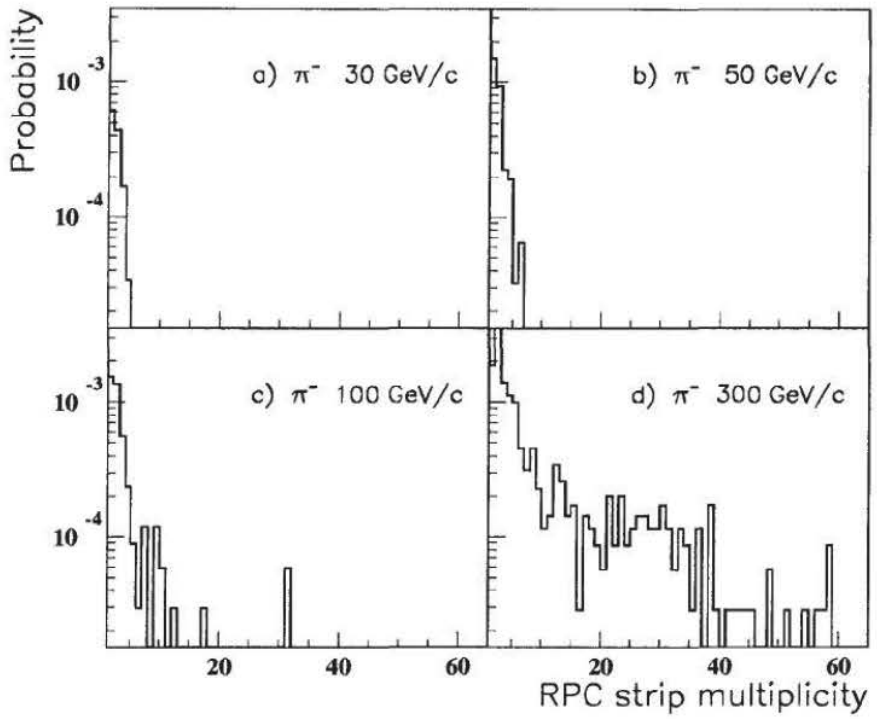

Figure 3.23: Multiplicity of hit RPC strips in Station 1 ($\approx 10\lambda$) when we require that there is also a hit recorded in Station 2 ($\approx 20\lambda$). The showers originated from negative pions of momenta a) 30 GeV/c, b) 50 GeV/c, c) 100 GeV/c and d) 300 GeV/c when a hit is recorded in Station 2 ($\approx 20\lambda$). The data were taken with the magnet M1 off. The histograms have been normalized by the total number of events.

In Section 3.3.1, we describe the event selection and reconstruction algorithm used for this analysis. The results are presented in Section 3.3.2 as absolute momentum spectra. The results are compared with Monte Carlo predictions.

3.3.1 Data Sample and Analysis Method

The data used for the momentum analysis were taken during the 1993 runs. The analysis included data sets with different energies and particle types. As in the measurement of total punchthrough, data were taken with the MB and 10λ trigger. The normalization factor for the $10\,\lambda$ trigger was calculated by counting the number of events in the MB data, which also satisfied the $10\,\lambda$ trigger condition. In Table 3.5, we present the event statistics used in the momentum analysis. The total number of events listed, for each particle type, are the sum of MB and 10λ triggers, after the number of 10λ triggers has been divided by the trigger normalization factor. This sum represents the number of MB events one would have to take in order to get the same event statistics reaching a depth of 10λ. For each of these data sets in Table 3.5 we also took some data with a muon beam for background estimation and detector calibration.

As in the study of total punchthrough, the hadron beams contained a large muon contamination which had to be subtracted offline. The variable *activity* (A), which is described above in Section 3.3, was used to separate the muon contamination from the hadron beam. In Figure 3.24, the activity distribution of $30\,\mathrm{GeV}/c$ and $300\,\mathrm{GeV}/c$ pions and muons is shown as an example; the vertical scale in arbitrary. The cut values used to separate pions from muons was $A = 5$, for $30\,\mathrm{GeV}/c$, and $A = 40$, for $300\,\mathrm{GeV}/c$. The separating power of this variable is poor for low beam momenta, and increases with the momentum. The signal losses due to this cut, for each beam

momentum	particle type							
[GeV/c]	π^-		π^+		K^+		proton	
	statistics, M1 field 0 T							
20	2031 k	294						
30	1224 k	459	1307 k	460				
50	1618 k	1033						
100	687 k	1121	365 k	522			862 k	1096
200	255 k	880						
300	325 k	1502	217 k	869			208 k	873
	statistics, M1 field 1.5 T							
30	866 k	297						
100	735 k	1047						
300	208 k	857						
	statistics, M1 field 3 T							
20	2254 k	175						
30	941 k	204	2022 k	236				
50	1055 k	276			667 k	311		
75							880 k	324
100	791 k	708	165 k	106	195 k	217	302 k	171
200	277 k	530						
300	322 k	812	114 k	261			141 k	329

Table 3.5: Event statistics for momentum analysis. The first column of each particle type gives the sum of MB and 10 λ data (in thousands of events). The number of 10 λ triggers was divided by the trigger normalization factor. The second column gives the number of events with at least one track that passed all cuts.

energy, were calculated by subtracting the normalized activity distribution of the muon beam from the activity distribution of the pion beam and then counting the number of events that fail the cut. The muon distribution was normalized to have the same number of entries, with activity less than 1.5, as the pion distribution. The signal loss was estimated to be 6.7±0.4% for the 30 GeV/c beam and drops to 2.4±0.1% for the 300 GeV/c beam. The signal loss was confirmed by scanning some of the rejected events for several energies.

A sample of the accepted events were scanned (100 events of each sample) to determine the amount of background remaining. The identified background events were about 10% for the 30 GeV/c π^- beam and dropped to about 2% for the 300 GeV/c π^- beam. The momentum spectra of the signal lost due to the activity cut and the remaining background events are both flat over the whole momentum range with a slight increase at half the beam momentum. (For this comparison we use the relative momentum and combine the data of all beam momentum.) Thus the background subtraction and signal loss correction almost cancel each other. We made no background subtraction and signal loss correction, but added an adequate systematic error (from 5% for 30 GeV/c down to 1% for 300 GeV/c).

Using this method to separate the muon contamination from the hadron beam, a hadron, penetrating the whole calorimeter without interaction or decaying before the first hard interaction, is identified as "muon" and rejected. Our detector does not provide any means to separate these events from the muon background. The probability that a hadron will penetrate the entire calorimeter (10 λ of iron) and have no hard interaction is about 5×10^{-5}. A further factor 10 reduction in this background occurs because each non-interacting hadron must also penetrate through the first half of the absorber magnet (1.8 m iron) in order to reach Station 2 and

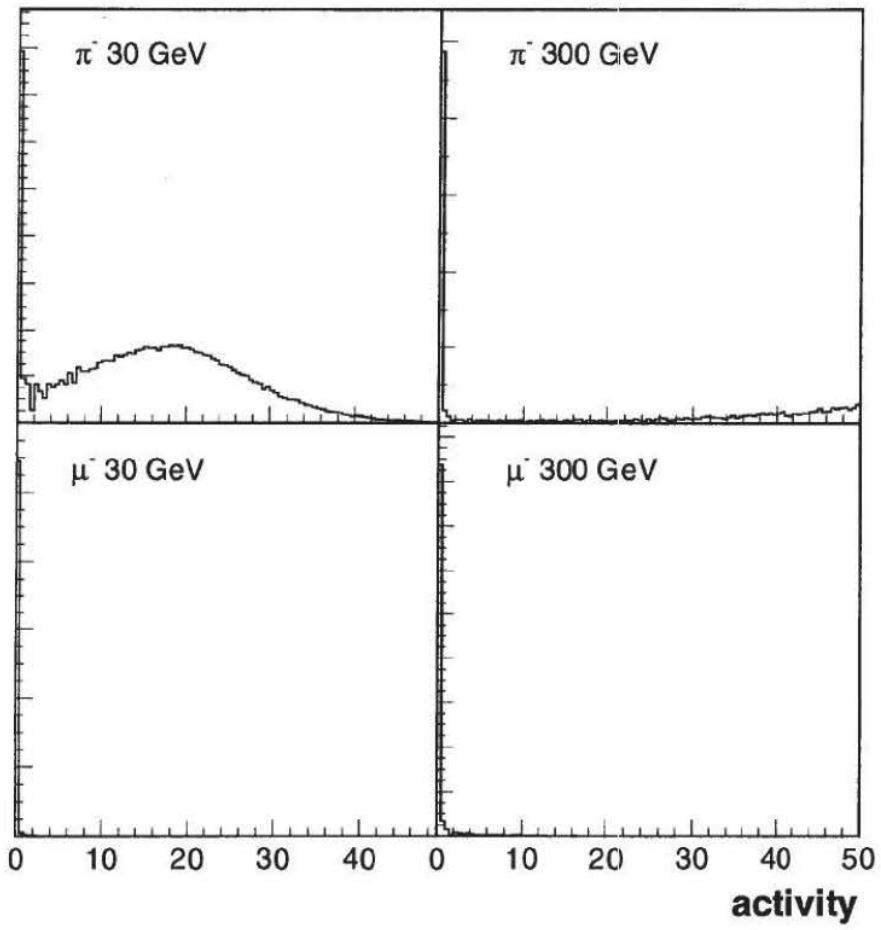

Figure 3.24: Example of an activity distribution for 30 GeV/c and 300 GeV/c pions and muons. The vertical scale is arbitrary. The cut values used to separate pions from muons was 5 for 30 GeV/c and 40 for 300 GeV/c.

become a candidate for reconstruction.

An additional muon background arose from hadrons which began to shower upstream of the calorimeter. For the low beam energies the beam had a wide profile and hadrons showered frequently in shielding and trigger devices just upstream of the detector (10 % of the selected events for a 30 GeV/c beam). These secondaries had a high chance to decay, giving an additional muon background. These events were characterized by having a large number of tracks in one or both MWPC chambers. Events having two or more tracks in both MWPCs, or having more than two tracks in any of the MWPCs, were rejected as multi-particle events. The MWPC cut removed almost all of these events. On the other hand, due to noise and e.m. secondaries, the MWPC gave wrong multiplicities from time to time. This effect was measured with muon data and the MWPC efficiency was found to be $91.8 \pm 0.2_{stat} \pm 1_{sys}$ %, independent of beam energy and also stable with time. Since this cut was only applied for selected events, the MWPC efficiency had to be corrected for.

To fit the momentum, we selected only the events with at least one track in the second muon station, thus requiring the particle to penetrate at least $20\,\lambda$ of absorber. One has to keep that in mind when looking at our results, where we give the distributions for a reference depth of $10\,\lambda$. For each track in the second muon station we searched for matching tracks in the first and third muon station, requiring to find at least one. These track candidates were then fit using the GEANE package of the GEANT library.

The fitted track was rejected as beam halo if it did not point back to the calorimeter. It was checked, that this cut caused no signal loss, however, halo muons penetrating the calorimeter were not rejected.

After the fit and applying the cuts we produced the spectra shown in Section 3.3.2.

Given in Table 3.5, in addition to the total events statistics, are the number of events, for each data set, with at least one track that passed all cuts. If there was more than one track, we only took the one with the best χ^2/degree of freedom. This was done because most of the multi-track events stem from reconstruction ambiguities, and only a few were real multi-track events.

Monte Carlo Simulation

The simulated data was produced with GEANT, using GHEISHA as the hadronic shower generator. To generate a reasonable number of muons reaching $20\,\lambda$ we had to tune the program for speed. In this so-called *fast Monte Carlo*, only particles with momentum above 3 GeV/c were tracked in the calorimeter; this requirement removed all the time consuming low momentum particles. Only in the last 8 cm of TRACAL did we track all particles. This was in order to get approximately the correct distribution of tracks in the first muon station. Since the momentum threshold for muons penetrating the first half of the absorber magnet is 3 GeV/c, we did not loose signal events by this modification. The simulated data was then treated in the same way as the real data, except for the activity cut and the MWPC cut, which were not applied. Table 3.6 gives an overview of the available Monte Carlo data.

To study the geometrical acceptance loss, the same simulation program which was described above (see Section 3.2.2) was run. The absorber magnet covers an area 0.8 m above and below the beam line. Tracks that are bent outside this area were rejected at Station 2 and Station 3. At Station 1, all tracks outside the calorimeter boundaries were rejected. The acceptance loss at Station 1 was found to be $3.2 \pm 1.1\%$ for M1 off. However, this signal loss affects only low momentum particles (below 15 GeV/c) and changes the distributions shown here only slightly. We did not correct for this

effect.

momentum	particle type							
[GeV/c]	π^-		π^+		K^+		proton	
	statistics, M1 field 0 T							
30	250 k	93						
100	60 k	61	60 k	74				
300	20 k	81						
	statistics, M1 field 3 T							
30	250 k	64						
100	60 k	58	60 k	83	60 k	96	60 k	30
300	20 k	48						

Table 3.6: Event statistics for the simulation of punchthrough muons. The first column of each particle type gives the number of generated events (in thousands). The second column gives the number of events with at least one track passing all cuts.

3.3.2 Results

Momentum Distribution of Punchthrough Muons

The momentum spectra of punchthrough muons for various beam momenta and particle types are presented in this section. We corrected these spectra for the inefficiencies of the detector and the momentum fit and for the signal losses due to the applied cuts. These include:

- Trigger efficiency of the 10 λ trigger: 99 % $\pm$ 0.3 %.
- Reconstruction efficiency in muon chambers (position and direction dependent); 79–91 %, typical error: 2 %.
- Matching and fit efficiency, momentum dependent: 50–90 %, typical error: 2 %.

- MWPC efficiency (i.e. percentage of undisturbed events): $91.8\,\% \pm 1.2\,\%$.

Figure 3.25 shows the combination of all these efficiencies (except the activity cut) as a function of the muon momentum. The errors were treated as systematic errors; their sum is also shown in Figure 3.25. These efficiencies were calculated using real muon data, with momenta from 10 to $300\,\mathrm{GeV}/c$, simulated muons and data generated using the fast Monte Carlo.

In Figure 3.26 the momentum distributions of punchthrough muons originating from showers produced by positive and negative pions, positive kaons and protons, are presented. The probability, integrated over punchthrough muon momentum, is consistent with the measured total punchthrough probability presented in Section 3.2.3. Negative and positive momentum, corresponds to negatively and positively charged punchthrough muons, respectively. The hole in the center of the distribution is due to the momentum acceptance of the RD5 spectrometer; a muon's momentum must be at least $3\,\mathrm{GeV}/c$ before it will reach the second muon station and thus become a candidate for reconstruction. The charge asymmetry observed in each spectrum may be explained by the existence of leading particles in the hadronic shower which will more frequently carry the charge of the incident hadron. These leading particles arise from fragmentation of the incident hadron. Subsequent decay of these leading particles will give punchthrough muons with the same sign as the incident hadron, carrying a large fraction of the incident hadron's momentum.

Figure 3.27 shows the momentum distributions of punchthrough muons originating from π^- showers. The incident pion momentum was 20, 30, 100 and $300\,\mathrm{GeV}/c$. We compare the results using data taken with M1 off and M1 at 3 T. For the data taken with M1 at 3 T one observes a reduction in the number of low energy muons reaching Station 2. It was found, as a result of running the detector acceptance simulation, that

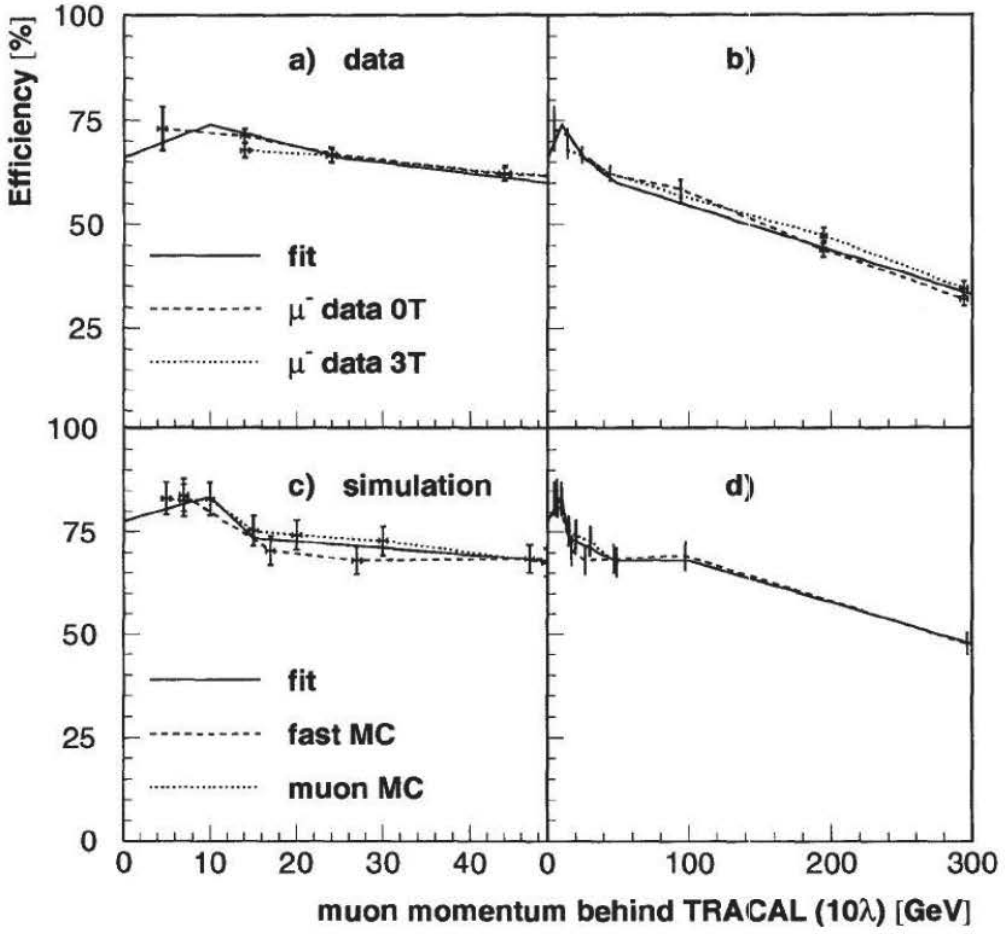

Figure 3.25: The total efficiency for the momentum fit as a function of the muon momentum. Fig. a) and b) show the efficiency for real data, Fig. c) and d) show the efficiency for simulated data. Fig. a) and c) show an enlarged view of the low momenta, while Fig. b) and d) cover the whole momentum range. The solid curves were used for the correction of the momentum spectra.

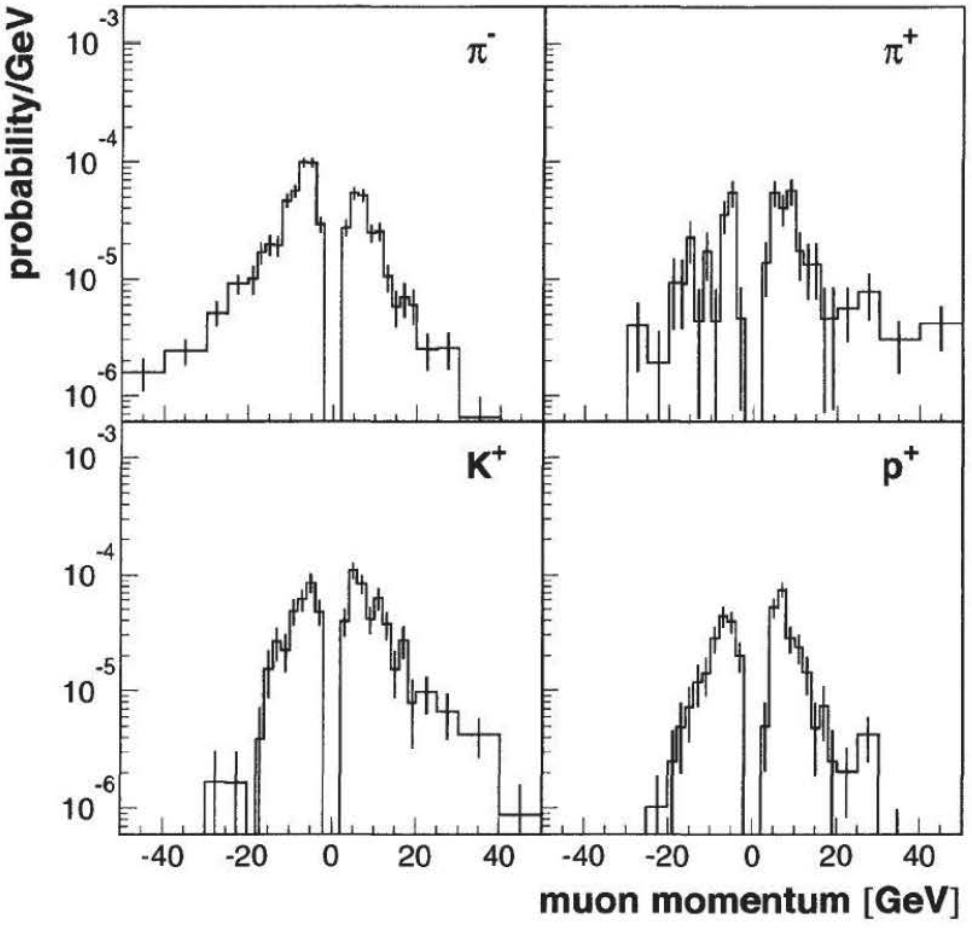

Figure 3.26: The momentum distributions of punchthrough muons originating from positive and negative pions, positive kaons and protons. All data shown here were taken with 100 GeV/c beam momentum and with the M1 magnet at 3 T.

the observed reduction can be wholly explained by losses due to detector acceptance.

In Figure 3.28 the measured momentum distributions are compared with the results of the Monte Carlo simulation. The data was taken with M1 off. The simulation statistics are very low, however, the measurements and simulation agree within errors.

Angular distribution of punchthrough muons

In Figures 3.29 and 3.30 we show the projected angle of the tracks, in the $x-y$ plane of the RD5 coordinate system, for three different beam momenta. The first figure shows the data taken with magnet M1 off and the second with the M1 field at 3 T. The angle and momentum is given for the reference plane at 10λ. The distributions are given for three intervals of the punchthrough muon momentum. The angle in the transverse plane was also measured. It is independent of the field, as expected, and is not shown here. The data has been corrected as described above. The errors shown include the systematic errors from these corrections.

The shape and the normalization of the simulated distributions agree with the data within the errors. For better readability the simulation is not included in the plots; because of low statistics, the simulated data cannot be shown with this fine binning.

In Figure 3.30 the influence of the magnetic field, which acts to separate positive and negative muons, is clearly seen. The asymmetry between negative and positive secondaries (negative particles also have negative bending angle) is also visible.

3.4 Conclusion

We have measured the total punchthrough probability of hadronic showers produced by positive and negative pions, positive kaons and protons with momenta from 10

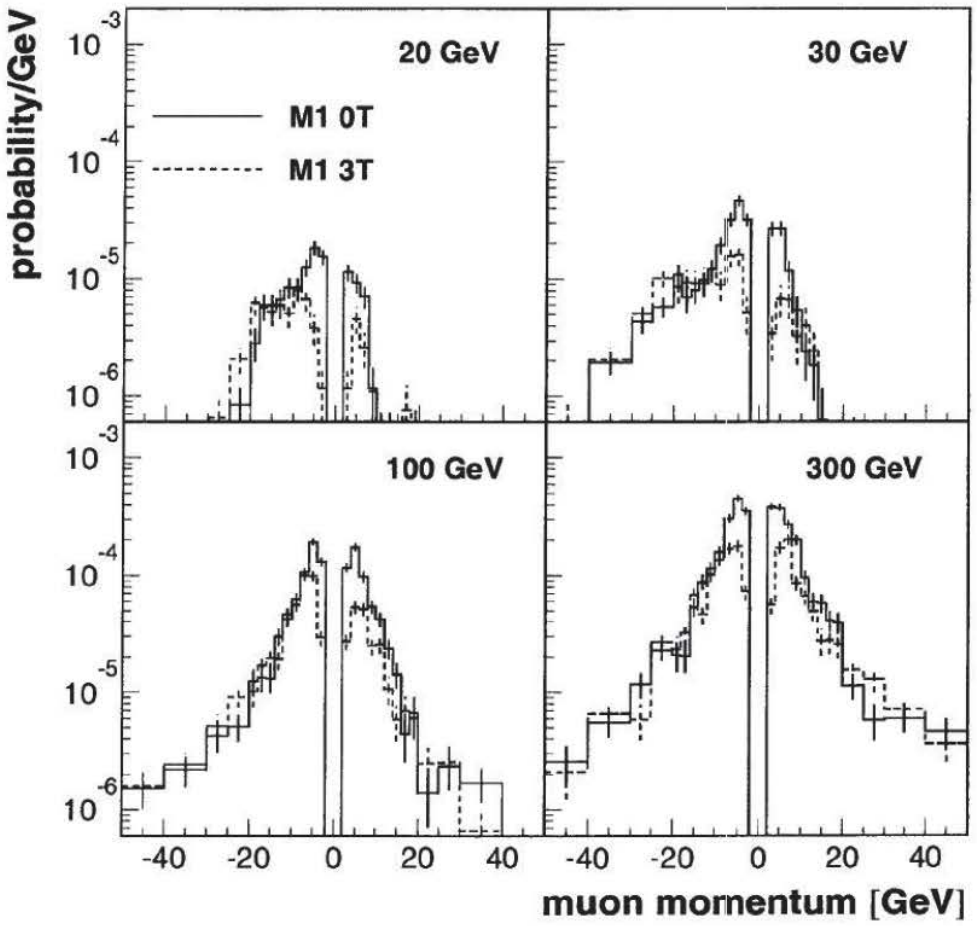

Figure 3.27: Momentum of punchthrough muons from π^- beams with four different energies. Data with the M1 magnet off (solid line) and at full field (dashed line) are shown. The μ^- are plotted with negative momentum. For low beam energies the asymmetry between μ^- and μ^+ is clearly visible.

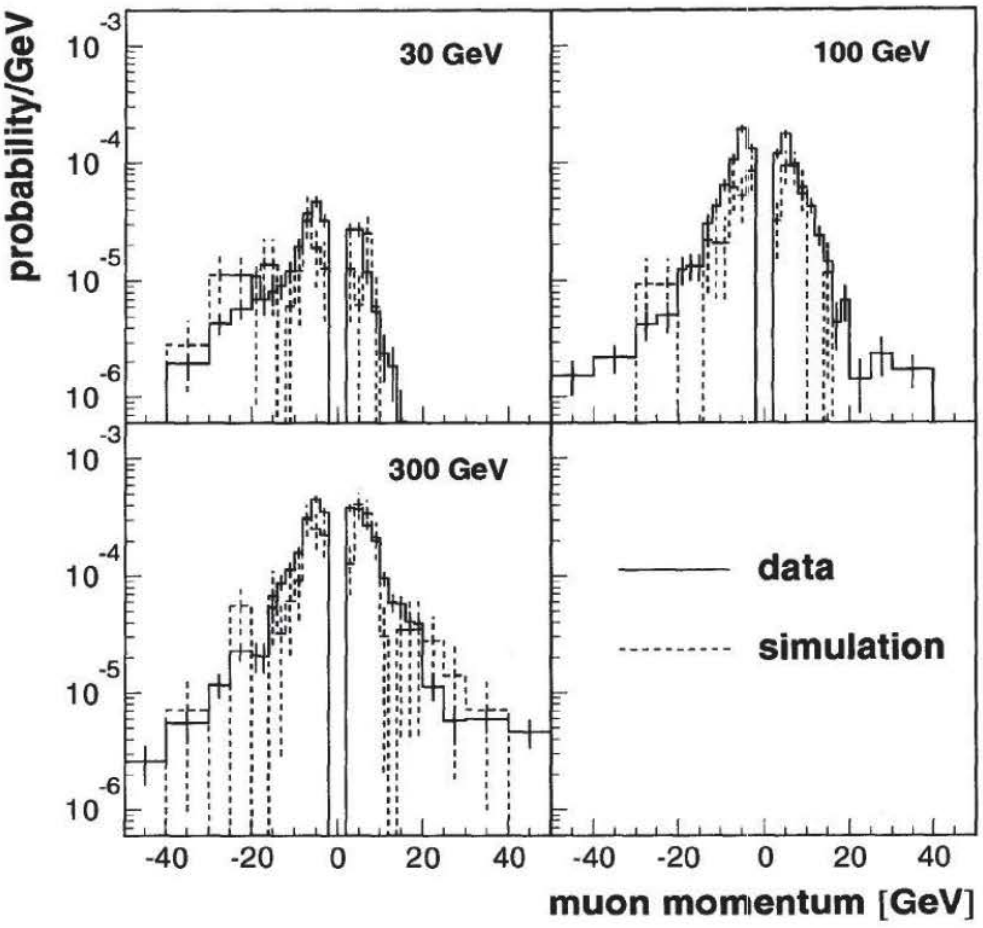

Figure 3.28: The momentum distributions of punchthrough muons originating form π^- data are compared with the GEANT simulation. The data was taken with M1 off. The simulation statistics are very low. The measurement agrees with the simulation within the errors.

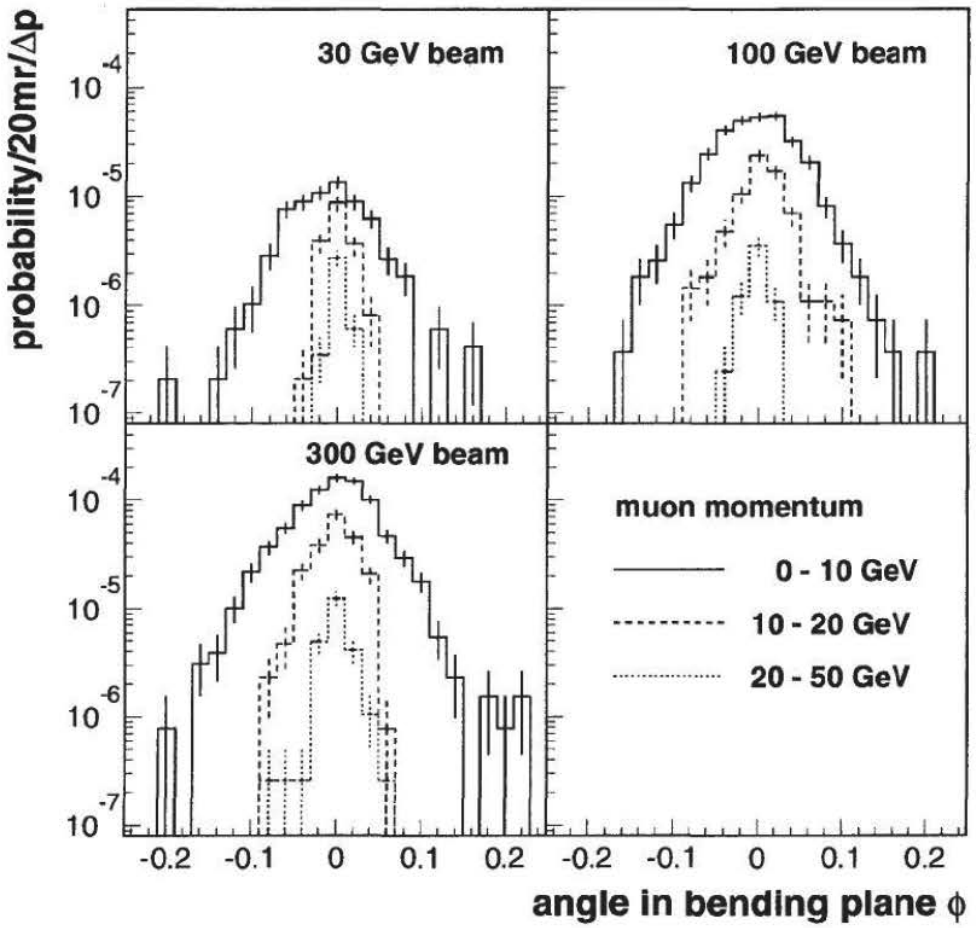

Figure 3.29: Angular distribution of punchthrough muons for three different beam momenta with the M1 field at 0 T. The angle shown here is the projection in the $x-y$ plane of the RD5 coordinate system. The distributions are shown for three intervals of the punchthrough muon momentum.

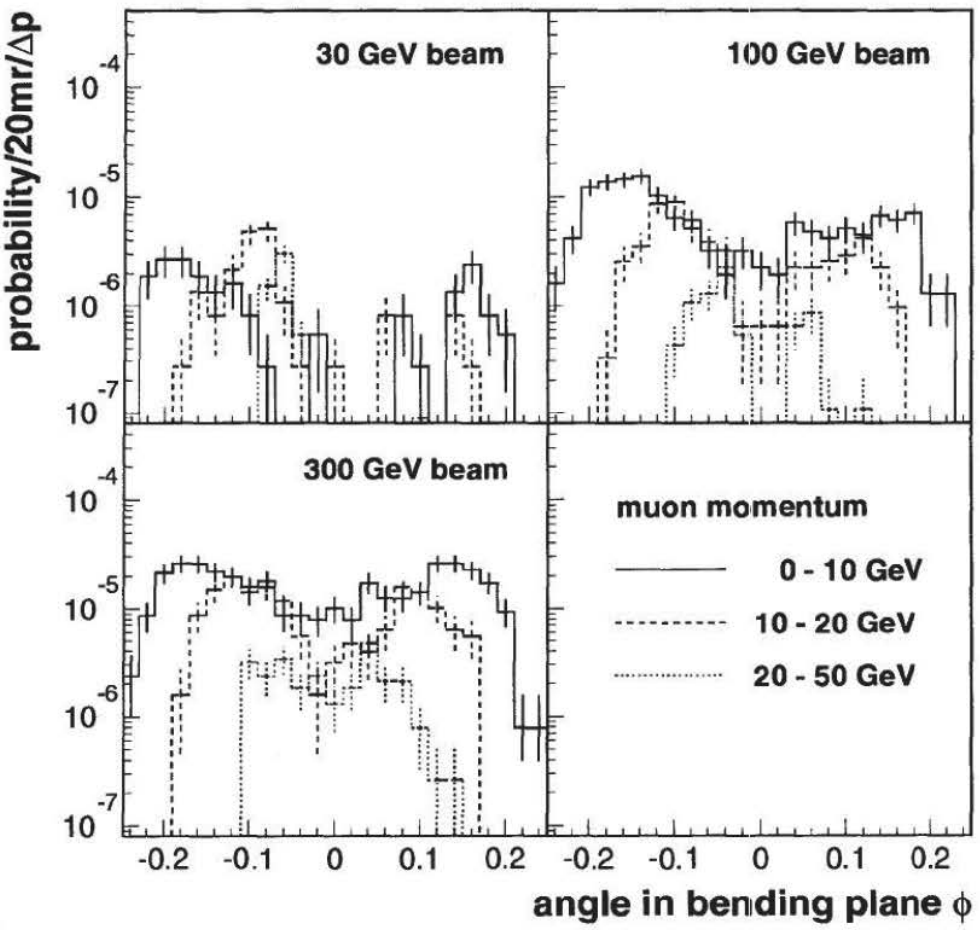

Figure 3.30: Angular distribution of secondary muons for three different beam momenta with the M1 field at 3 T. The angle shown here is the projection in the $x - y$ plane of the RD5 coordinate system. The distributions are shown for three intervals of the muon momentum.

to 300 GeV/c. The measurements reached to a depth of about 31λ, farther than measured by previous experiments.

The momentum and angular spectrum of punchthrough muons which penetrated to a depth of 20 $\lambda$was also measured. The momentum was given for a reference plane at 10 λ. The incident beam particles were positive and negative pions, positive kaons and protons with momenta from 20 to 300 GeV/c. The spectra were corrected for efficiencies due to event selection and muon reconstruction.

The most significant error in these measurements is the uncertainty in the subtraction of the muon contamination in the pion beam. The punchthrough probability at muon station 2 (3.49 m iron eq.) and station 3 (5.29 m iron eq.) are most sensitive to this background. An appropriate systematic error has been added reflecting the uncertainty in the background subtraction.

The influence of a 3 T and 1.5 T magnetic field on hadronic punchthrough was experimentally investigated for the first time. As expected, the reduction in punchthrough due to the magnetic field is largest for lower momentum data. For the 10 GeV/c π^- data, the reduction in the punchthrough probability at 1.43 m iron eq. was almost a factor 3. The reduction in the punchthrough probability within TRACAL may be explained, in part, by low energy shower particles curling back inside of TRACAL and by losses due to detector acceptance. The reductions in the punchthrough probability for absorber depths greater than 10 λ, i.e. muon stations 2 and 3, can be wholly explained by losses due to the detector acceptance.

All the measurements were compared with the results of a simulation of the RD5 detector using GEANT 3.21 and two different hadronic shower generators: GHEISHA and FLUKA. The measured quantities were adequately reproduced by the simulation. For the simulation of the punchthrough probability of 10 and 30 GeV/c negative pions,

the results using FLUKA better match the real data. The general agreement between the simulation and all aspects of the punchthrough study in RD5, give us confidence that this simulation can be used to make accurate predictions when applied to the design of LHC detectors.

Chapter 4

A Study of Charged Particle Rates in the CMS Muon System

In order to realize the optimum performance of the CMS muon system, detailed studies of the different types of backgrounds affecting the system are being performed. The types of background sources being studied are: 1) hadronic punchthrough and decay muons, 2) cosmic ray muons, 3) uncorrelated neutrons and photons and 4) muon-induced electromagnetic showers and delta rays. In this study we concentrate solely on charged particle backgrounds coming from hadron punchthrough and decay muons.

As previously described in Chapter 2, charged particles reaching the CMS muon chambers can be divided into several components: 1) *prompt muons*, coming mainly from heavy quark decays near the interaction vertex, 2) *decay muons*, coming from π and K mesons which decay within the tracking volume and 3) hadronic punchthrough, which consists of muons from π and K decays in the hadronic shower and other charged particles composing the tail of the hadronic shower. In this text when we speak of *punchthrough particles*, we mean punchthrough muons and all other particles

composing the tail of the hadronic shower. Likewise, when we refer to *punchthrough muons*, we refer only to the muon component.

4.1 Particle Rates at the Vertex

It has been found [52] that minimum bias events can be characterized in terms of the quantities $\langle n_{ch} \rangle$ (the mean charged multiplicity), $\langle p_T \rangle$ (the average transverse momentum) and $\sum E_T$ (the scalar transverse energy). These quantities increase with center of mass energy and show an approximate linear log s dependance, where $\sqrt{s}$ is the center of mass energy of the proton-proton collision. The parameters of the Monte Carlo programs PYTHIA and ISAJET have been tuned in order to correctly reproduce these quantities, which were measured by UA1 and CDF in the center of mass energy interval between $\sqrt{s} = 0.2\,\text{TeV}$ up to $\sqrt{s} = 1.8\,\text{TeV}$. The predictions of the two Monte Carlo programs were then extrapolated to the center of mass energy of the LHC, $\sqrt{s} = 16\,\text{TeV}$ [53]. (The planned center of mass energy for collisions at the LHC was reduced to $\sqrt{s} = 14\,\text{TeV}$ since the completion of this work. This change is not expected to significantly affect the results presented in this chapter. Other uncertainties, for example uncertainties in the simulation of minimum bias events, are expected to be more important. In any case, one would expect that a reduction in the center of mass energy of p-p collisions would lead to a reduction in the number of charged particles reaching the CMS muon system.)

An estimate of the rate of charged particles emerging from the collision vertex at the LHC was obtained by running the tuned Monte Carlo program PYTHIA [54]. The procedure followed is due to M. Konecki et al. [55]. The PYTHIA parameters used in the simulation of minimum bias events are listed below.

```
MSEL = 1

MSTP (82) = 4

MSTP ( 2) = 2

MSTP (33) = 3

PARP (85) = 0.81

PARP (86) = 0.9

PARP (82) = 1.6
```

These parameters result in a minimum bias cross section of about 81 mb. In total, 1.2×10^6 events were simulated. All hadrons and muons within $\eta = \pm 2.5$ were accepted. A luminosity of $10^{34}\mathrm{cm}^{-2}\mathrm{s}^{-1}$ has been used throughout. The p_T distribution of hadrons is shown in Figure 4.1 a). The solid points were obtained with no kinematic cut on the transverse momentum of produced jets. It can be seen that statistics above $20\,\mathrm{GeV}/c$ are not sufficient to allow accurate parametrization. In order to reduce fluctuations in the tail, an additional 4×10^5 "hard" events with ${p_T}^{jet} > 20\,\mathrm{GeV}/c$ have been simulated. The distribution parameterized consisted of the minimum bias spectrum below $20\,\mathrm{GeV}/c$ and the hard spectrum above. The fractions of the different types of hadrons produced by PYTHIA are presented in Table 4.1.

The distribution has been fitted with the following formula:

$$\frac{dN}{d\eta dp_T} = \begin{cases} ae^{\frac{-(x-\mu)^2}{2\sigma^2}} & 0.1 < p_T < 1.0 \\ (1 + a_3x + a_4x^2)e^{(a_1+a_2x)} & 1.0 < p_T < 100. \end{cases}$$

where $x = log_{10}p_T$ [GeV/c] and,

$$a = 0.780 \times 10^{10},\ \mu = -0.664,\ \sigma = 0.329$$

$$a_1 = 20.75,\ a_2 = -12,\ a_3 = 3.3,\ a_4 = 34.1$$

Table 4.1: Percentage of different particles produced by PYTHIA for proton-proton collisions at the center of mass energy 16 TeV.

Particle type	Fraction generated
$\pi^{\pm}$	51.7%
$K^0_L, K^0_S, K^{\pm}$	28.1%
$p, \overline{p}, n, \overline{n}$	12.3%
$\Lambda, \overline{\Lambda}$	3.4%
$\Sigma^{\pm}, \overline{\Sigma}^{\pm}$	3.2%
$\Xi^-, \Xi^0, \overline{\Xi}^0$	1.3%

A similar procedure was followed to parameterize the prompt muon spectrum. In this case it was necessary to simulate an additional data set with $p_T{}^{jet} > 40\,\mathrm{GeV}/c$. The p_T distribution of prompt muons is shown in Figure 4.2 a). In this case the p_T spectrum is a lognormal distribution:

$$\frac{dN}{d\eta dp_T} = ae^{\frac{-(x-\mu)^2}{2\sigma^2}}$$

where $x = log_{10}p_T$ [GeV/c] and,

$$a = 0.134 \times 10^7,\ \mu = -0.593,\ \sigma = 0.371 \quad \text{for} \quad 0.1 < p_T < 1.0$$

$$a = 0.230 \times 10^8,\ \mu = -1.570,\ \sigma = 0.565 \quad \text{for} \quad 1.0 < p_T < 100.$$

The result of the parameterization of minimum bias hadrons and prompt muons are presented in Figures 4.1 b) and 4.2 b), respectively. The parameterization is superimposed on the data points which were used for the fit.

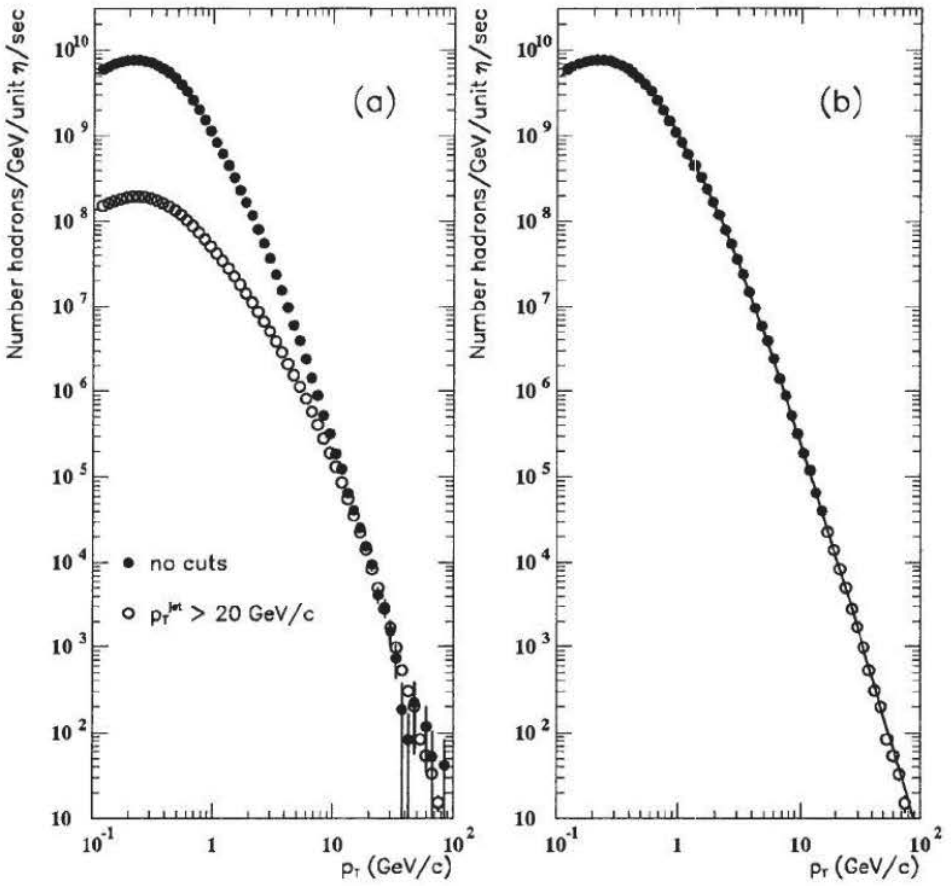

Figure 4.1: p_T distribution of hadrons: a) The solid circles are data with no kinematic cut on the transverse momentum of jets, the open circles are data with $p_T^{jet} > 20\text{GeV}/c$. b) The parameterization superimposed on the data points used for the fit.

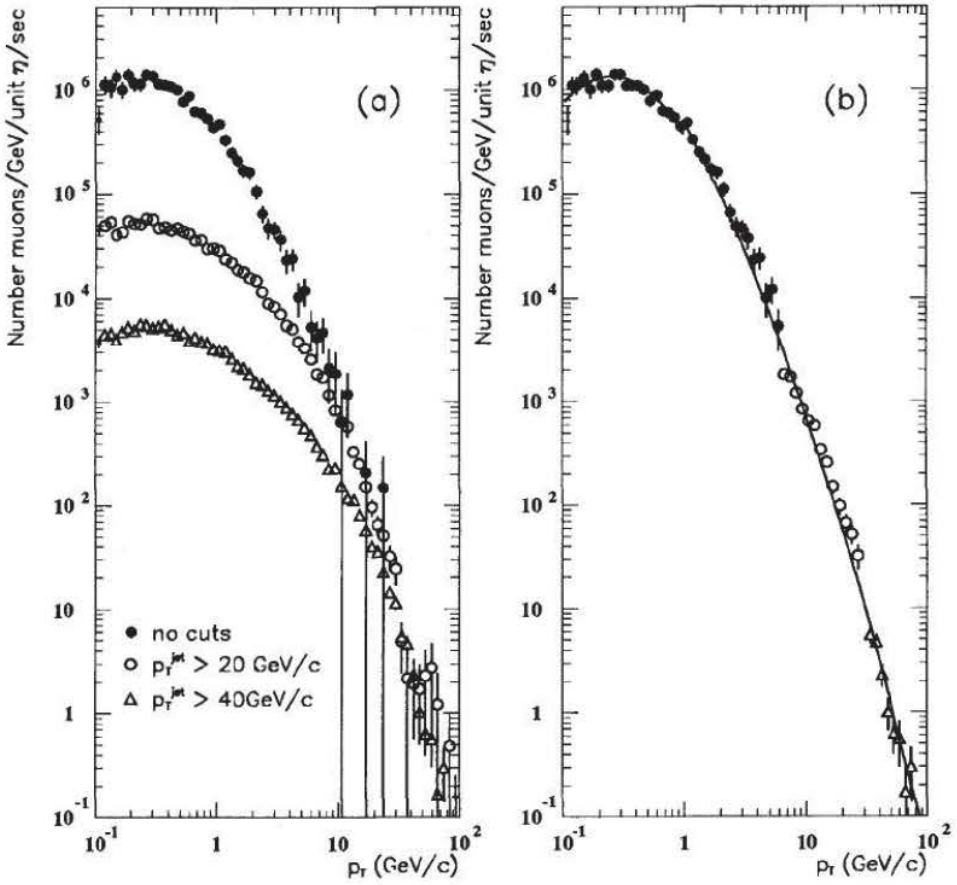

Figure 4.2: p_T distribution of prompt muons: a) The solid circles are data with no kinematic cut on the transverse momentum of jets, open circles are data with $p_T^{jet} > 20\text{GeV}/c$ and the triangles are data with $p_T^{jet} > 40\text{GeV}/c$. b) The parameterization superimposed on the data points used for the fit.

4.2 CMS Simulation

The CMS simulation program (CMSIM) [56], version 004[1], running on CERN's Central Simulation Facility (CSF), is a GEANT-based general purpose description of the CMS detector. A CMSIM user may select geometry options most appropriate to their study through the use of GEANT data cards. The rate due to hadronic punchthrough and decay muons does not depend on the detailed structure of the central tracker, electromagnetic calorimeter (EC) or hadronic calorimeter (HC). Therefore, a simplified structure of these detector elements consisting of average materials was chosen.

In the case of decay muons, the length of the primary particle's decay path, and thus the decay probability, is determined by the size of the tracking volume. The amount of material in the central tracker reaches a maximum of about 30% of one radiation length at $\eta = 1.5$ [57], therefore, we could neglect the absorption due to this small amount of material and choose an empty tracking volume.

The punchthrough probability of hadrons depends on the initial momentum of the primary hadron, the total absorber thickness and the location of air gaps between dense absorbers which provide space for pions to decay. The EC has a maximum thickness of 60 cm at $\eta = 0$ and tapers down to 25 cm thickness at $\eta = 1.5$, however, due to the overall projective geometry of the CMS detector the EC presents a constant 1 λ absorption path to particles coming from the interaction region. In the barrel, the amount of material in front of MS1 is about 10.1λ and is the sum of the material in the EC + HC (7λ) the magnet coil (1.1λ) and the tail catcher (2λ). In the end-cap region, the amount of material in front of MF1 is the sum of the EC + HC and is about 12 λ. A schematic of the CMS detector is presented in Figure 1.3. The

[1]This geometry version was current at the time of the CMS Letter of Intent [14]

Table 4.2: Flags used to select CMS geometry version used for the rate study.

Detector	Flag	Description
CMS (general)	ICVERS = 9	CMS version 004
Tracker	ITVERS = 0	Tracking volume filled with air
EC	IEVERS = -1	Average material of BGO
HC	IHVERS = -1	Average material of lead/plastic scintillator
Muon	IMVERS = 901	Simple box filled with gas
VC	IFVERS = 0	No forward calorimeter

reader is referred to Section 1.4 of this text for a more detailed description of CMS. A summary of the geometry options chosen for the rate study is presented in Table 4.2.

The simulation also accounted for the full 4 T solenoidal magnetic field planned for CMS. The magnetic field map version was 07b. It should also be noted that this is a simulation of ideal muon chambers. Any chamber inefficiencies or internal structures of the chambers themselves were not considered.

Single hadrons and muons were generated at the interaction vertex distributed exponentially with respect to p_T. The minimum transverse momentum generated was 0.2 GeV/c and the average was 10 GeV/c. The generated hadrons and muons were equally distributed with respect to η. The type of hadron generated was determined according to the percentages in Table 4.1. The GEANT flags used to control physics processes were all set to 1. The hadronic shower generator GHEISHA, which is integrated as part of GEANT, was used. All particles were tracked down to an energy cut-off of 10 MeV. The effect of a lower energy cut-off is presented below in Section 4.3.5.

In order to increase the statistics for high p_T hadrons, the generated spectrum was "harder" than the true spectrum as described in Section 4.1. In order to compensate for this, a set of weights, which consisted of the ratio of the "generated" hadron

or muon spectrum to the "true" hadron or muon spectrum, was calculated. The hit position and particle type of all charged particles entering a muon chamber was recorded, in addition, if the particle type was "muon", the particle's 3-momentum was also recorded. All hits were weighted according to the set of weights just described. All hadrons which decayed, producing muons in the tracking volume, were flagged, thus allowing one to distinguish decay muons from punchthrough muons.

4.3 Simulation Results

4.3.1 Comparison with Experimental Results of RD5

In this section we compare the results of the CMS simulation with the corresponding measurements in RD5. In order to more easily make this comparison, mono-energetic pions were generated in the barrel at $\eta = 0.1$. Approximately 8.2×10^4 pions were simulated at three momentum values: 30, 50 and 100 GeV/c.

Figure 4.3 shows the comparison between the punchthrough probability for pions at MS1, MS2, MS3 and MS4, with the experimental results of RD5. The simulation is being compared to the RD5 data with the field of M1 at 0 T. The agreement between simulation and data is adequate. In each case, however, the total punchthrough probability in MS1 is lower than the RD5 data. This may be because the 4 T field in the CMS simulation is more efficiently deflecting back low energy punchthrough particles. One should note that $\int \vec{B} \times d\vec{l}$ evaluated over the central region of CMS is 12 T·m. This strong field is effective in suppressing low energy punchthrough particles that would normally reach the first muon station.

In Figure 4.4 we compare the muon momentum measured at RD5 with the simulated punchthrough muons from mono-energetic pions of 30, 50 and 100 GeV. Here

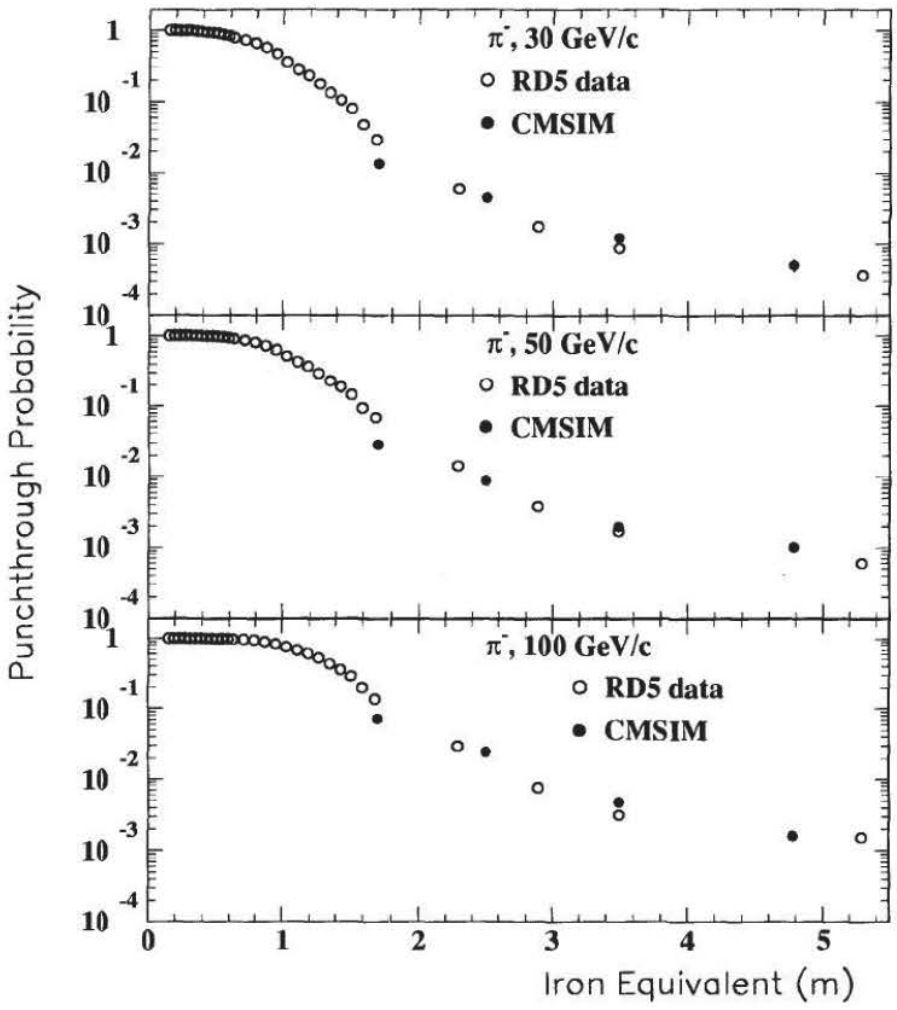

Figure 4.3: Comparison between RD5 data with M1 at 0 T and the CMS simulation with its 4 T solenoidal field. The solid circles indicate the punchthrough probability at MS1, MS2, MS3 and MS4.

we use the RD5 data with M1 off. We see a good agreement between data and simulation, except for the 50 GeV data. This disagreement is still under investigation. The difference between the two curves near the beam momentum for the 30 GeV plot is due to the resolution of the RD5 detector, which is 12 % for this momentum.

4.3.2 Muon Penetration Efficiency

When beginning this simulation, we first wanted to determine what is the minimum transverse momentum that a particle must have before it can penetrate to the muon stations. Because of limited CPU time it is not practical to simulate particles with arbitrary small momentum which would never have a chance to create a signal in the muon stations.

To determine what is a reasonable p_T threshold for particle generation, muons were generated at the interaction vertex and tracked through the CMS detector accounting for energy loss and multiple scattering. Figure 4.5 shows the probability that a muon starting off with a given transverse momentum in the barrel and in the end-cap region will reach a given muon station.

In the barrel, the p_T threshold for particles to reach MS1 is mainly determined by the bending power of the central magnetic field. Given a 4 Tesla field, a particle with a transverse momentum less than 2.3 GeV/c will have a radius of curvature less than half the distance to MS1. The momentum threshold for a muon to reach MS4 is about 6 GeV/c. In the end-cap region muons with p_T less then 0.5 GeV/c can penetrate to MF1. Low p_T muons are able to penetrate to end-cap muon stations because the bending power of the magnetic field is weaker, and as η increases, a particle with small transverse momentum can have a large longitudinal momentum.

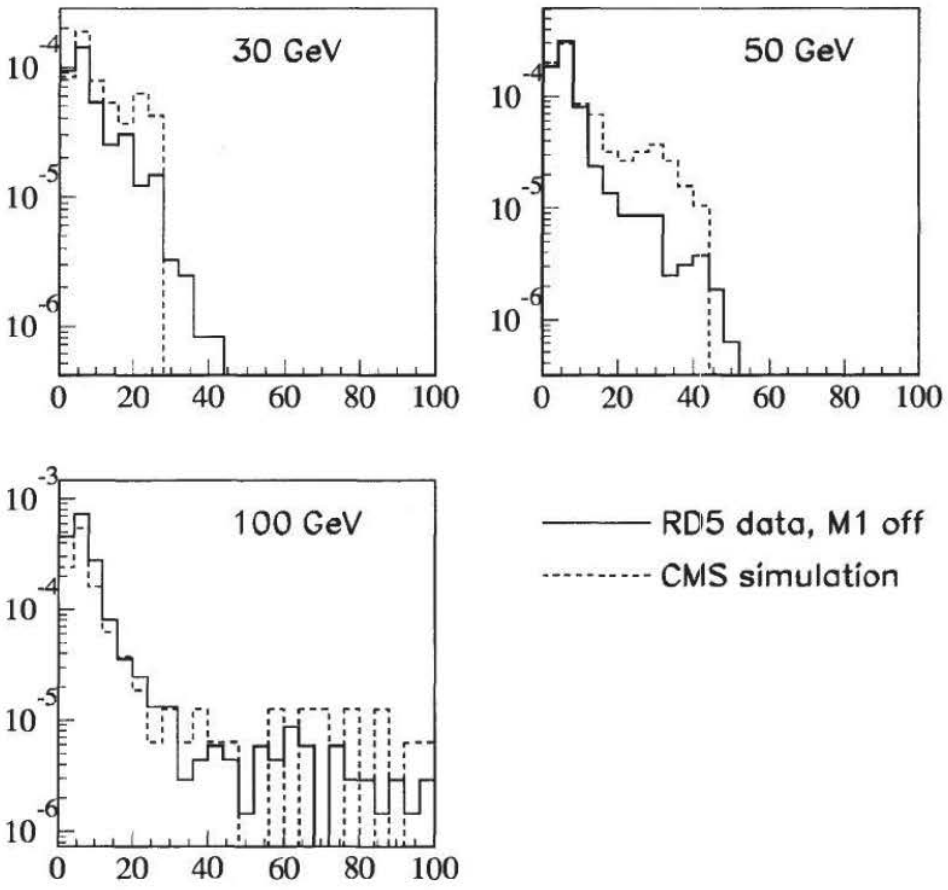

Figure 4.4: The momentum spectrum of punchthrough muons measured at RD5 (solid lines) compared with the CMS simulation (dashed lines). The RD5 data was taken with M1 at 0 T.

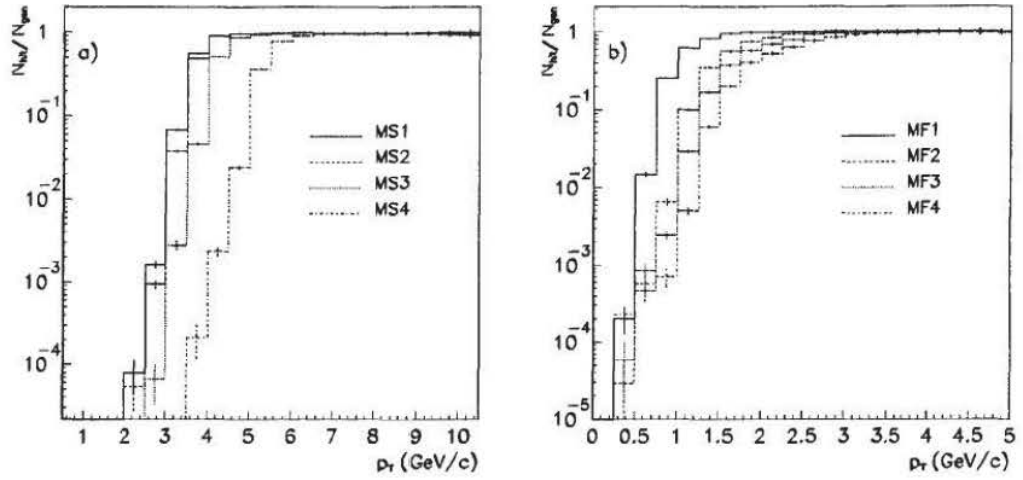

Figure 4.5: Fraction of muons reaching a given muon station in a) barrel ($0. < \eta < 1.5$) and b) end-cap ($1.5 < \eta < 2.5$) regions.

4.3.3 Punchthrough and Decay Probability for Hadrons

The generated hadron data was used to calculate the probability that a hadron will produce at least one hit in a given muon station. This is the combined probability for hadrons which interact in the calorimeter and hadrons which decay in the tracking volume. The type of hadron generated was determined according to the percentages in Table 4.1. The probability for hadrons to produce at least one hit in the barrel muon stations, as a function of p_T, is presented in Figure 4.6, the probability for end-cap muon stations is presented in Figure 4.7. The average charged particle multiplicity per primary hadron in the barrel and end-cap muon stations is presented in Figures 4.8 and 4.9, respectively.

The kinds of particles reaching the CMS muon stations is presented in Figure 4.10. For the particle type ID we use the GEANT convention. The sum of punchthrough particles and decay muons is shown. One sees that a large number of electrons and pions, the tail of the hadronic shower, reaches MS1 and MS2. As expected, only

muons penetrate to MS4.

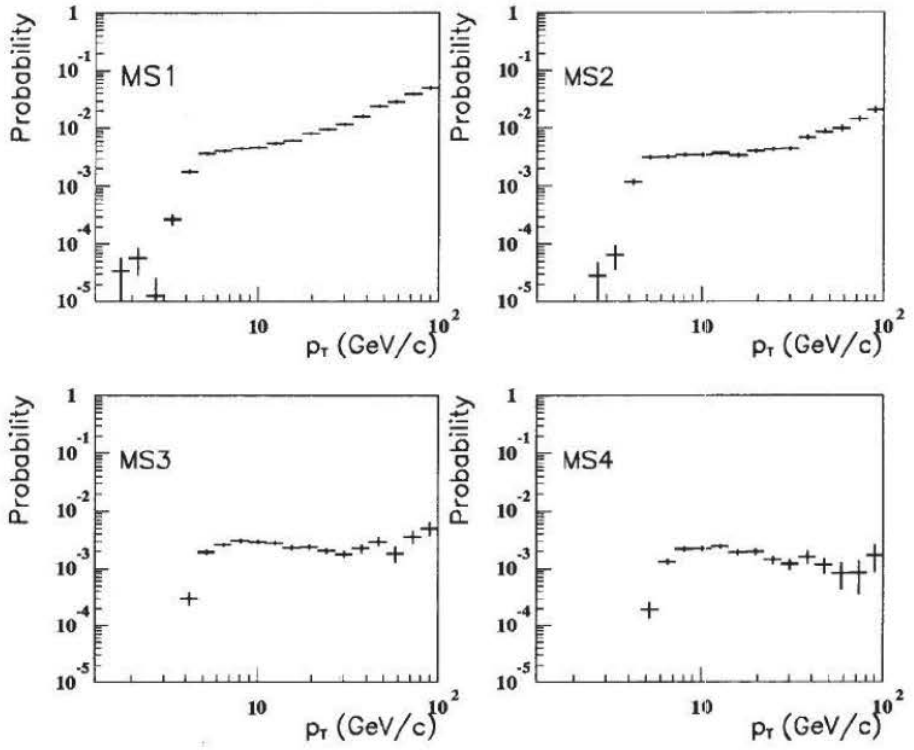

Figure 4.6: Probability that a hadron will produce at least one hit in the barrel muon stations as a function of initial hadron p_T.

4.3.4 Momentum Spectrum of Muons

In Figure 4.11, we present the momentum spectrum of muons at MS1 and MF1 for four different pseudorapidity intervals. The spectra of prompt, punchthrough and

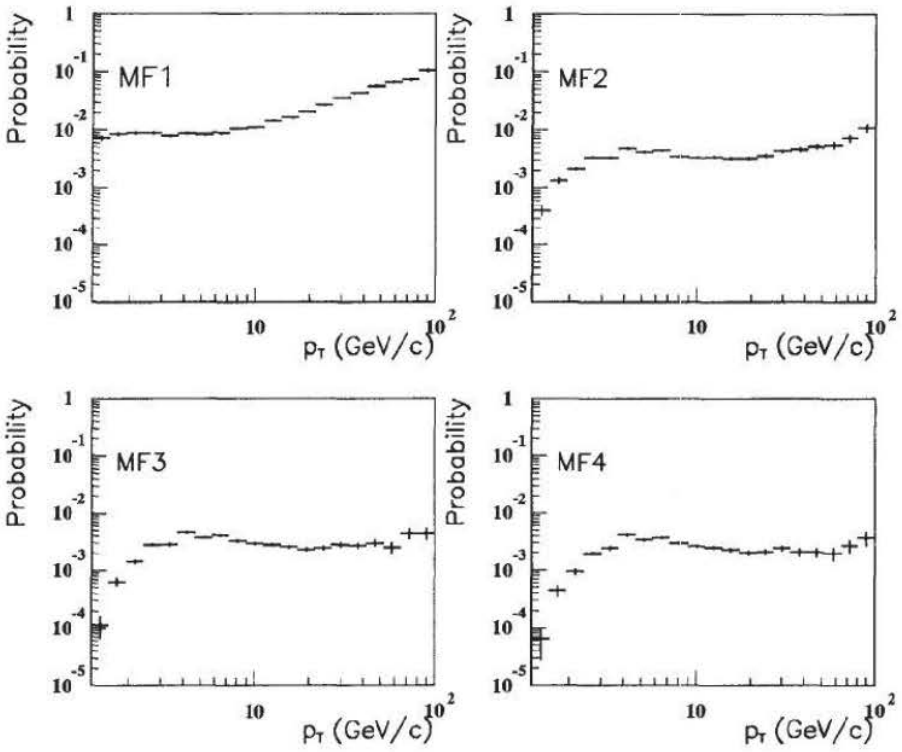

Figure 4.7: Probability that a hadron will produce at least one hit in the end-cap muon stations as a function of initial hadron p_T.

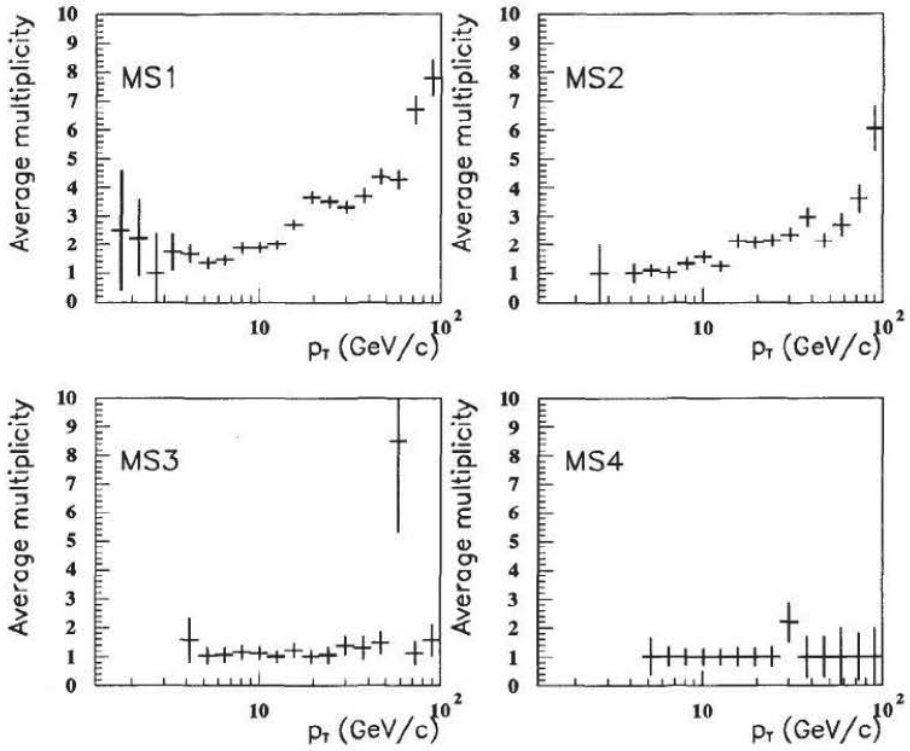

Figure 4.8: Average charged particle multiplicity in barrel muon stations per primary hadron as a function of initial hadron p_T.

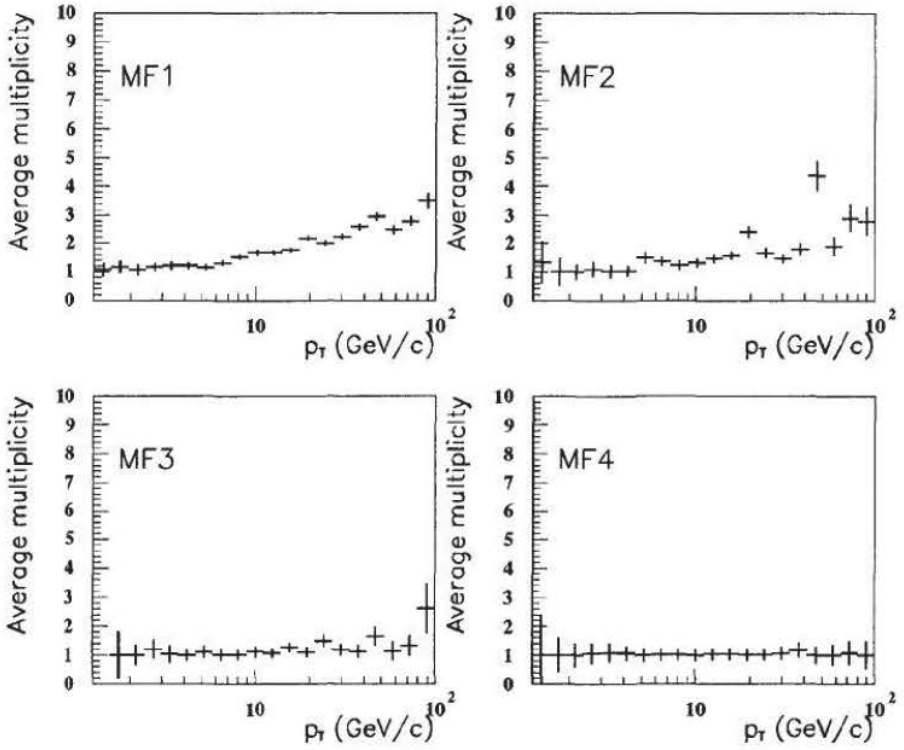

Figure 4.9: Average charged particle multiplicity in end-cap muon stations per primary hadron as a function of initial hadron p_T.

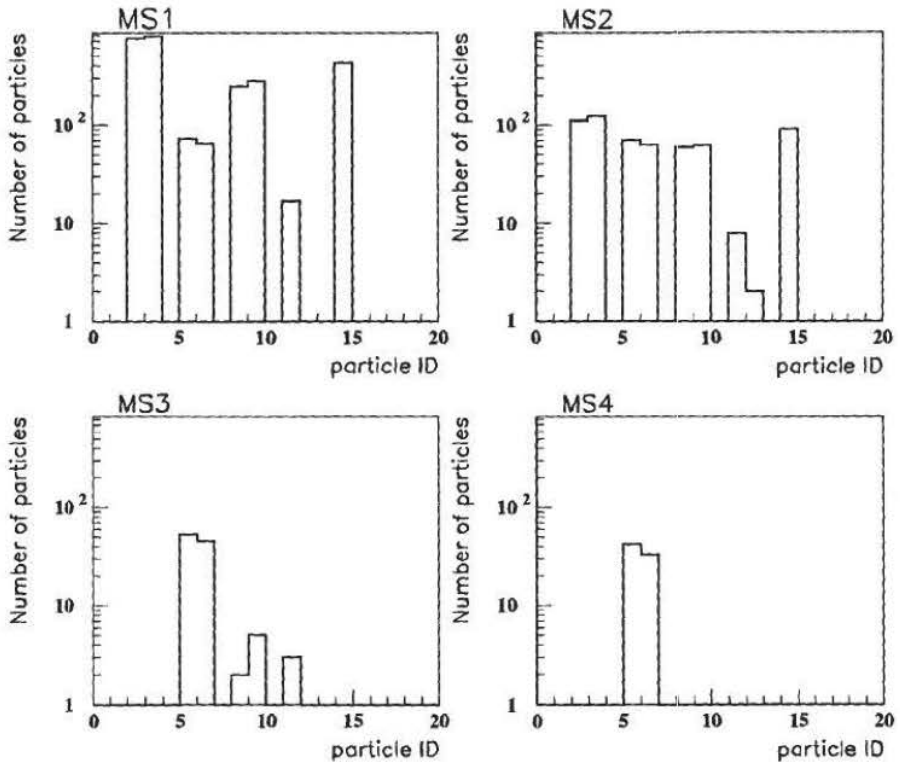

Figure 4.10: The number of particles of each particle type that reach a given muon station. Approximately 8.2×10^4 pions were simulated. The initial pion momentum was 30 GeV/c. For the particle ID we use the GEANT convention: 2 or 3 electrons, 5 or 6 muons, 8 or 9 pions, 11 or 12 kaons and 14 or 15 protons.

decay muons are given separately. The prompt muons have the hardest spectrum and also dominate the total rate in the barrel (see also Section 4.3.6). The punchthrough muons have the softest spectrum, as expected. In the end-cap region the spectra of punchthrough and decay muons become harder and they dominate the total rate for muon momentum less than about 20 GeV/c. The momentum given here is the muon momentum at MS1, after energy loss in the calorimeter.

The kink in the prompt muon spectrum at 90 GeV, for small rapidities (upper left picture in Figure 4.11), is an artifact of the generated spectrum. The particles were generated with a transverse momentum spectrum up to 100 GeV. In the barrel region ($\eta = 0$) the transverse momentum equals the momentum. Furthermore, these muons loose, on average, about 1.4 GeV/c passing through the barrel calorimeter.

4.3.5 Charged Particle Rates

The total charged particle rate (Hz/cm^2) in the barrel and end-cap muon stations is shown in Figure 4.12. The rate is the sum of prompt muons, decay muons and punchthrough particles. One sees that in the barrel region ($\eta < 1.5$), the total rate remains below 0.1 Hz/cm^2 then rises rapidly in the end-cap region to a maximum of about 300 Hz/cm^2 at $\eta = 2.4$. The large decrease in the rate, as one goes from MS1 to MS4, results from particles being absorbed as they pass through successive layers of iron separating the muon stations and largely due to geometrical effects; the particle flux is spread over a larger surface area for muon stations at larger radii.

The charged particle rate (Hz/cm^2) at each muon station, as a function of η, is presented in Figures 4.13 through 4.16. The total rate is decomposed into a rate due to prompt muons, decay muons and punchthrough particles. Each figure is plotted with the same scale so one can more easily compare the relative rates. One sees that

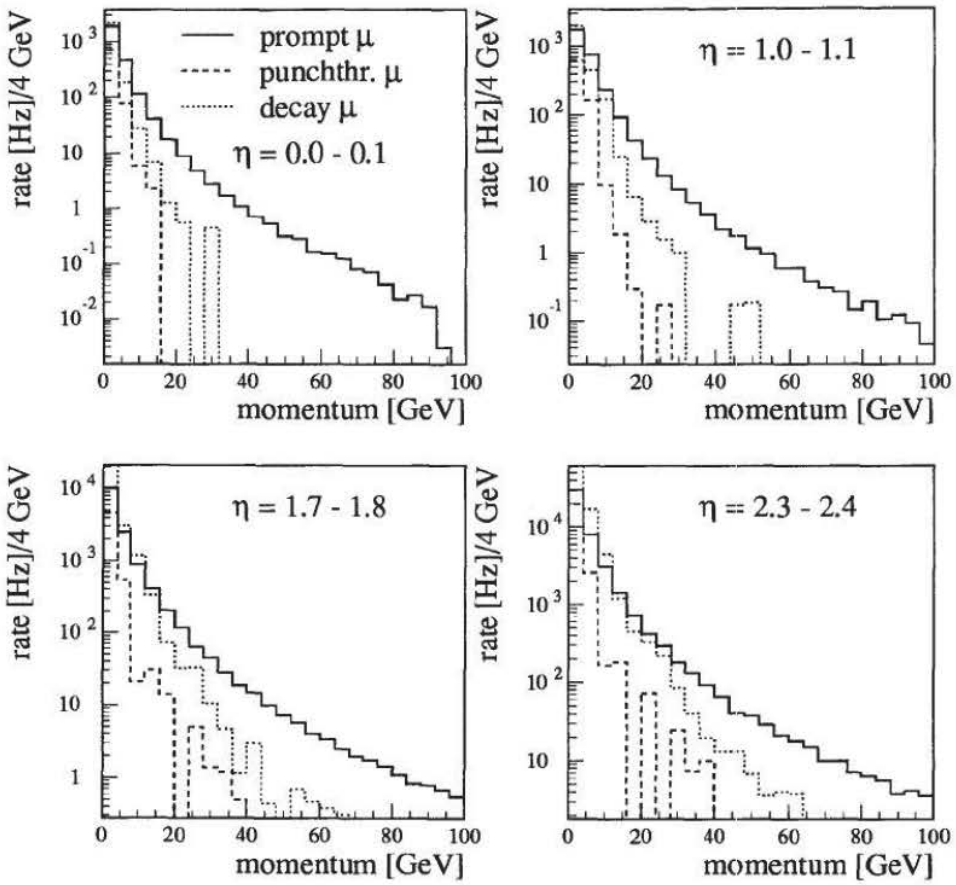

Figure 4.11: Simulated momentum spectra of prompt, punchthrough and decay muons for four pseudorapidity intervals. The kink at 90 GeV in the upper left picture is an artifact of the generated spectrum.

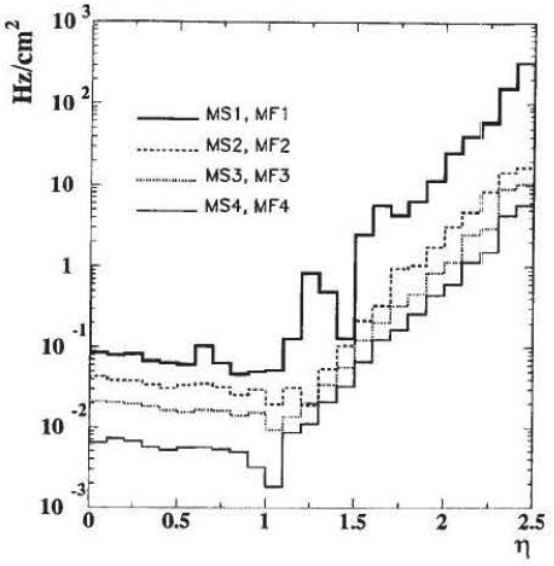

Figure 4.12: Rate (Hz/cm^2) of all charged particles reaching the barrel and end-cap muon stations.

in MS1 ($\eta < 1.5$) the CMS calorimeter has been optimized so that punchthrough, decay and prompt muons contribute equally to the total rate. In the end-cap region ($\eta > 1.5$) decay muons and punchthrough dominate. The increase in the decay rate in the end-cap is due to the longer decay path available for particles traveling in the forward direction. The increase in the punchthrough rate occurs because these particles have a larger longitudinal momentum than particles in the barrel for a given p_T. Furthermore, the magnetic field is much less effective in suppressing punchthrough in the forward direction because the particles are traveling predominantly along the field lines.

In all muon stations, the particle rate due to decay muons is either greater than or comparable to the rate due to prompt muons, however, the trigger rate due to prompt muons always dominates over the rate due to punchthrough and decay (for $p_T^{cut} > 6$ GeV/c) [58]. This is a consequence of the fact that the momentum spectrum

of prompt muons is harder than the spectrum due to punchthrough and decay muons (see Figure 4.11).

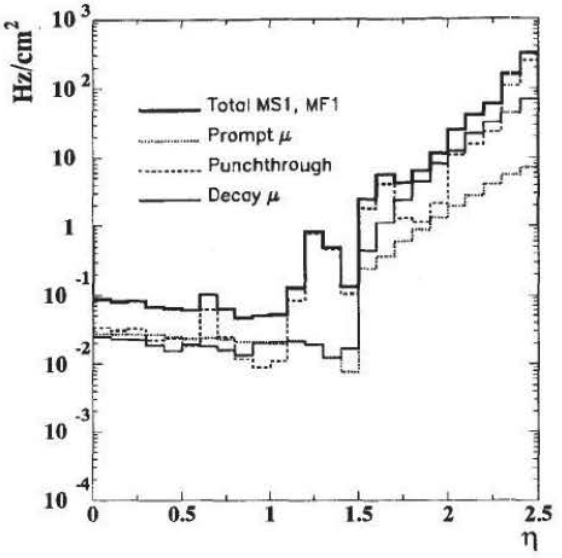

Figure 4.13: Charged particle rate (Hz/cm^2) in MS1 and MF1. The rate due to prompt muons, decay muons and punchthrough particles is indicated.

In order to investigate the sensitivity of the charged particle rate to the GEANT energy cut-off, an additional simulation was run where the energy cut-off was set to 1 MeV. A comparison between the rate calculated with 10 MeV and 1 MeV cut-offs is presented in Figure 4.17. One can see that, within statistical fluctuation, both simulations give almost the same result. Therefore, the 10 MeV energy cut-off was used for the entire simulation. The use of the higher energy cut-off reduced the required CPU time by about a factor 2.

One outstanding feature in Figure 4.13 is the large increase in the rate due to punchthrough between $\eta = 1.1$ and $\eta = 1.4$. It was found that the increased rate is due to additional punchthrough hadrons and electrons. This increase is in the region

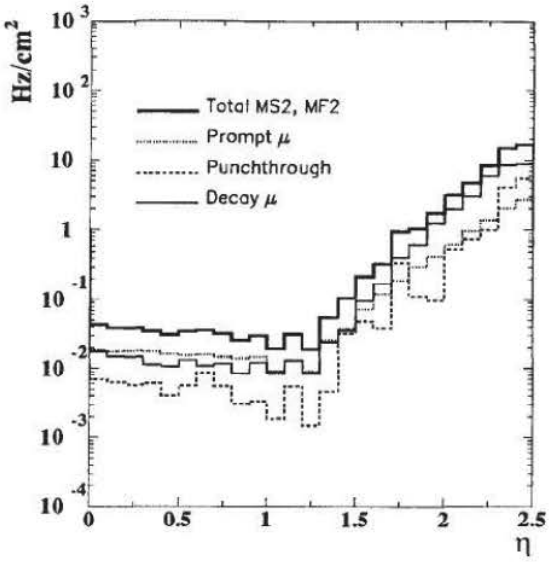

Figure 4.14: Charged particle rate (Hz/cm^2) in MS2 and MF2. The rate due to prompt muons, decay muons and punchthrough particles is indicated.

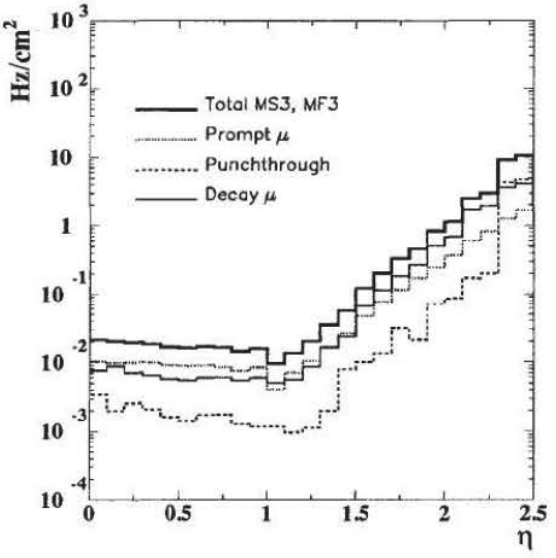

Figure 4.15: Charged particle rate (Hz/cm^2) in MS3 and MF3. The rate due to prompt muons, decay muons and punchthrough particles is indicated.

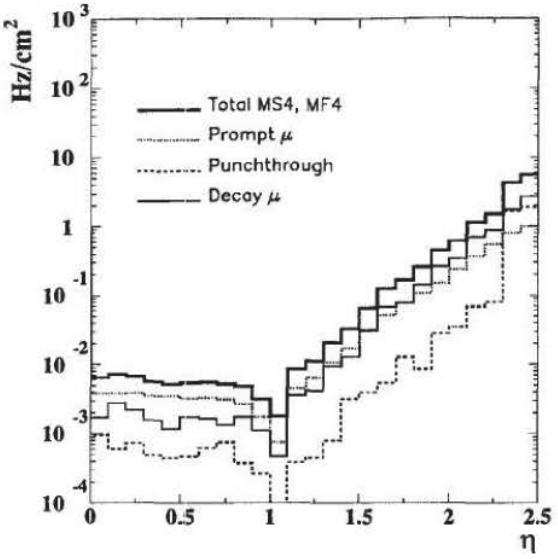

Figure 4.16: Charged particle rate (Hz/cm^2) in MS4 and MF4. The rate due to prompt muons, decay muons and punchthrough particles is indicated.

where the EC tapers to a thickness of 25 cm. In order to investigate the possible effect of the EC thickness on punchthrough, the simulation was run again replacing the tapered EC with an EC of constant thickness, which filled the entire space up to the beginning of the HC. Again, an averaged material composed of BGO was used to approximate the EC absorber medium. The result of this simulation is presented in Figure 4.18. One sees that with a constant thickness EC the increased rate between $\eta = 1.1$ and $\eta = 1.4$ is no longer present. The increased rate may be explained in the following way: With the tapered EC, there is an air gap between the EC and the HC. Low energy pions and kaons, produced in hadronic showers originating in the EC, enter this air gap and have a high probability to decay, thus producing additional punchthrough muons in this area.

As discussed in Section 2.2.3, we expect the hit rate due to neutrons and gammas to be large, especially on the outer most muon stations. In MS1 ($\eta < 1.5$) the rate

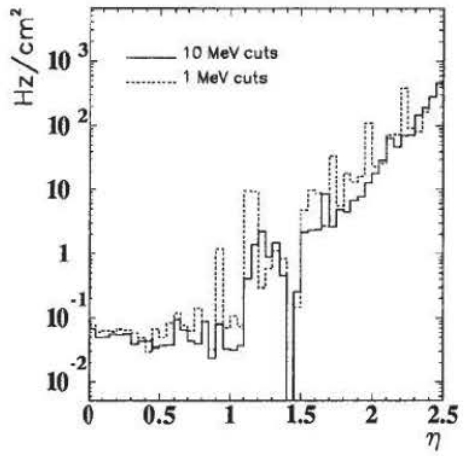

Figure 4.17: The charged particle rate (Hz/cm^2) in MS1 and MF1. The rate shown is the sum of punchthrough particles and decay muons. A comparison is made between the simulation results with 1 MeV and 10 MeV energy cut-offs.

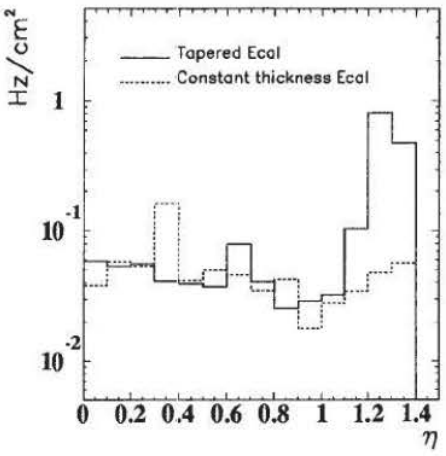

Figure 4.18: The charged particle rate (Hz/cm^2) in MS1. The rate shown is the sum of punchthrough particles and decay muons. A comparison is made between the simulation with a tapered EC and a constant thickness EC.

due to neutrals is expected to be less than 5×10^{-3} Hz/cm^2, much less than the total rate due to charged particles. In station MF1 ($\eta > 1.5$), the rate due to neutrals rises above the total rate due to charged particles and is larger by about a factor of 4. In MS4 and MF4, the rate due to neutrals is larger than the total charged particle rate by several orders of magnitude [24]. One should note that the neutral rates presented here are preliminary estimates and may be reduced substantially by an optimization of the shielding and moderators.

4.3.6 Angular Distributions and Trigger Rates

A trigger system that uses only one point (layer) per muon station can be disturbed by accidental hits. As mentioned above, the hit rate in the muon chambers due to neutrons and gammas is expected to be very high. Therefore, it may become necessary to build a trigger system that uses several layers in a muon station. Such a system should not only be able to distinguish between single hits and track segments, the angle of the track segment can also be used as the trigger criterion, if the angular resolution of the chamber is good enough. In addition to the suppression of single hits, such a trigger system can also reduce the punchthrough and decay muon background, already at the level of a single muon station.

We studied the angular distributions of punchthrough, decay and prompt muons reaching the first muon station of CMS (MS1 and MF1). We compare each muon track with a straight line coming from the collision vertex, which corresponds to an infinite momentum track. In Figures 4.19 and 4.20, we show the angular difference between these infinite momentum tracks and tracks produced by punchthrough and decay muons. These plots also contain the angular distributions of the prompt muons with a cut on initial $p_T \geq 10\,\mathrm{GeV}/c$, which can be considered as the distributions of

the "signal" muons. We use the prompt muon distribution to define an angular cut which corresponds to $p_T^{cut} \geq 10\ GeV/c$. The cut angle was chosen so that we loose less than 10 % of the signal. The distribution of the prompt muons without a cut on p_T is not shown.

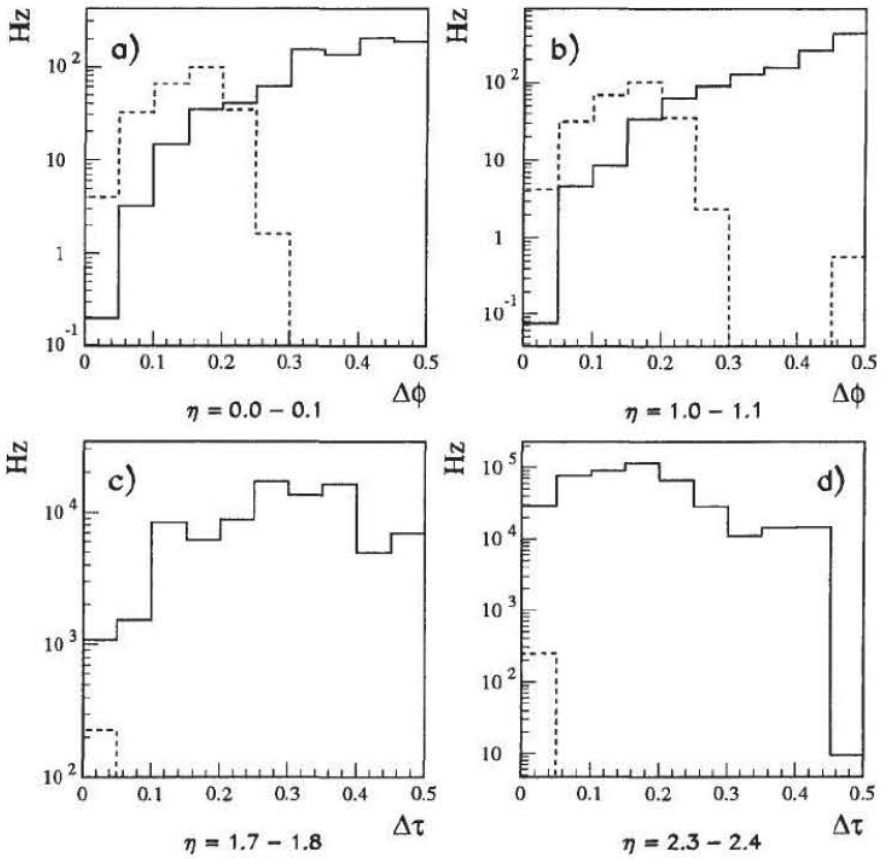

Figure 4.19: **MS1/MF1:** Angular difference $\Delta\phi$ and $\Delta\tau$ between simulated muons and infinite momentum tracks for punchthrough and decay muons (solid line, no cut) and prompt muons with initial $p_T \geq 10\,\mathrm{GeV/c}$ (dashed line), for four different pseudorapidity intervals. a) and b) show the angle $\Delta\phi$ measured by the wires parallel to beam (barrel chambers), c) and d) show the angle $\Delta\tau$ measured by the radial wires/strips (end-cap chambers).

Figures 4.19 a) and b) show the angular difference $\Delta\phi$ for two pseudorapidity intervals in MS1. The angle ϕ is the angle in the projection perpendicular to the

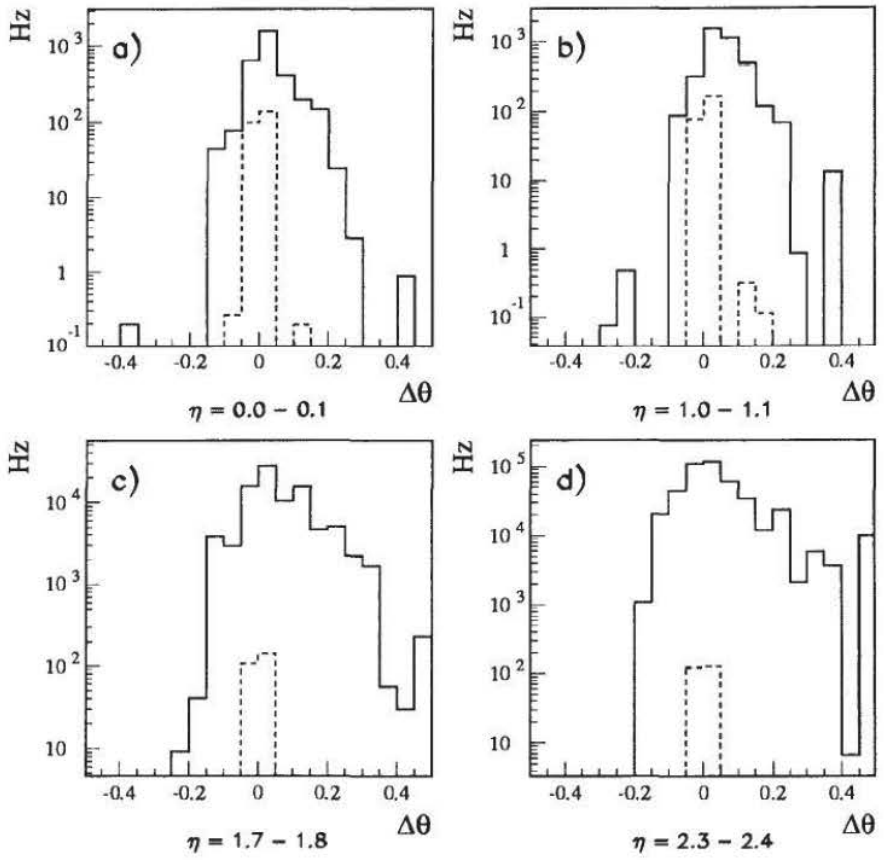

Figure 4.20: **MS1/MF1:** Angular difference $\Delta\theta$ between simulated muons and infinite momentum tracks for punchthrough and decay muons (solid line, no cut) and prompt muons with initial $p_T \geq 10\,\mathrm{GeV}/c$ (dashed line), for four different pseudo-rapidity intervals. This is the projection in the non-bending plane (at least in the barrel).

magnetic field, as usual. In the end-cap region this angle is not measured with only one projection of a muon chamber, because there are no readout strips in this direction. For that reason Figure 4.19 c) and d) shows the angular difference $\Delta\tau$. τ is the projected angle along the strip direction and is directly measured by the radial readout strips of the end-cap chambers. For $\Delta\phi$ and $\Delta\tau$ we give only the absolute value.

Figure 4.20 gives the angular difference $\Delta\theta$, which is the usual polar angle with respect to the beam and in the non-bending plane. The angle θ is measured in both the barrel and end-cap chambers. The distribution of $\Delta\theta$ is asymmetric and we give it including the sign. This asymmetry is a geometrical effect; in this projection the incidence direction of an infinite momentum particle is not perpendicular to the chamber. The angular difference $\Delta\theta$ for prompt muons is caused by multiple scattering in the calorimeter. In the case of the decay and punchthrough muons, the angular difference $\Delta\theta$ is also caused by multiple scattering in the calorimeter, and there is an additional contribution coming from the muon's production angle in the central tracker (for the decay muons) or production angle in the calorimeter (for punchthrough muons).

In Table 4.3 we give the trigger rates of a trigger system which employs an angular cut to distinguish the muon background, of punchthrough, decay and low p_T prompt muons, from the high p_T muon signal ($p_T \geq 10\,\mathrm{GeV}/c$). The columns entitled *reduction* give the fraction of the background and prompt muons that pass the angular cut. Note that the column for the prompt muons includes also the low p_T prompt muons, which are background. Table 4.4 gives the trigger rate in the barrel corresponding to $p_T^{\mathrm{cut}} > 20\,\mathrm{GeV}/c$ and $p_T^{\mathrm{cut}} > 50\,\mathrm{GeV}/c$.

The angular trigger based on $\Delta\phi/\Delta\tau$ is able to make an efficient cut on the muon's transverse momentum. Such a trigger can reduce the background trigger rate

by a factor of more than 20, for $p_T^{\rm cut} > 10\,{\rm GeV}/c$. This large reduction is achieved because of the strong solenoidal field in CMS. The background muons, with their softer momentum spectrum, are well separated from the prompt muon signal, due to strong bending in the transverse plane.

In the end-cap region we also get a reduction factor of about 20 (for $p_T^{\rm cut} > 10\,{\rm GeV}/c$), however, the trigger rates are still very high. In the end-cap region one has to use a more narrow angular cut ($< 50\,{\rm mr}$). This is required because of the weaker magnetic bending for muons traveling in the forward direction. The tightening of this cut, for further background reduction, may become difficult to realize in a trigger system.

The angular trigger based on $\Delta\theta$ is less effective in separating the background muons from the signal. One might hope that, by combining the normal cut on p_T ($\Delta\phi/\Delta\tau$) with an additional cut on $\Delta\theta$, that one could achieve an additional reduction in the background trigger rate. However, we see that for $p_T^{\rm cut} > 10\,{\rm GeV}/c$, the angular resolution needed in the non-bending plane (θ projection) is of the order 20 mr. This resolution would be difficult to achieve with the detectors foreseen for the CMS muon system. On the other hand, a rough cut on the angular difference $\Delta\theta$, could still be useful for rejecting halo muons which are traveling parallel with the beam line.

4.4 Conclusion

In this study we estimated the charged particle flux emerging from the collision vertex at the LHC by running the Monte Carlo program PYTHIA. We simulated the interaction of these particles in the CMS detector with the GEANT-based program CMSIM. From this simulation we derived the momentum spectrum of prompt, decay and punchthrough muons reaching the first muon station of CMS (MS1 and MF1).

$< 10\,\%$ loss of signal muons with $p_T \geq 10\,\mathrm{GeV}$					
MS1/MF1		ϕ/τ-projection			
pseudorapidity	angular	punchthrough and decay		prompt muons	
η	cut (mr)	reduction	rate (kHz)	reduction	rate (kHz)
$0.0 - 0.1$	250	0.03	0.1	0.13	0.33
$1.0 - 1.1$	250	0.03	0.1	0.12	0.35
$1.7 - 1.8$	50	0.01	1.	0.03	0.61
$2.3 - 2.4$	20	0.04	18.	0.03	1.6
MS1/MF1		θ-projection			
$0.0 - 0.1$	20	0.37	1.2	0.46	1.2
$1.0 - 1.1$	20	0.22	0.8	0.35	1.0
$1.7 - 1.8$	10	0.13	12.	0.20	4.
$2.3 - 2.4$	10	0.17	80.	0.25	13.

Table 4.3: Expected muon trigger rates of an angular trigger for four pseudorapidity intervals. The second column gives the angular cut that corresponds to a loss of less than $10\,\%$ of the prompt muons with $p_T \geq 10\,\mathrm{GeV}$. The third and fifth columns give the fraction of punchthrough muons, decay muons and prompt muons that still pass these cuts. The other columns give the corresponding trigger rates. The columns for the prompt muons include also the low p_T muons.

$< 10\,\%$ loss of signal muons with $p_T \geq 20\,\mathrm{GeV}$					
MS1/MF1		ϕ-projection			
pseudorapidity	angular	punchthrough and decay		prompt muons	
η	cut (mr)	reduction	rate (kHz)	reduction	rate (kHz)
$0.0 - 0.1$	100	0.001	0.003	0.014	0.04
$1.0 - 1.1$	100	0.001	0.005	0.012	0.04
$< 10\,\%$ loss of signal muons with $p_T \geq 50\,\mathrm{GeV}$					
$0.0 - 0.1$	40	0.00006	0.0002	0.0008	0.002
$1.0 - 1.1$	40	0.00002	0.0001	0.0006	0.002

Table 4.4: Expected muon trigger rates of an angular trigger for two pseudorapidity intervals, as in Table 4.3. Here the angular cuts correspond to a p_T^{cut} on prompt muons $\geq 20\,\mathrm{GeV}/c$ and $\geq 50\,\mathrm{GeV}/c$.

The charged particle rate in each muon station, due to prompt muons, decay muons and punchthrough particles, was also determined. Furthermore, the trigger rate, of a trigger system which uses the angle of the muon in the first muon station as a trigger criteria, was estimated.

We showed that the total charged particle rate is $0.1\,\mathrm{Hz/cm^2}$ in MS1 at $\eta = 0$ and rises up to $\approx 300\,\mathrm{Hz/cm^2}$ in the end-cap at $\eta = 2.5$. The charged particle rate in Station 4 is $< 0.01\,\mathrm{Hz/cm^2}$ at $\eta = 0$ and rises to $5\,\mathrm{Hz/cm^2}$ at $\eta = 2.5$. The rate due to photons and neutrons in MS4/MF4 is expected to be several orders of magnitude higher but may be reduced by an optimization of shielding and moderators.

A trigger system, that distinguishes between single hits and track segments, could be helpful to suppress the "neutral" background. It was shown that a trigger system which uses the angular difference $\Delta\phi$ to distinguish the low p_T background muons from the high p_T muon signal can reduce the muon background trigger rate by a factor 20 (for $p_T^{\mathrm{cut}} > 10\,\mathrm{GeV}/c$). A cut on the angular difference in the non-bending plane ($\Delta\theta$) was able to reduce the background trigger rate by a factor 6, however, the required angular cut was 20 mr in the barrel and 10 mr in the end-cap; such an angular resolution may be difficult to realize in a trigger system.

In this study we have disregarded the jet structure of the events resulting from the p-p collisions and instead simulated hadrons and muons distributed uniformly in ϕ and η. This approach was motivated by the desire to reduce the required CPU time and thus increase statistics. For future studies one may want to investigate the effect of punchthrough muons correlated with high p_T jets.

One uncertainty in our study comes from the simulation of minimum bias events at LHC energies. It has been shown [55] that the particle rates from the vertex, predicted by the Monte Carlo programs ISAJET and PYTHIA, agree to within 50%

of each other. This indicates the amount of systematic uncertainty introduced at the level of the generated hadron and prompt muon spectrum.

Bibliography

[1] Three introductory texts:

F. Halzen and A.D. Martin, *Quarks and Leptons: An Introductory course in Modern Particle Physics*, (John Wiley & Sons, New York, 1984);

D.H. Perkins, *Introduction to High Energy Physics, 3rd edition*, (Addison-Wesley, Reading Massachusetts, 1987);

M.G. Bowler, *Femtophysics: A Short Course on Particle Physics*, (Pergamon, Oxford, 1990).

[2] *Particles and Fields*, Phys. Rev. D, Vol. 50, Num. 3 (1994) 1194.

[3] CDF Collaboration, *Evidence for Top Quark Production in $p\bar{p}$ Collisions at $\sqrt{s} =$ 1.8 TeV*, **FERMILAB-PUB-94/097-E** (1994).

[4] R.P Feynman, *Rev. Mod. Phys* **20** (1948) 267;

J. Schwinger, *Phys. rev.* **73** (1948) 416;

S. Tomonaga, *Phys. rev.* **74** (1948) 224.

[5] E. Fermi, *Z. Phys.* **88** (1934) 161.

[6] S.L. Glashow, *Nucl. Phys.* **10** (1959) 107;

S. Weinberg, *Phys. Rev. Lett.* **19** (1967) 1264;

A. Salam and J.C. Ward, *Nuovo Cimento* **11** (1959) 568;

A. Salam, *Proc. 8th Nobel Symposium, Aspenäsgarden, Sweden: Elementary Particle Theory,* N. Svartholm (ed.) (Almquist and Wiksell, Stockholm, 1968) p. 367.

[7] N. Cabibbo, *Phys. Rev. Lett.* **10** (1963) 531;
M. Kobayashi and T. Maskawa, *Progr. Th. Phys.* **49** (1973) 652.

[8] M.J. Shochet, *Physics of Proton Antiproton Collisions*, **FERMILAB-CONF-91/341-E** (1991);
M.G. Bowler, *Femtophysics: A Short Course on Particle Physics*, (Pergamon, Oxford, 1990).

[9] P.W. Higgs, *Phys. Lett.* **12** (1964) 132.

[10] G. Giacomelli and P. Giacomelli, *Particle Searches at LEP*, **CERN PPE/93-107** (1993).

[11] D.H. Perkins, *Introduction to High Energy Physics, 3rd edition*, (Addison-Wesley, Reading Massachusetts, 1987) p. 339-340.

[12] D. Denegri, *Standard Model Physics at the LHC (pp Collisions)*, Proc. LHC Workshop, Vol.I, Aachen, 1990, eds. G. Jarlskog and D. Rein,
CERN 90-10, p.56;
G. Altarelli, *ibid*, p.153.

[13] Letter of Intent, Atlas Collaboration, **CERN LHCC/92-4** (1992).

[14] Letter of Intent, CMS Collaboration, **CERN LHCC/92-3** (1992).

[15] F. Gasparini et al., Nucl. Instr. and Meth. **A336** (1993) 91.

[16] R. Santonico and R. Cardarelli, Nucl. Instr. and Meth. **A187** (1981) 377;
R. Cardarelli et al., Nucl. Instr. and Meth. **A263** (1988) 20.

[17] A. Nisati, *Muon Rates at the LHC*, Proc. LHC Workshop, Vol.III, Aachen, 1990, eds. G. Jarlskog and D. Rein, **CERN 90-10** p.442.

[18] M. Della Negra et al., *Study of Muon Triggers and Momentum Reconstruction in a Strong Magnetic Field for a Muon Detector at LHC*, **CERN DRDC/90-36, DRDC/P7.**

[19] A. Bodek, *Punchthrough in Hadronic Showers, Muon Identification, and Scaling Laws for Different Absorbers*, Univ. of Rochester pre-print **UR-911** (1985).

[20] F. Lacava, *Punchthrough in Hadronic Showers: A Parameterization of the Total Probability*, Roma Univ. pre-print **ROM-NI 968** (1990).

[21] H. Fesefeldt et al., Nucl, Instr. and Meth. **A292** (1990) 279.

[22] D. Green et al., Nucl. Instr. and Meth. **A244** (1986) 356;
D. Green and D. Hedin, Nucl. Instr. and Meth. **A297** (1990) 111.

[23] P.A. Aarnio and M. Huhtinen, Nucl. Instr. and Meth. **A336** (1993) 98.

[24] M. Huhtinen and P.A. Aarnio, *Radiation problems at LHC experiments I: Neutral particle background*, **CMS TN/94-135** (1994).

[25] Y. Fisyak, K. McFarline and G. Mitselmakher, *Neutron and γ backgrounds in GEM and CMS muon systems*, **CMS TN/94-147** (1994).

[26] I. Azhgirey and A. Uzunian, *CMS Muon System Radiation Background Shielding*, **CMS TN/94-266** (1994).

[27] M. Huhtinen and G. Wrochna, *Estimation of the RPC Muon Trigger Rates Due to Neutral Particles*, **CMS TN/94-138** (1994).

[28] Á. Csilling et al., *Muon Trigger Rates*, **CMS TN/94-282** (1994).

[29] T. Del Prete and C. Petridou, *Energy Loss by Muons in Dense Materials*, Proc. LHC Workshop, Vol.III, Aachen, 1990, eds. G. Jarlskog and D. Rein, **CERN 90-10** p.477.

[30] C. Albajar et al. (RD5 collaboration), *Electromagnetic Secondaries in the Detection of High Energy Muons*, **CERN PPE/94-204** (1994). *Submitted to Zeitschrift Für Physik C*

[31] I. Hietanen et al., Nucl. Instr. and Meth. **A310** (1991) 671.

[32] I. Hietanen et al., Nucl. Instr. and Meth. **A310** (1991) 677.

[33] H. Van der Graaf, Nucl. Instr. and Meth. **A307** (1991) 220.

[34] H. Faissner et al., Nucl. Instr. and Meth. **A330** (1993) 76.

[35] J. Shank et al., *Test beam results from the GEM Prototype CSC in RD5*, **GEM TN/93-402** (1993).

[36] RD5 Status Report 1991, **CERN DRDC/91-53.**

[37] RD5 Status Report 1993, **CERN DRDC/93-49.**

[38] F. Bakker et al., Nucl. Instr. and Meth. **A330** (1993) 44.

[39] M. Aguilar-Benitez et al., Nucl. Instr. and Meth. **A258** (1987) 26.

[40] J.L. Bénichou, A. Hervé and G. Waurick, *Absorber Magnet for RD5*, **RD5 TN/91-01.**

[41] K. Eggert et al., Nucl. Instr. and Meth. **176** (1980) 217;
C. Albajar et al., Z. Phys. **C44** (1989) 15.

[42] M. Aguilar-Benitez et al., Nucl. Instr. and Meth. **A205** (1983) 79.

[43] M. Aalste et al., Z. Phys. **C60** (1993) 1.

[44] C.R. Lyndon and A. Sanjari, *Simulation Studies of Punchthrough Measurements for CERN Experiment RD5*, **RD5 TN/93-13** (1993).

[45] R. Brun, M. Hansroul and L.C. Lassalle, *GEANT User's Guide*, **CERN DD/EE/82**, (1982);
CERN Program Library Long Writeup **W5013**.

[46] H. Fesefeldt, *The Simulation of Hadronic Showers - Physics and Applications*, RWTH Aachen Report **PITHA 85/02** (1985);
H. Fesefeldt, Proc. 3rd Pisa Meeting on Advanced Detectors, Castiglione della Pescaia, 1986;
H. Fesefeldt, Nucl. Instr. and Meth. **A263** (1988) 114.

[47] A. Fassò, A. Ferrari, J. Ranft, P.R. Sala, G.R. Stevenson and J.M. Zavula. FLUKA92. In *Proceedings of the Workshop on Simulating Accelerator Radiation Environments*, Santa Fe, USA, 11-15 January 1993.

[48] *Review of Particle Properties, Part 2*, Phys. Rev. D, Vol. 45, Num. 11, (1992) p. III.86 - III.88.

[49] P. H. Sandler et al., Phys. Rev. **D 42** (1990) 759.

[50] G.L. Bencze et al., Nucl. Instr. and Meth. **A340** (1994) 466.

[51] F. S. Merritt et al., Nucl. Instr. and Meth. **A245** (1986) 27.

[52] C. Albajar et al., Nucl. Phys. **B335** (1990) 261.

[53] G. Ciapetti and A. Di Ciaccio, *Monte Carlo Simulation of Minimum Bias Events at the LHC Energy*, Proc. LHC Workshop Aachen, 1990, eds. G. Jarlskog and D. Rein, **CERN 90-10**.

[54] H.-U. Bengtsson and T. Sjostrand, Computer Physics Commun. **46** (1987) 43;
T. Sjostrand, **CERN TH/7112-93** (1993).

[55] M. Konecki, J. Królikowski and G. Wrochna, *Simulation of the RPC Based, Single Muon Trigger for CMS*, **CMS TN/92-39**.

[56] C. Charlot et al.,*CMS Simulation Facilities*, **CMS TN/93-63**.

[57] The CMS Collaboration,*CMS Status Report and Milestones*, **CERN LHCC/93-48**.

[58] Á. Csilling et al., *Simulation of the CMS Muon Trigger System*, **CMS TN/94-174** (1994).

Appendix A

Tracking with Scintillating Fibers and Visible Light Photon Counters

Over the past decade there has been an increasing interest in scintillating fiber detectors in such fields as tracking and calorimetry in high energy physics [1], gamma ray telescopes for astrophysics and devices for medical imaging [2]. This technique, as applied to particle tracking, has its origins in the 50's [3], but further development was soon abandoned due to the superior position resolution of bubble and spark chambers [5]. Renewed interest in this detector technology has occurred because of the improved optical performance of scintillating fibers and the invention of photo-detectors with sensitivity to individual photons and high quantum efficiency.

In order to cope with the demanding experimental environment at the SSC, a scintillating fiber tracking system was proposed as part of the detector being built by the Solenoid Detector Collaboration (SDC) [4]. A subset of the SDC, The Fiber Tracking Group (FTG), was formed to develop and prove the feasibility of this technology. A scintillating fiber tracking system is also part of the planned upgrade of the D0 detector at FNAL.

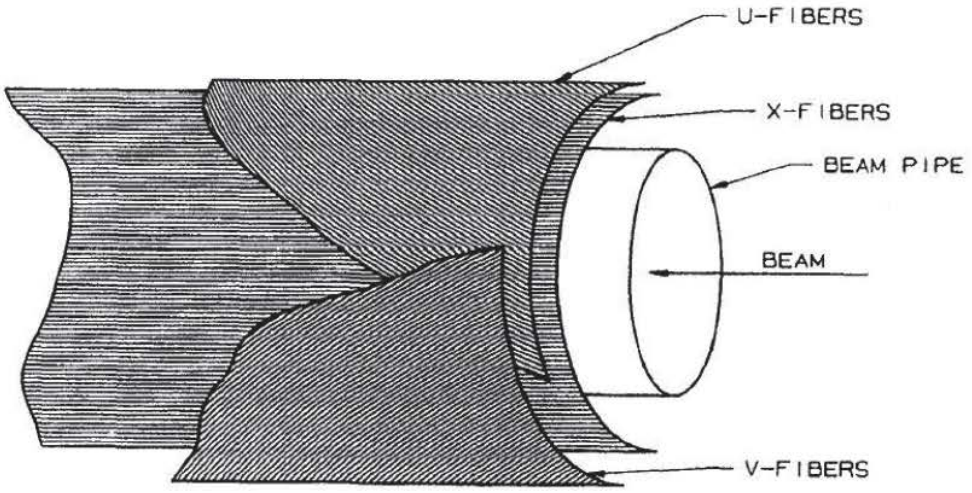

Figure A.1: A fiber superlayer with one layer parallel to the beam direction and two stereo layers.

The tracking system envisioned for the SDC consists of a silicon inner tracker at radii r $<$ 50 cm and superlayers of scintillating fibers surrounding the interaction region starting at a radius r = 60 cm. Each superlayer will consist of four separate fiber layers: two parallel to the beam direction to measure the rϕ coordinate, and two stereo layers at an angle of about 4° to measure the z coordinate (see Figure A.1).

The scintillating fibers will be attached to clear non-scintillating light guides in order to bring the light signal from the tracking volume to the readout system. The clear fibers will be coupled directly to solid state photomultipliers. A schematic of the SDC scintillating fiber tracking system is presented in Figure A.2.

The fibers will be used in a digital mode. Either the fiber records a hit or no hit. The resolution one can obtain from N layers of fibers with diameter D and each layer offset by D/N is,

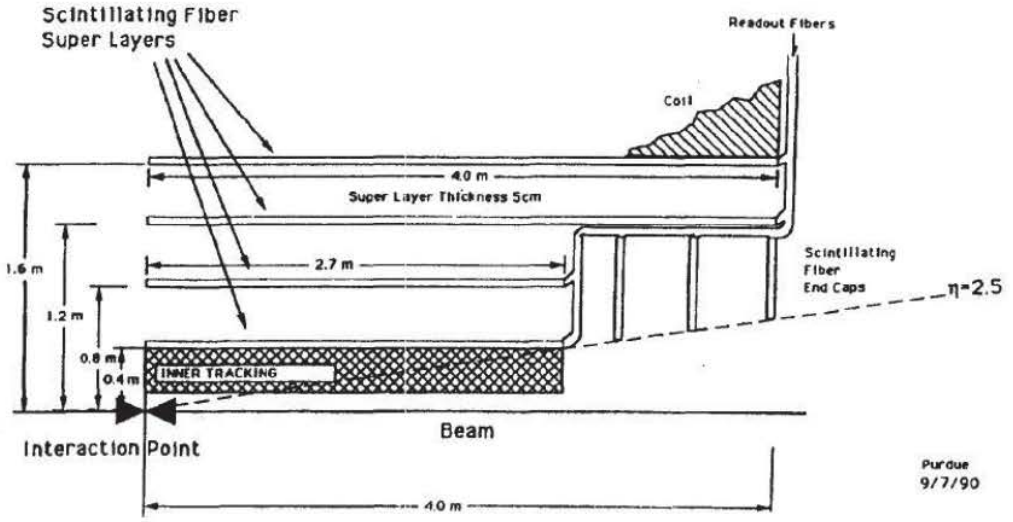

Figure A.2: A schematic of the SDC scintillating fiber central tracking system.

$$\sigma = \frac{D}{\sqrt{12}} \frac{1}{N}.$$

The system has been designed to have 830 μm diameter fibers. The expected resolution is 240 μm if one uses a single fiber to define a track point and 120 μm if one uses a fiber doublet.

In this chapter the major components of this system and the research and development that was conducted in order to realize this detector will be described.

A.1 Scintillating Fibers

It is well known that fiber optic technology has revolutionized the telecommunications industry. *Scintillating* optical fibers have essentially the same function as conventional

optical fibers, being that of transmitting a light signal from a source to a distant optical detector. The main difference between the two is in the source of photons. In the case of telecommunication fiber optics, digital information is converted to light pulses through the use of photodiodes. Photodiodes can produce intense light pulses which will propagate long distances through the fibers. Scintillating fiber systems, however, are limited to the relatively few photons produced in the fiber itself as the result of excitation by ionizing radiation. Therefore, one must choose scintillating materials which maximize the primary light output caused by the charged particle and reduce as much as possible the sources of light loss and absorption which attenuate the light signal as it propagates down the fiber, and finally one must employ photodetectors with high quantum efficiency in order to detect efficiently the small number of photons which survive.

A.1.1 The Scintillation Mechanism

Organic scintillators are aromatic hydrocarbon compounds containing benzene-ring structures [6]. When charged particles pass through an organic compound ions and electronically excited molecules are formed. The excited states involve the free valence electrons (called π-*electrons*) of the benzene-rings. Coupling between the π-states and the vibrational states of the molecule leads to a splitting of each π-state into a set of vibrational levels. The states are labeled S_{ij}, where i is the electronic excitation level and j is the vibrational sub-level (see Figure A.3).

Ion recombination, as well as the degradation of highly excited molecules, produce significant concentrations of first excited singlet and triplet states. Fast light emission, also called florescence, occurs when the π-electrons make transitions from the first excited singlet state S_{10} to the ground state S_{00} or to an intermediate vibrational

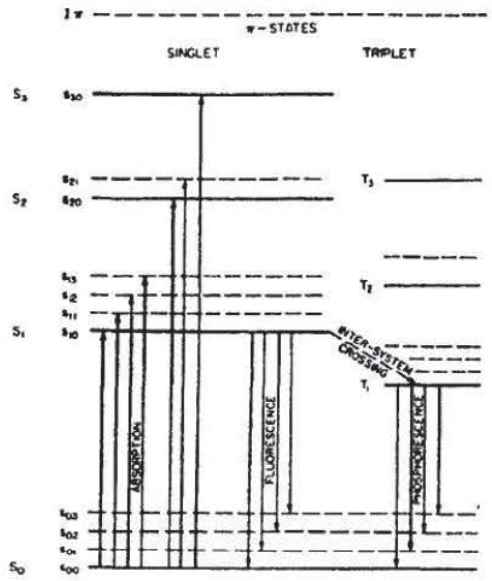

Figure A.3: π-electron energy levels of an organic molecule [6].

state S_{0j}. The decay time of these states is typically on the order of 1 to 5 ns, quite sufficient for the time scales encountered at the SSC or LHC. The triplet states are metastable, therefore, transitions from T_1 to S_{0j} can take from a microsecond to several milliseconds. This delayed light emission is called phosphorescence.

The π-electron energy levels of an organic compound determine its absorption and emission spectra. The shift of the emission spectrum to longer wavelengths occurs because the S_{10} states frequently decay to excited vibrational states S_{0j}, with emission of radiation energy less than that required for the initial transition $S_{00} \rightarrow S_{10}$. This is referred to as the *Stokes shift*. This also explains why scintillators are to a large extent transparent to their own radiation. However, there is not a total separation of the absorption and emission spectra. The region of overlap leads to self-absorption of the emitted light.

Pure organic liquids, such as toluene and xylene, and plastics, such as polystyrene (PS) and polyvinyltoluene are frequently doped with one or two additional scintillating compounds. These so-called *wavelength-shifting* solutes increase the quantum yield of the base scintillator (or solvent) and are chosen so that the wavelength of their emitted light matches the sensitivity range of the photo-detector. In order to have an efficient energy transfer from the solvent to the solute, the absorption spectrum of the solute must overlap the emission spectrum of the solvent. The energy transfer occurs through two different processes: 1) direct absorption of the light emitted by the base scintillator (radiative transfer) and 2) a resonant dipole-dipole process described by Förster [7]. For solute concentrations below 0.001 M (M = moles/liter) the radiative transfer dominates, while at concentrations above 0.01 M the transfer occurs mainly through the *Förster* process.

A.1.2 Light Trapping Efficiency

Scintillating fibers consist of a core material - usually polystyrene - doped with an appropriate wavelength shifting compound and has an index of refraction n_{core}. The surface of the fiber is covered with a thin non-scintillating cladding with an index of refraction n_{clad}. The core and cladding materials are chosen so that $n_{core} > n_{clad}$. Ionizing radiation traversing the fiber will excite the fiber core material which will in turn emit light isotopically. Most of the light rays will pass through the core-cladding interface and be lost. However, those light rays which meet the core-cladding interface at an angle $\theta > \theta_c$ will be totally internally reflected and thus transmitted down the fiber (see Figure A.4). The critical angle is given by, $\theta_c = \arcsin(n_{clad}/n_{core})$.

A fiber with a polystyrene core ($n_{core} = 1.58$) and PMMA[1] cladding ($n_{clad} = 1.49$)

[1] poly-methylmethacrylate

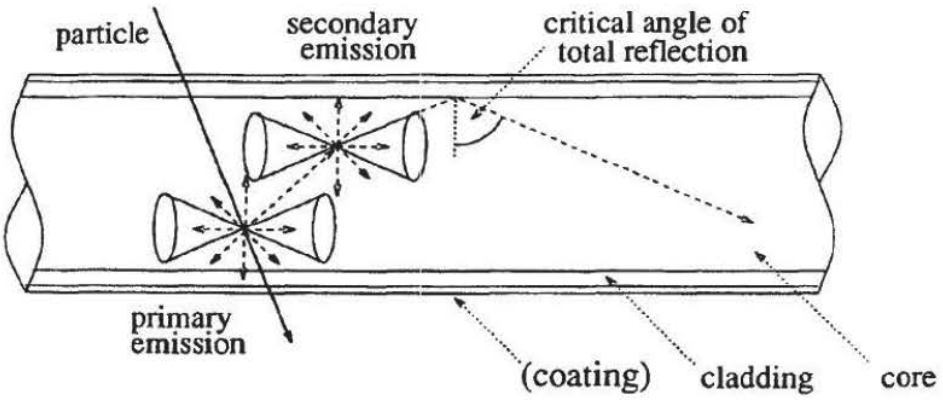

Figure A.4: Schematic view of the production and trapping of light in a plastic fiber containing two dopants [5].

has a critical angle $\theta_c = 71°$. The light trapping efficiency in one direction can be approximated by,

$$T_{efficiency} = \frac{1}{2}(1 - \frac{n_{clad}}{n_{core}}).$$

The fraction of light trapped can be increased by reducing the index of refraction of the cladding material. For example, the standard PMMA cladding can be replaced by fluorinated[2] polymethacrylate with $n_{clad} = 1.42$; this should increase the trapping efficiency by about a factor of 2 [8].

A.1.3 Light Transmission and Attenuation

Light attenuation in scintillating fibers is caused by two different processes: 1) reflection losses at the core-cladding interface and 2) bulk attenuation in the fiber core.

Reflection losses occur because of imperfections in the core-cladding interface re-

[2]H atoms of polymethacrylate replaced by F atoms

sulting in a reflection coefficient q less than unity. The reflection loss is directly proportional to the number of reflections a light ray must undergo as it travels down the fiber. The number of reflections is inversely proportional the fiber diameter. For large diameter fibers (d $>$ 0.5 mm) the reflection losses are small compared to the bulk attenuation. For small diameter fibers (d $<$ 0.1 mm) the reflection losses become important [9]. In any case, however, it is important to manufacture fibers with few imperfections in the core-cladding interface.

Bulk attenuation is mainly due to self-absorption by the dopant, caused by an overlap of the dopant's absorption and emission spectra, and absorption by the base scintillator. Absorption by the base scintillator can be reduced by use of appropriate wavelength-shifting compounds. In the common ternary system, PS doped with butyl-PBD[3] and DPOPOP[4], butyl-PBD is present in relatively high concentrations to provide a high light output, however, the peak of its emission spectrum (λ_{em} = 365 nm) lies in the opaque region of PS, therefore, DPOPOP (λ_{em} = 420 nm) is add to shift the light into the transparent region of PS. Another solution is to choose dopants such as PMP[5] and 3HF[6] which have both a large Stokes shift and emit in the transparent region of PS.

Another source of bulk attenuation, is Rayleigh scattering on submicron density variations in the core material. These losses can be reduced by improving the fiber production process.

---

[3] 2-(4'-t-butylphenyl)-5-(4"-biphenylyl)-1,3,4- oxadiazole
[4] 1,4-bis-[2-(5-phenyloxazolyl)]-benzene
[5] 1-phenyl-3-mesityl-2-pyrazoline
[6] 3-hydroxyflavone

A.2 Visible Light Photon Counters

Visible light photon counters (VLPCs) are a visible light version of the solid state photomultiplier (SSPM) developed by scientists at Rockwell International Science Center [10]. The application of the SSPM technology to scintillating fiber tracking was first initiated by Professor M. Atac in 1988 [11]. Since then research has been ongoing to optimize the VLPC for visible light operation, i.e. reducing the sensitivity to infrared photons, increasing the count rate capability and improving the quantum efficiency.

One can understand the operating principle of the VLPC by referring to Figure A.5. One sees that a visible photon enters the device from the top and is absorbed either in the undoped blocking layer, or the doped gain region below, creating an electron-hole pair. Taking first the case where the photon is absorbed in the blocking layer, the electron is collected in the top contact but the hole drifts into the gain region. There it produces free electrons by impact ionization of neutral donor impurities that are present in high concentrations. In the VLPC, a neutral donor is a substitutional ion with an electron bound to it in a hydrogen-like orbit with an ionization potential about 0.05 eV. When the concentration of such impurities is sufficiently high they form an energy band separated from the conduction band by the ionization energy. When the electric field is sufficiently high (2×10^3 to 10^4 V/cm) each initial electron starts an avalanche of free electrons forming a combined avalanche of about 5×10^4 electrons within a nanosecond.

In the case where the electron is absorbed in the gain region, the number of initial impact ionization electrons from the photo generated hole is smaller but the final number in the combined avalanche is the same as in the case where the photon is absorbed in the blocking layer. This is because, regardless of how they are formed,

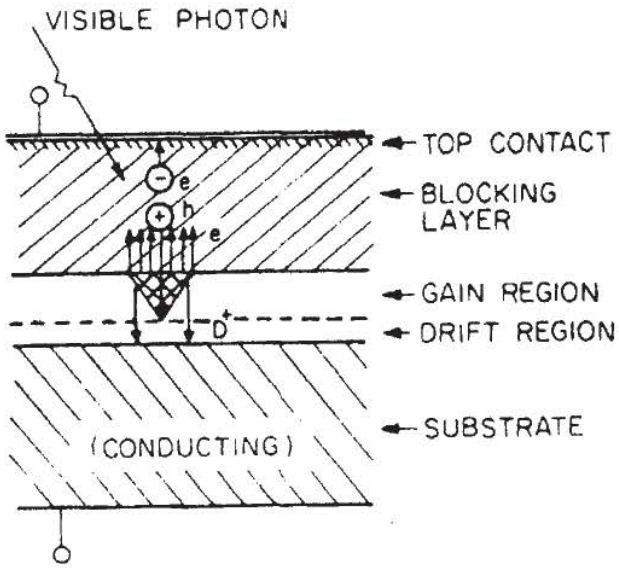

Figure A.5: Operation principles of the VLPC are indicated.

growth of the avalanche is limited. This limit is due to the localized recombination and field collapse induced by the spacecharge of the relatively immobile donor ions (holes in the impurity band) equal in number to the avalanche electrons. Positively charged impurity band holes formed in the avalanche drift to the bottom contact in about one microsecond. While the collection time of the positive change is relatively long, the ultimate rate capability of the device remains high. This is because the avalanche is limited to a region of about 6 μm diameter and the rest of the device, which has a total area of $800 \times 800 \mu m^2$, remains active. The operational characteristics of the VLPC are summarized in Table A.1.

As indicated in Table A.1, VLPCs need to be cryogenically cooled. The optimum operating temperature is near 6.5 K. The activation energy of electrons from the impurity band of the extrinsic semiconductor, Si:As, is about 0.05 eV, therefore, the

Table A.1: Characteristics of VLPC.

Parameter	Value
Pulse rise time	< 5 ns (limited by amplifier response)
Average gain	3×10^4
Gain dispersion	< 30 %
Quantum efficiency	> 70 %
Dead time	none (continuous)
After pulses	none (< 0.01 %)
Dark pulse rate	5×10^3 s^{-1}
Saturation pulse rate	2.5×10^7 s^{-1}/mm^2
Average power	~ 1.3 μW
Breakdown voltage	7.5 V
Operating voltage	6.5 V
Neutron damage level	$> 10^{12}$ n·cm^{-2}
Operating temperature	6.0 K to 7.0 K
Insensitivity to magnetic field	≤ 14 kG

thermal electron count rate would be intolerably high at temperatures about 10 K. However, the cooling of these devices for detection of visible light photons is not difficult. This is because the fibers greatly simplify the optical coupling of the devices inside the dewer, at liquid helium temperatures, to the room temperature environment. The fibers, designed to have high transmission in the visible light region, are natural blockers of the large flux of infrared background photons ($\sim 10^{18}$ ph/cm^2) to which the VLPCs are still sensitive even after substantial reduction of the infrared response. The quantum efficiency of the VLPC has its maximum in the region of visible light, between 400 and 700 nm and is compatible with the emission spectrum of 3HF. Figure A.6 shows the VLPC spectral quantum efficiency. In this figure, HISTE-I, II and III correspond to three different research prototypes. The final VLPC will have its quantum efficiency suppressed for photon wavelengths greater than 1μm.

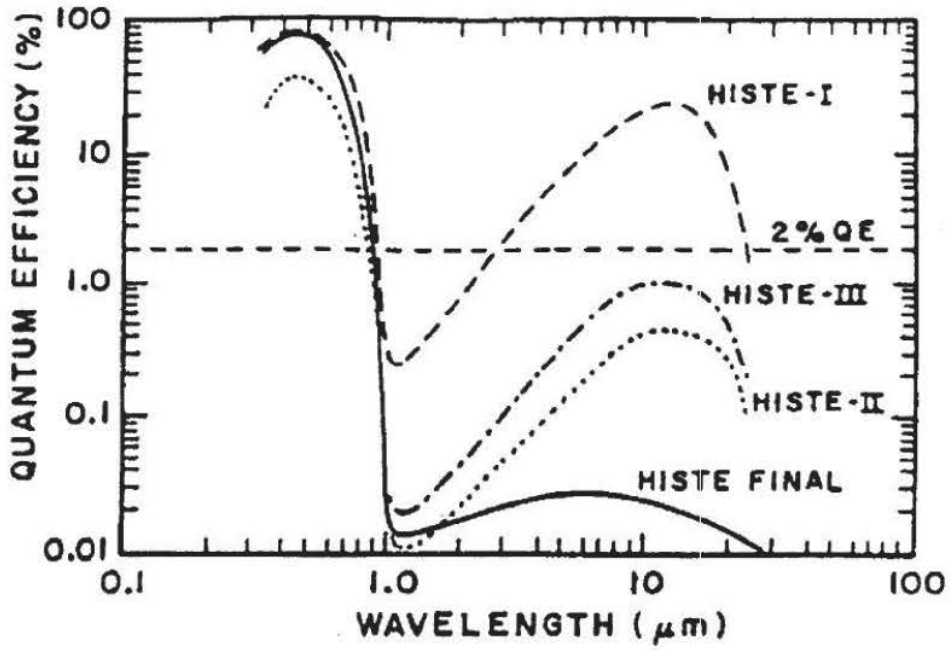

Figure A.6: VLPC spectral quantum efficiency. HISTE-I, II and III are three different VLPC research prototypes.

A.3 Photon Counting and Light Attenuation Measurement

An experiment was performed at UCLA to measure the number of photons that could be detected by a VLPC at the end of 4 meters of scintillating fiber plus 3 meters of clear fiber light guide [12]. These are the same lengths of fibers that will be used in the SDC central tracking system.

The measurements were made with Bicron 99-05 (PS-PTP[7]-3HF) scintillating fibers. The 4 m long scintillating fibers were irradiated by a collimated ^{90}Sr source. The fiber and source were enclosed inside a light tight box. The diameter of the collimator was 1 mm with a height of 12 mm. Two 1 mm$\times$1 mm square cross section scintillating fibers were kept below the collimator to provide a gate for a Le Croy 2249A CAMAC ADC. Figure A.7 shows the experimental arrangement. The core diameter of the scintillating fiber was 800μm, thus some of the selected, mainly minimum ionizing, beta particles would miss the scintillating fiber and make a coincidence in the fiber telescope below. The scintillating fiber was coupled to a clear non-scintillating light guide of the same diameter using optical grease in a Lucite ferrule with holes matching the fiber diameter. The length of the optical fiber that guided the photons to the VLPC was 3 m. It was kept in black flexible tubing between the light tight box and a simple cryostat. The cryostat kept the VLPC at the optimum temperature of 6.5 K. The cold end of the clear fiber was glued with Epoxi in a positioning hole that kept the fiber at a distance of about 75μm from the VLPC surface. The VLPC, the clear fiber and the signal and power carrying wires were all kept in the cold helium gas. This arrangement uses the enthalpy of the gas between

[7]para-terphenyl

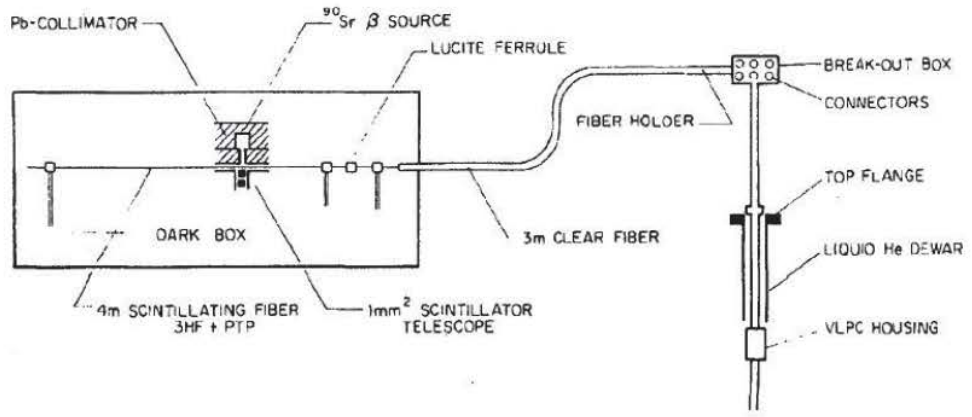

Figure A.7: Schematic of experimental arrangement showing a 4 m long scintillating fiber, with a 800μm diameter core, (PS-PPT-3HF) spliced to a 3 m long clear optical fiber that carried the photons to the VLPC.

6.5 K and room temperature and results in very small heat loss through the system.

As seen in Figure A.7, the clear fiber had at least three bends with radius of curvature as small as 6 cm. The experiments were performed with and without a mirror at the far end of the scintillating fiber. The pulse height spectra were taken when the source was at different positions with respect to the spliced fiber joint. Figures A.8a-d show the pulse height spectra, taken with the source at the position indicated. Also indicated is the weighted average number of photons detected by the VLPC when a simple mirror was attached to the end of the scintillating fiber with optical grease. As stated above, pedestal noise peaks were expected in the pulse height spectra due to the fact that the collimator was larger than the scintillating fiber diameter. One can also see the peaks corresponding to single and the multiple simultaneously detected photons which provided a direct pulse height calibration.

Figure A.9 summarizes the experimental results with and without the mirror in place. We see that there is a substantial gain in the number of detected photons when the mirror is used. An average number of 4 photons were detected at the end of 4 m

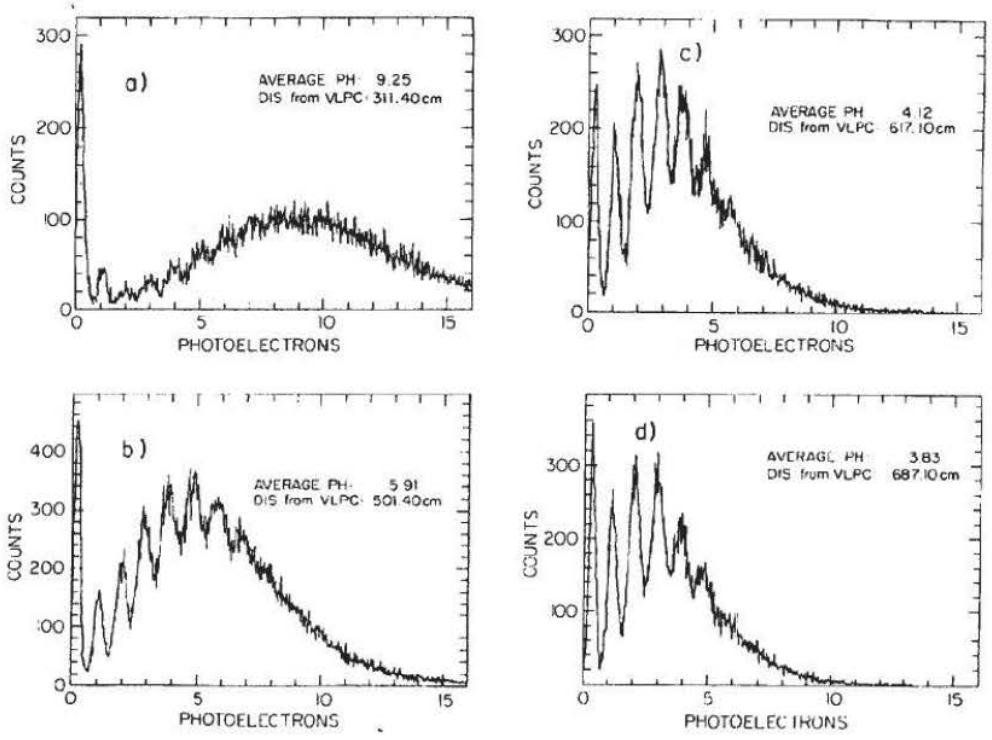

Figure A.8: Four pulse height spectra obtained with the ^{90}Sr source located at the positions indicated. The weighted average number of detected photons are given on the figures.

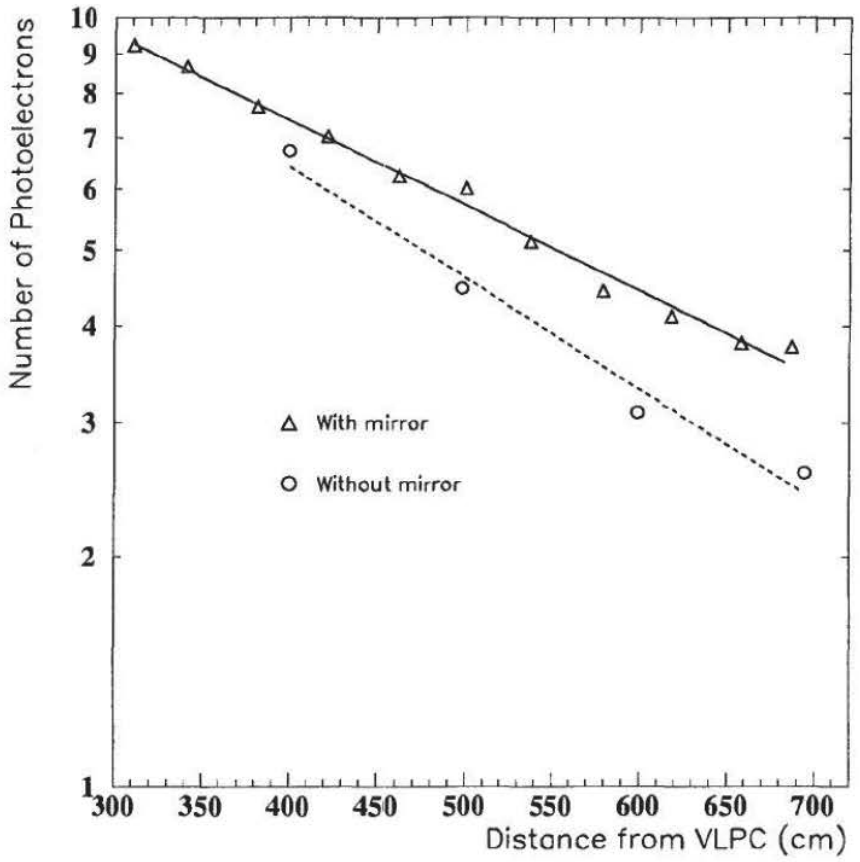

Figure A.9: Number of detected photons as a function of source position.

scintillating fiber plus 3 m of clear fiber. In addition, for data taken with the mirror in place, the measured attenuation length was 390 ± 3 cm; with no mirror at the end of the fiber ribbon, the measured attenuation length was 280 ± 10 cm.

A.4 A Prototype Fiber Tracking System

The goal of the next experiment, also conducted at UCLA [13], was to measure charged particle tracks from cosmic rays using the same length of fibers that will be used in the SDC detector and to show the feasibility of simultaneously operating multiple channels of VLPCs.

A.4.1 Experimental Setup of Cosmic Ray Test

Four scintillating fiber ribbons were stacked and placed in a rectangular black plastic channel. Each ribbon is composed of 8 scintillating fibers which were held together with white reflective acrylic paint. The 4 central fibers on each ribbon were used to make a 16 channel array. The scintillating fibers, 830 μm thick, were made of polystyrene doped with 1000 ppm 3HF, and were connected to the same diameter non-scintillating clear fibers using small acrylic blocks. The scintillating fiber ribbons were 4 meters, the clear fibers were 3 meters in length. Figure A.10 shows this experimental arrangement.

The acrylic blocks were precisely drilled to the fiber diameter and held together using pins and screws. The fibers were glued with epoxy to the acrylic block and their ends are polished to make good optical joints. A thin layer of optical grease was used between the blocks to improve the optical transmission. At the other end of the fiber array the fibers were placed into the same type of acrylic block and glued into place. The fibers were then polished and coupled directly to a mirror in order to reflect back light which would otherwise be lost out of the end of the fibers. The fiber geometry is shown in Figure A.11. The precise fiber geometry was determined by recording many cosmic ray tracks. By triggering on fibers in layers 1 and 4, and searching for the hit fiber or fibers in layers 2 and 3, the geometric alignment between

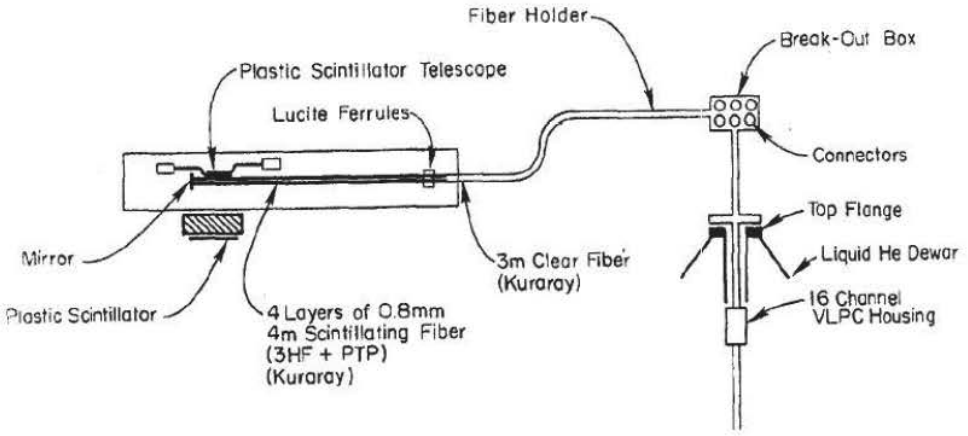

Figure A.10: Experimental arrangement for cosmic ray tests.

the fibers was determined. This was done for all combinations of the fibers in layers 1 and 4.

The cosmic ray trigger consisted of a plastic scintillator telescope of 0.7 cm by 10 cm size placed above the fiber array. The width of the telescope was chosen to be wider then the four central fibers so that there was no geometric limitation in the trigger. To ensure that the cosmic rays used for the test were minimum ionizing, a 10 cm thick lead brick and a third scintillator were placed below the fiber array. The experiment was performed with and without the brick in place.

A single bias voltage of 6.3 volts was used for the two 8 channel VLPC arrays. The signal from each VLPC element was amplified by a FET input transconductance amplifier[8] which has a rise time of 70 ns. Each amplifier was operated at the same bias voltage, resulting in a gain uniformity of 5% for all 16 channels. This gain uniformity can greatly simplify operation of these devices in large systems. The VLPCs were operating with a gain around 3×10^4. The operating temperature 6.5 K. The amplifiers

[8] AD3554-AM

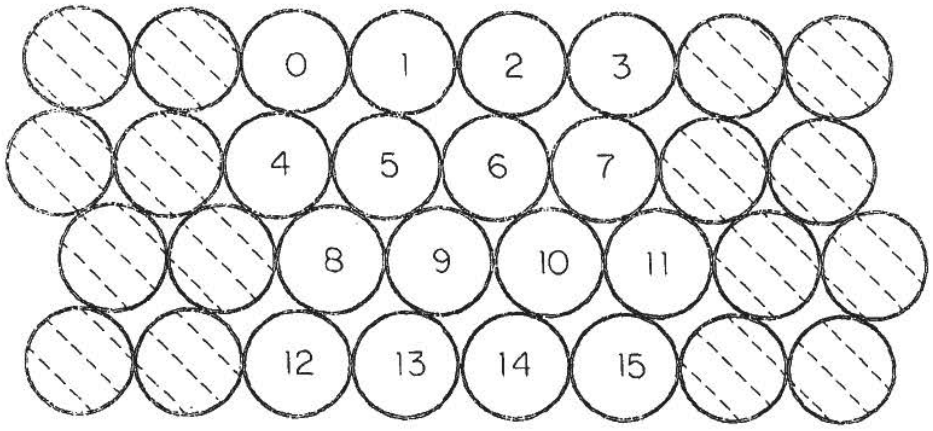

Figure A.11: Arrangement of fiber ribbon matrix. The numbered fibers in each ribbon were used in the tests. The geometry was determined by measuring cosmic ray tracks, i.e. triggering on fibers in the first and fourth layers and determining the fibers in the second and third layers which were also hit.

were readout using Le Croy 1885F FASTBUS ADCs. The ADCs have dual dynamic ranges with two slopes. This wide dynamic range is needed in order to measure charge up to 1000 pC.

A.4.2 Results of Cosmic Ray Test

Due to the low cosmic ray event rate, the ADC calibration was achieved by irradiating the fiber array with 1 MeV gamma rays from a ^{60}Co source and triggering on the light from the Compton electron produced inside an individual fiber. The source was held at the end of the 7 meter fiber array. Figure A.12 shows the pulse height spectrum obtained. The calibration between the number of photoelectrons and charge in picocoulombs was obtained from this spectra and is plotted in Figure A.13. In the fit the first photoelectron peak was not used because the signal threshold imposed excluded the lower tail of this peak. The threshold cut was necessary to reduce the

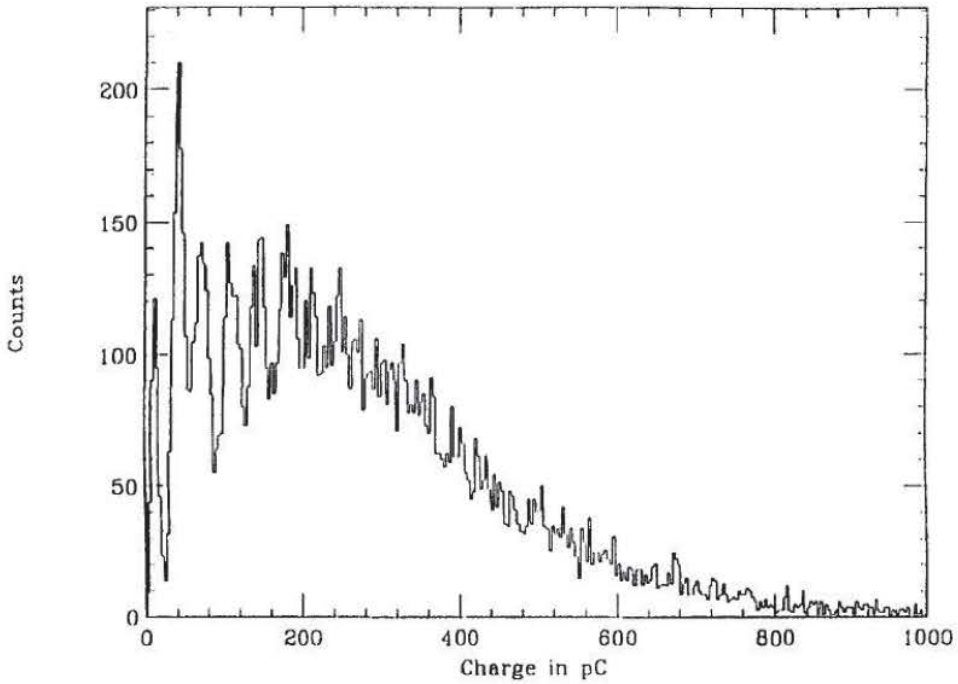

Figure A.12: Charge calibration using a ^{60}Co source. The photoelectron peaks were measured by detecting the photons produced by Compton electrons from the 1 MeV gamma rays. The peaks clearly identify the number of multiple photoelectrons detected by one of the VLPCs. This excellent pulse height resolution shows the power of the VLPCs in counting as few as one photon. We also see the pedestal noise peak.

single photoelectron peak that is mainly produced by the thermal electron background in this self triggering calibration mode of operation. The calibration was performed for each and every channel of the second and third fiber ribbon layers. Figure A.14 shows the corresponding charge in picocoulomb per photoelectron for each fiber channel in these layers. The variations are mainly due to gain variations of the transconductance amplifiers. The average value of 33 pC per photoelectron was taken to be the electronic gain for the tests presented below.

The plastic scintillator telescope indicated in Figure A.10 was placed at four dif-

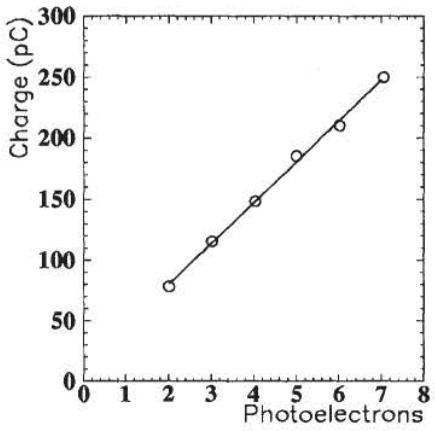

Figure A.13: The number of photoelectrons versus the charge in picocoulombs. This was determined for all fibers in the second and third layers.

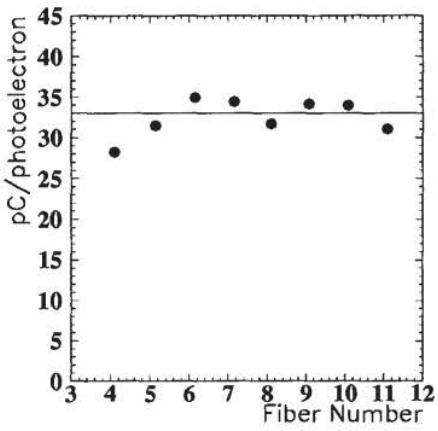

Figure A.14: Charge calibration per photoelectron for fibers 4 through 11. The variations are mainly due to the gain variations of the amplifiers. A separate test showed that the VLPC gain variations are within 5% under the same bias voltage.

ferent positions along the fiber array in order to trigger on cosmic rays. Several thousand events were accumulated at each position of the telescope. A large fraction of the tracks did not go through the 4 central fibers of the ribbons due to the fact that the width of the telescope was about twice as wide as the width of the four fibers. Figure A.15 shows the distribution of the number of photoelectrons produced by cosmic rays in the fibers in layer 3 when layers 1 and 2 were in coincidence with the scintillator telescope at a distance of 6.5 m from the VLPC. As seen in the figure the weighted average number of photoelectrons is 6.2. All events above 0.5 photoelectrons were accepted in the distribution. The distribution seen in Figure A.15 was the same within 0.1 photoelectrons when the telescope above the fiber array was in triple coincidence with the scintillator below the 10 cm thick lead brick. The inefficiency seen in the histogram distribution is mainly due to geometric arrangement of the fiber ribbons as shown in Figure A.11. Some of the cosmic ray tracks miss layer 3 due to the staggering of the layers.

Figure A.16 shows the average number of photoelectrons obtained from layers 2 and 3 at four different positions of the scintillator telescope. It also shows one data point when the mirror was removed from the end of the fibers.

The tracking efficiency of the second and third fiber layers, for minimum ionizing tracks, was obtained by triggering on the two middle fibers in layers 1 and 4 while counting the hits in the second and third layers. Figure A.17 shows the efficiency of the second and third layers as a function of trigger threshold in the first and fourth layers. It shows that the efficiency is flat between one and three photoelectron threshold cuts. About 95% efficiency was obtained by counting the hits in layer 2 and layer 3. About 98.7% efficiency was found by counting hits in either layer 2 or layer 3. The small inefficiency is mainly due to geometric effects produced by tracks passing

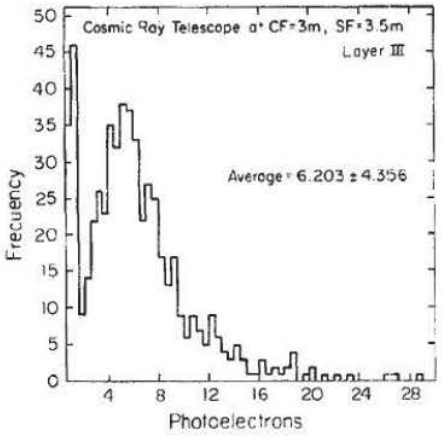

Figure A.15: The photoelectron distribution obtained from the cosmic rays passing through the fibers of the third layer at the distance of 6.5 meters from the VLPCs. It shows a Landau-like distribution. This is expected from thin fiber sampling of dE/dX.

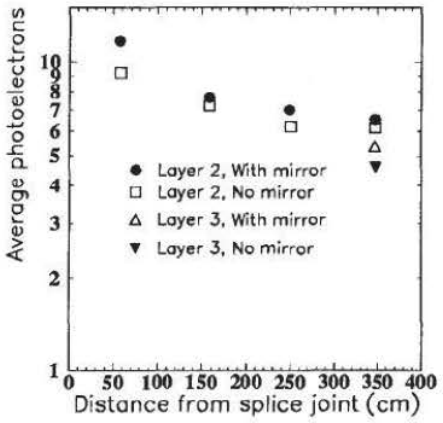

Figure A.16: The average number of photoelectrons obtained from the fibers in layers 2 and 3 when the cosmic ray telescope was located at the positions indicated. Data was taken with the mirror at the end of the scintillating fibers. One data point without the mirror in place is also given.

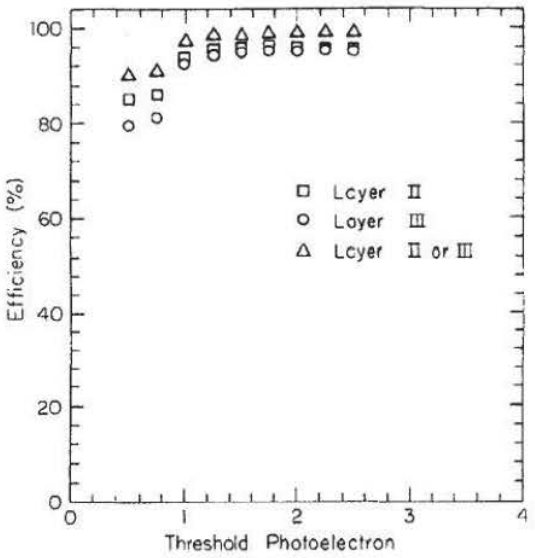

Figure A.17: Fiber tracking efficiency for fibers in layers 2 and 3 as a function of photoelectron threshold cut. In addition it shows the efficiency if layer 2 or layer 3 were hit. The efficiency for the half fiber staggered doublet is around 99%. For these plots the two middle fibers of layers 1 and 4 were used as triggers. The apparent inefficiency at the threshold cut below 1 photoelectron, is due to some triggers being produced by electronic noise and therefore it is not a true inefficiency.

through the non-scintillating fiber cladding. This 15μm thick cladding produces an effective gap in tracking.

Some typical cosmic ray tracks are shown in Figure A.18. The tracks are seen to be very clean without inter-fiber cross-talk. Figure A.19 shows some unusual tracks selected by computer. There is evidence for delta ray production, as indicated by the excessive number of photoelectrons either within the hit fiber or an adjacent fiber.

Furthermore, excellent time resolution is obtained. The time response of the VLPC has been tested using a fast transconductance preamplifier[9] [14]. The rise

[9]The VTX preamplifiers used by CDF collaboration

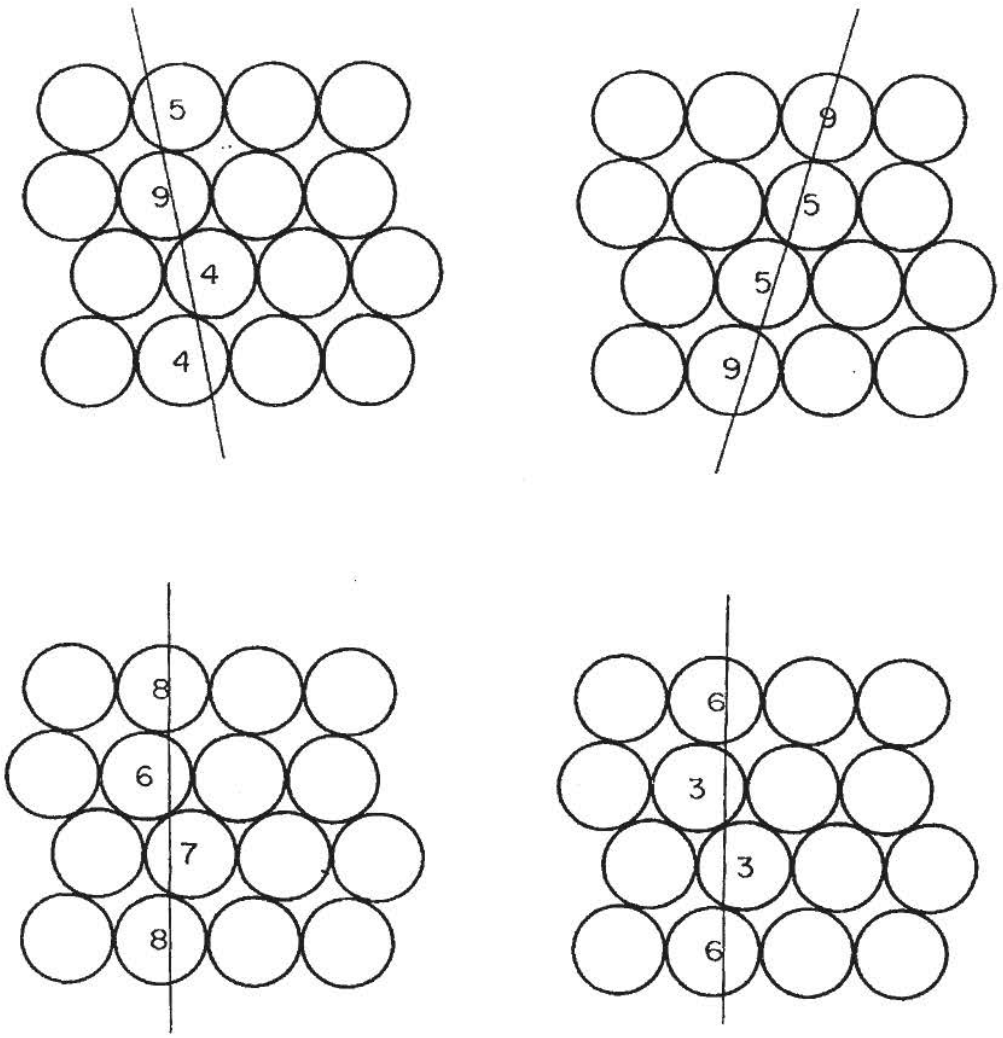

Figure A.18: Typical charged particle tracks. The number of photoelectrons detected from each fiber is indicated. The tracks are very clean. For these events, a 0.5 photoelectron threshold was used. There was no detectable cross-talk between the fibers.

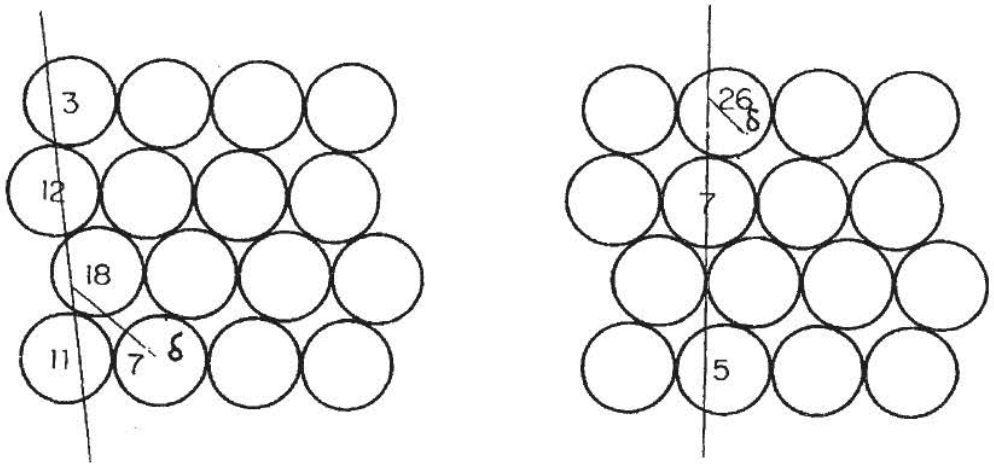

Figure A.19: Two unusual tracks, showing an excessive number of photoelectrons produced within a fiber or neighboring fibers, produced by the passage of minimum ionizing particles. Delta rays could produce these excess photoelectrons.

time is on the order of 5 ns, consistent with the 5 ns preamplifier rise time, indicating that a faster rise time may be obtainable, as the signals shown are limited by the preamplifier response.

A.5 Determination of Optimum 3HF Concentration

An experiment was performed to determine the optimum dopant concentration which should be used for a given scintillating fiber length and fiber diameter. We investigated 830μm diameter polystyrene fibers doped with 3HF. As one increases the concentration of 3HF the yield of primary photons also increases. However, the probability that a photon will be lost due to self-absorption as it travels down the fiber increases as well. Therefore, one must choose a dopant concentration which achieves an optimum balance between these two effects and, thus, maximizes the number of

Table A.2: The 3HF concentration which maximizes the light yield for each source position.

Source position (cm)	Y_{Max} (ppm)
15	1770
100	1540
200	1530
300	1440
380	1610

photons finally detected at the end of the fiber.

The experimental setup for this test is similar to the one described in section A.4.1. Three 4 meter long fiber ribbons were coupled to 2.5 meter long clear fiber light guides which were in turn coupled to VLPCs. There was no mirror coupled to the end of the fibers. Each fiber ribbon had a different 3HF concentration: 500, 1000 and 2000 ppm. The fibers were excited by 1 MeV gamma rays from a ^{60}Co source. The light yield for a given source position was measured as a function of dophant concentration. The source position was measured with respect to the distance from the splice point. Figure A.20 shows the light yield as a function of 3HF concentration for the source at five different positions. The points for each source position were fitted with a second order polynomial. The position of the curve maximum was taken to be the 3HF concentration which would maximize the light yield for a fiber length equal to the source position. Table A.2 shows the 3HF concentration (Y_{Max}) which maximizes the light yield for each source position.

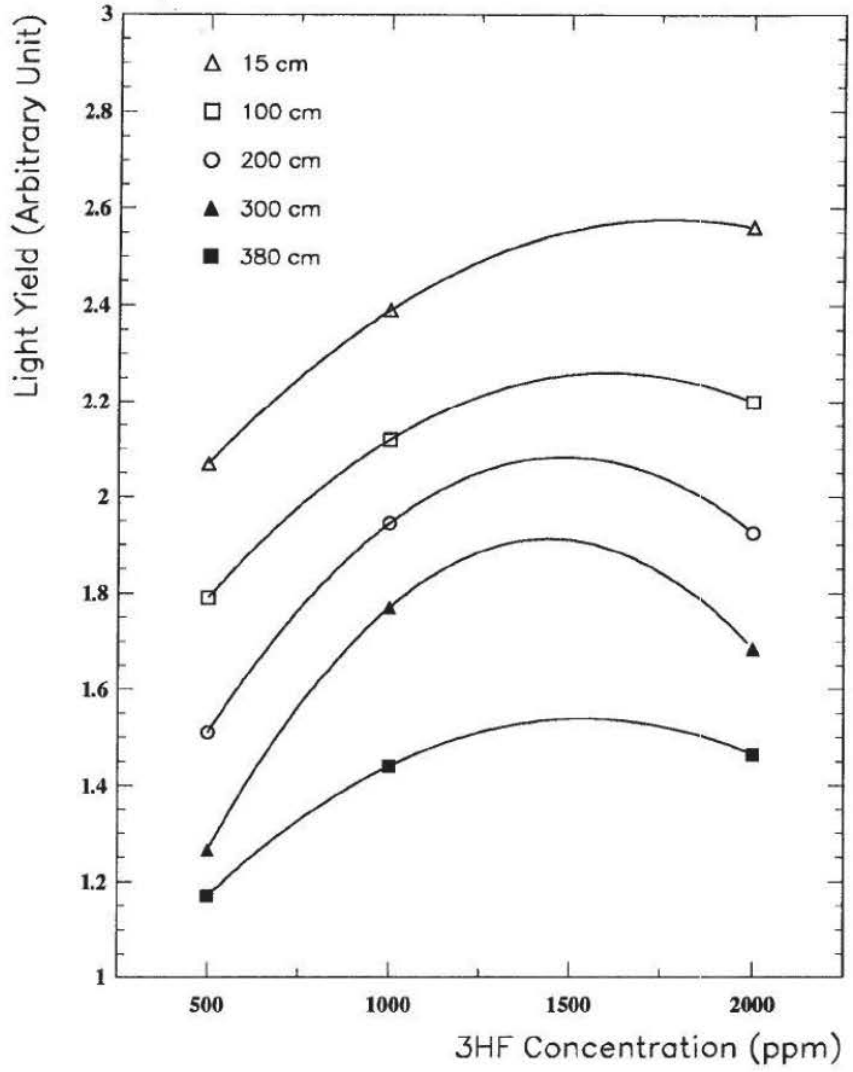

Figure A.20: Relative light yield as a function of 3HF concentration for 5 different source positions. The source position is measured with respect to the distance from the splice point. The maximum of each curve was taken to be the 3HF concentration which would maximize the light yield for a fiber length equal to the source position.

A.6 Conclusion

In these experiments with scintillating fibers and VLPCs we have demonstrated that one can efficiently record charged particle tracks using fibers of the length proposed for the SDC detector. In tests with cosmic rays, a 95% efficiency was achieved in one fiber layer when a hit was required in both neighboring layers. A 98.7% efficiency was observed when a hit was required in only one of the neighboring layer. In this same cosmic ray test, 6.2 photoelectrons were detected when the scintillator telescope was 6.5 m (4 m scintillating fiber + 2.5 m clear fiber light guide) from the VLPC. It was shown that one can easily operate 16 VLPC channels simultaneously. A common bias voltage of 6.5 V was used for all channels and a gain uniformity of 5% was observed. The VLPCs exhibited excellent time resolution. A rise time of 5 ns, consistent with the rise time of the preamplifier, was measured. Finally, the optimum 3HF concentration was determined for various lengths 830μm diameter fibers. The 3HF concentration which maximizes the light yield after 380 cm of scintillating fiber is 1610 ppm.

Bibliography

[1] The RD1 Collaboration, *RD1 - Scintillating Fiber Calorimetry*, **CERN PPE/93-22** (1993).

[2] P. Antich et al., Nucl. Instr. and Meth. **A297** (1990) 514.

[3] G.T. Reynolds and P.E. Condon, Rev. Sci. Instrum. **28** (1957) 1098;
G.T. Reynolds, IRE Trans. Nucl. Sci. **NS-7** (1960) 115.

[4] Solenoid Detector Collaboration, *Technical Design Report*,
SDC 92-201 (1992).

[5] A. Simon, *Scintillating Fiber Detectors in Particle Physics*, **CERN PPE/92-95** (1992).

[6] J. B. Birks, *The Theory and Practice of Scintillation Counting*, Pergammon Press (1964);
A.J. Davis et al. Nucl. Instr. and Meth. **A 276** (1989) 347.

[7] Th. Förster, Ann. Physik **2** (1948) 55;
R.K. Swank and W.L. Buck, Phys. Rev. **91** (1953) 927.

[8] C. D'Ambrosio et al., *Photoelectron Counting with Small Diameter Scintillating Fibers*, **CERN PPE/92-207** (1992).

[9] C. D'Ambrosio et al., Nucl. Instr. and Meth. **A306** (1991) 549.

[10] M.D. Petroff, M.G. Stapelbroek and W.A. Kleinhans, Appl. Phys. Lett. **Vol. 51**, No. 6 (1987) 406.

[11] M.D. Petroff and W.G. Stapelbroek, IEEE Trans. Nucl. Sci. N.S. **36** (1989) 158;
M.D. Petroff and M. Atac, IEEE Trans. Nucl. Sci. N.S. **36** (1989) 163.

[12] M. Atac et al., Nucl. Instr. and Meth. **A314** (1992) 56.

[13] M. Atac et al., Nucl. Instr. and Meth. **A320** (1992) 155.

[14] R.J. Yarema, T. Zimmerman, W. Willams, M. Binkley, T. Huffman, R. Wagner, IEEE Nucl. Sci. Symposium (1991).

Appendix B

Total punchthrough probability numerical results

The tables below contain the results of measurements of the total punchthrough probability of hadronic showers as a function of absorber depth. These are the results after all know muon backgrounds have been subtracted. The error is the sum of the statistical error and an additional error reflecting an uncertainty in subtracting the muon background. The results below have not been corrected for the detector acceptance.

Table B.1: Total punchthrough probability of 10, 20, 30 and 50 GeV/c negative pions, magnet M1 off.

Iron eq. (m)	10 GeV/c	20 GeV/c	30 GeV/c	50 GeV/c
0.15	0.99978 ±0.00006	0.9967 ±0.0002	0.9984 ±0.0001	0.99993 ±0.00003
0.19	0.9921 ±0.0004	0.9922 ±0.0003	0.9952 ±0.0002	0.99985 ±0.00005
0.23	0.9769 ±0.0006	0.9851 ±0.0004	0.9919 ±0.0003	0.9992 ±0.0001
0.27	0.9537 ±0.0009	0.9745 ±0.0006	0.9871 ±0.0003	0.9983 ±0.0002
0.31	0.926 ±0.001	0.9619 ±0.0008	0.9812 ±0.0004	0.9971 ±0.0002
0.35	0.890 ±0.001	0.9483 ±0.0009	0.9747 ±0.0005	0.9943 ±0.0003
0.39	0.843 ±0.002	0.929 ±0.001	0.9656 ±0.0006	0.9908 ±0.0004
0.43	0.783 ±0.002	0.900 ±0.001	0.9503 ±0.0007	0.9856 ±0.0004
0.47	0.733 ±0.002	0.870 ±0.001	0.9324 ±0.0008	0.9788 ±0.0005
0.51	0.669 ±0.003	0.829 ±0.002	0.9071 ±0.0009	0.9686 ±0.0006
0.55	0.600 ±0.003	0.784 ±0.002	0.878 ±0.001	0.9567 ±0.0007
0.59	0.532 ±0.003	0.728 ±0.002	0.836 ±0.001	0.9366 ±0.0009
0.63	0.470 ±0.004	0.670 ±0.002	0.787 ±0.001	0.906 ±0.001
0.71	0.395 ±0.004	0.596 ±0.002	0.723 ±0.001	0.864 ±0.001
0.79	0.333 ±0.004	0.526 ±0.002	0.656 ±0.002	0.812 ±0.001
0.87	0.270 ±0.005	0.443 ±0.002	0.568 ±0.002	0.730 ±0.002
0.95	0.201 ±0.005	0.350 ±0.002	0.466 ±0.002	0.631 ±0.002
1.03	0.126 ±0.005	0.246 ±0.002	0.351 ±0.002	0.515 ±0.002
1.11	0.090 ±0.006	0.188 ±0.002	0.278 ±0.001	0.428 ±0.002
1.19	0.071 ±0.006	0.153 ±0.001	0.232 ±0.001	0.367 ±0.002
1.27	0.051 ±0.006	0.114 ±0.001	0.178 ±0.001	0.295 ±0.002
1.35	0.036 ±0.006	0.081 ±0.001	0.133 ±0.001	0.230 ±0.002
1.43	0.029 ±0.006	0.064 ±0.001	0.1061 ±0.0010	0.187 ±0.001
1.51	0.021 ±0.006	0.0459 ±0.0009	0.0790 ±0.0009	0.144 ±0.001
1.59	0.013 ±0.006	0.0260 ±0.0007	0.0470 ±0.0007	0.092 ±0.001
1.69		0.0153 ±0.0002	0.0291 ±0.0002	0.0673 ±0.0003
2.29		0.00296 ±0.00008	0.00602 ±0.00010	0.0141 ±0.0002
2.89		0.00096 ±0.00005	0.00177 ±0.00006	0.0039 ±0.0001
3.49		0.00050 ±0.00004	0.00086 ±0.00005	0.00171 ±0.00008
5.29		0.00013 ±0.00003	0.00036 ±0.00005	0.00061 ±0.00007

Table B.2: Total punchthrough probability of 10, 20, 30 and 50 GeV/c negative pions, M1 field 3 T.

Iron eq. (m)	10 GeV/c	20 GeV/c	30 GeV/c	50 GeV/c
0.15	0.9993 ±0.0001	0.99981 ±0.00005	0.9965 ±0.0002	0.99997 ±0.00002
0.19	0.9944 ±0.0003	0.9942 ±0.0003	0.9937 ±0.0003	0.9990 ±0.0001
0.23	0.9803 ±0.0006	0.9846 ±0.0004	0.9898 ±0.0004	0.9978 ±0.0002
0.27	0.9584 ±0.0009	0.9695 ±0.0006	0.9842 ±0.0004	0.9962 ±0.0002
0.31	0.932 ±0.001	0.9523 ±0.0008	0.9774 ±0.0005	0.9944 ±0.0003
0.35	0.892 ±0.001	0.9347 ±0.0009	0.9690 ±0.0006	0.9921 ±0.0003
0.39	0.838 ±0.002	0.909 ±0.001	0.9571 ±0.0007	0.9886 ±0.0004
0.43	0.774 ±0.002	0.874 ±0.001	0.9383 ±0.0008	0.9830 ±0.0005
0.47	0.718 ±0.002	0.839 ±0.001	0.9165 ±0.0010	0.9746 ±0.0006
0.51	0.649 ±0.002	0.792 ±0.001	0.887 ±0.001	0.9619 ±0.0007
0.55	0.573 ±0.002	0.739 ±0.002	0.852 ±0.001	0.9468 ±0.0008
0.59	0.500 ±0.002	0.679 ±0.002	0.807 ±0.001	0.9234 ±0.0010
0.63	0.437 ±0.002	0.618 ±0.002	0.754 ±0.002	0.893 ±0.001
0.71	0.361 ±0.002	0.540 ±0.002	0.685 ±0.002	0.854 ±0.001
0.79	0.298 ±0.002	0.469 ±0.002	0.615 ±0.002	0.812 ±0.001
0.87	0.236 ±0.002	0.388 ±0.002	0.526 ±0.002	0.719 ±0.002
0.95	0.169 ±0.002	0.298 ±0.002	0.425 ±0.002	0.609 ±0.002
1.03	0.098 ±0.002	0.197 ±0.002	0.311 ±0.002	0.482 ±0.002
1.11	0.065 ±0.002	0.143 ±0.002	0.244 ±0.002	0.394 ±0.002
1.19	0.047 ±0.002	0.110 ±0.002	0.202 ±0.001	0.330 ±0.002
1.27	0.027 ±0.002	0.071 ±0.002	0.154 ±0.001	0.253 ±0.002
1.35	0.016 ±0.002	0.049 ±0.002	0.113 ±0.001	0.201 ±0.001
1.43	0.010 ±0.002	0.036 ±0.002	0.088 ±0.001	0.163 ±0.001
1.51		0.022 ±0.002	0.0644 ±0.0009	0.124 ±0.001
1.59			0.0357 ±0.0007	0.0767 ±0.0010
1.69			0.0197 ±0.0005	0.0527 ±0.0003
2.29			0.0027 ±0.0003	0.0105 ±0.0002
2.89				0.0021 ±0.0001
3.49				0.00076 ±0.00009
5.29				0.00020 ±0.00008

Table B.3: Total punchthrough probability of 100, 200 and 300 GeV/c negative pions, magnet M1 off.

Iron eq. (m)	100 GeV/c	200 GeV/c	300 GeV/c
0.15	0.99956 ±0.00007	1.000000±0.000001	0.99997 ±0.00003
0.19	0.99931 ±0.00008	0.99997 ±0.00003	0.99997 ±0.00003
0.23	0.99903 ±0.00010	0.99987 ±0.00006	0.99995 ±0.00004
0.27	0.9981 ±0.0001	0.99979 ±0.00008	0.99987 ±0.00006
0.31	0.9968 ±0.0002	0.9995 ±0.0001	0.99970 ±0.00009
0.35	0.9955 ±0.0002	0.9993 ±0.0001	0.9995 ±0.0001
0.39	0.9936 ±0.0002	0.9991 ±0.0002	0.9993 ±0.0001
0.43	0.9903 ±0.0003	0.9987 ±0.0002	0.9990 ±0.0002
0.47	0.9871 ±0.0003	0.9982 ±0.0002	0.9988 ±0.0002
0.51	0.9836 ±0.0004	0.9975 ±0.0003	0.9984 ±0.0002
0.55	0.9800 ±0.0004	0.9968 ±0.0003	0.9980 ±0.0002
0.59	0.9723 ±0.0005	0.9947 ±0.0004	0.9975 ±0.0003
0.63	0.9646 ±0.0006	0.9926 ±0.0005	0.9967 ±0.0003
0.71	0.9323 ±0.0008	0.9904 ±0.0005	0.9954 ±0.0004
0.79	0.9001 ±0.0009	0.9807 ±0.0007	0.9929 ±0.0005
0.87	0.855 ±0.001	0.964 ±0.001	0.9854 ±0.0007
0.95	0.809 ±0.001	0.947 ±0.001	0.9744 ±0.0009
1.03	0.744 ±0.001	0.920 ±0.001	0.959 ±0.001
1.11	0.657 ±0.001	0.894 ±0.002	0.931 ±0.001
1.19	0.571 ±0.002	0.839 ±0.002	0.895 ±0.002
1.27	0.486 ±0.002	0.769 ±0.002	0.845 ±0.002
1.35	0.403 ±0.002	0.678 ±0.003	0.776 ±0.002
1.43	0.332 ±0.001	0.593 ±0.003	0.694 ±0.003
1.51	0.262 ±0.001	0.509 ±0.003	0.611 ±0.003
1.59	0.182 ±0.001	0.387 ±0.003	0.499 ±0.003
1.69	0.1215 ±0.0005	0.291 ±0.002	0.430 ±0.002
2.29	0.0282 ±0.0003	0.075 ±0.001	0.123 ±0.001
2.89	0.0086 ±0.0001	0.0194 ±0.0007	0.0324 ±0.0008
3.49	0.0041 ±0.0001	0.0071 ±0.0006	0.0126 ±0.0007
5.29	0.00227 ±0.00009	0.0030 ±0.0006	0.0055 ±0.0006

Table B.4: Total punchthrough probability of 100, 200 and 300 GeV/c negative pions, M1 field 3 T.

Iron eq. (m)	100 GeV/c	200 GeV/c	300 GeV/c
0.15	0.99975 ±0.00007	0.99984 ±0.00006	1.000000±0.000001
0.19	0.9995 ±0.0001	0.99972 ±0.00008	1.000000±0.000001
0.23	0.9990 ±0.0001	0.9995 ±0.0001	0.99998 ±0.00003
0.27	0.9982 ±0.0002	0.9991 ±0.0001	0.99991 ±0.00005
0.31	0.9974 ±0.0002	0.9987 ±0.0002	0.99979 ±0.00007
0.35	0.9966 ±0.0002	0.9983 ±0.0002	0.99968 ±0.00009
0.39	0.9953 ±0.0003	0.9978 ±0.0002	0.9995 ±0.0001
0.43	0.9939 ±0.0003	0.9970 ±0.0002	0.9994 ±0.0001
0.47	0.9918 ±0.0004	0.9964 ±0.0003	0.9992 ±0.0001
0.51	0.9885 ±0.0005	0.9954 ±0.0003	0.9988 ±0.0002
0.55	0.9852 ±0.0005	0.9945 ±0.0003	0.9984 ±0.0002
0.59	0.9762 ±0.0007	0.9921 ±0.0004	0.9981 ±0.0002
0.63	0.9655 ±0.0008	0.9893 ±0.0005	0.9970 ±0.0003
0.71	0.9465 ±0.0010	0.9843 ±0.0006	0.9955 ±0.0003
0.79	0.898 ±0.001	0.9711 ±0.0008	0.9929 ±0.0004
0.87	0.850 ±0.002	0.9534 ±0.0010	0.9845 ±0.0006
0.95	0.781 ±0.002	0.926 ±0.001	0.9718 ±0.0008
1.03	0.709 ±0.002	0.889 ±0.001	0.953 ±0.001
1.11	0.660 ±0.002	0.856 ±0.002	0.925 ±0.001
1.19	0.580 ±0.002	0.794 ±0.002	0.886 ±0.002
1.27	0.485 ±0.002	0.717 ±0.002	0.830 ±0.002
1.35	0.389 ±0.002	0.622 ±0.002	0.768 ±0.002
1.43	0.324 ±0.002	0.538 ±0.002	0.689 ±0.002
1.51	0.257 ±0.002	0.452 ±0.002	0.610 ±0.002
1.59	0.164 ±0.002	0.323 ±0.002	0.491 ±0.003
1.69	0.1035 ±0.0006	0.227 ±0.001	0.377 ±0.002
2.29	0.0236 ±0.0003	0.0576 ±0.0008	0.108 ±0.002
2.89	0.0057 ±0.0002	0.0140 ±0.0006	0.0257 ±0.0008
3.49	0.0023 ±0.0001	0.0054 ±0.0006	0.0081 ±0.0005
5.29	0.0008 ±0.0001	0.0023 ±0.0006	0.0027 ±0.0004

Table B.5: Total punchthrough probability of 30, 100 and 300 GeV/c positive pions, magnet M1 off.

Iron eq. (m)	30 GeV/c	100 GeV/c	300 GeV/c
0.15	0.99933 ±0.00009	0.99999 ±0.00002	0.999999±0.000003
0.19	0.9976 ±0.0002	0.99947 ±0.00009	0.999999±0.000004
0.23	0.9950 ±0.0002	0.9981 ±0.0002	0.99997 ±0.00002
0.27	0.9911 ±0.0003	0.9964 ±0.0002	0.99994 ±0.00004
0.31	0.9861 ±0.0004	0.9949 ±0.0003	0.99983 ±0.00006
0.35	0.9800 ±0.0005	0.9939 ±0.0003	0.99965 ±0.00008
0.39	0.9707 ±0.0006	0.9928 ±0.0003	0.9994 ±0.0001
0.43	0.9558 ±0.0007	0.9917 ±0.0004	0.9992 ±0.0001
0.47	0.9383 ±0.0008	0.9905 ±0.0004	0.9991 ±0.0001
0.51	0.9131 ±0.0010	0.9886 ±0.0004	0.9988 ±0.0001
0.55	0.884 ±0.001	0.9864 ±0.0004	0.9985 ±0.0002
0.59	0.843 ±0.001	0.9825 ±0.0005	0.9981 ±0.0002
0.63	0.794 ±0.001	0.9743 ±0.0006	0.9972 ±0.0002
0.71	0.730 ±0.002	0.9617 ±0.0007	0.9959 ±0.0003
0.79	0.662 ±0.002	0.9403 ±0.0009	0.9934 ±0.0003
0.87	0.574 ±0.002	0.895 ±0.001	0.9861 ±0.0005
0.95	0.471 ±0.002	0.833 ±0.001	0.9748 ±0.0007
1.03	0.355 ±0.002	0.754 ±0.002	0.9581 ±0.0009
1.11	0.280 ±0.002	0.674 ±0.002	0.932 ±0.001
1.19	0.234 ±0.001	0.606 ±0.002	0.897 ±0.001
1.27	0.180 ±0.001	0.519 ±0.002	0.848 ±0.002
1.35	0.135 ±0.001	0.429 ±0.002	0.779 ±0.002
1.43	0.108 ±0.001	0.358 ±0.002	0.698 ±0.002
1.51	0.0807 ±0.0009	0.287 ±0.002	0.618 ±0.002
1.59	0.0490 ±0.0007	0.198 ±0.002	0.505 ±0.002
1.69	0.0307 ±0.0002	0.1373 ±0.0007	0.427 ±0.001
2.29	0.00642 ±0.00008	0.0298 ±0.0004	0.120 ±0.001
2.89	0.00176 ±0.00006	0.0076 ±0.0002	0.0323 ±0.0007
3.49	0.00081 ±0.00005	0.0033 ±0.0001	0.0123 ±0.0006
5.29	0.00037 ±0.00004	0.0016 ±0.0001	0.0052 ±0.0005

Table B.6: Total punchthrough probability of 30, 100 and 300 GeV/c positive pions, M1 field 3 T.

Iron eq. (m)	30 GeV/c	100 GeV/c	300 GeV/c
0.15	0.9987 ±0.0001	0.99984 ±0.00007	1.000000±0.000001
0.19	0.9971 ±0.0002	0.9994 ±0.0001	1.000000±0.000002
0.23	0.9942 ±0.0003	0.9987 ±0.0002	0.99999 ±0.00002
0.27	0.9895 ±0.0004	0.9977 ±0.0003	0.99994 ±0.00004
0.31	0.9834 ±0.0004	0.9969 ±0.0003	0.99976 ±0.00008
0.35	0.9763 ±0.0005	0.9960 ±0.0003	0.99965 ±0.00009
0.39	0.9652 ±0.0006	0.9947 ±0.0004	0.9995 ±0.0001
0.43	0.9485 ±0.0008	0.9935 ±0.0004	0.9992 ±0.0001
0.47	0.9277 ±0.0009	0.9918 ±0.0005	0.9989 ±0.0002
0.51	0.899 ±0.001	0.9893 ±0.0006	0.9987 ±0.0002
0.55	0.865 ±0.001	0.9864 ±0.0006	0.9983 ±0.0002
0.59	0.822 ±0.001	0.9806 ±0.0007	0.9978 ±0.0002
0.63	0.771 ±0.001	0.9697 ±0.0009	0.9969 ±0.0003
0.71	0.703 ±0.002	0.954 ±0.001	0.9956 ±0.0003
0.79	0.634 ±0.002	0.927 ±0.001	0.9931 ±0.0004
0.87	0.546 ±0.002	0.871 ±0.002	0.9855 ±0.0006
0.95	0.443 ±0.002	0.801 ±0.002	0.9736 ±0.0008
1.03	0.328 ±0.002	0.716 ±0.002	0.956 ±0.001
1.11	0.257 ±0.002	0.635 ±0.003	0.929 ±0.001
1.19	0.209 ±0.001	0.567 ±0.003	0.894 ±0.002
1.27	0.154 ±0.001	0.483 ±0.003	0.844 ±0.002
1.35	0.118 ±0.001	0.398 ±0.003	0.775 ±0.002
1.43	0.094 ±0.001	0.330 ±0.003	0.692 ±0.002
1.51	0.0695 ±0.0009	0.261 ±0.002	0.608 ±0.002
1.59	0.0399 ±0.0007	0.173 ±0.002	0.487 ±0.002
1.69	0.0275 ±0.0002	0.1099 ±0.0009	0.391 ±0.002
2.29	0.00498 ±0.00009	0.0232 ±0.0005	0.112 ±0.001
2.89	0.00104 ±0.00006	0.0051 ±0.0003	0.0262 ±0.0007
3.49	0.00048 ±0.00006	0.0017 ±0.0003	0.0084 ±0.0005
5.29	0.00013 ±0.00005	0.0005 ±0.0002	0.0028 ±0.0005

Table B.7: Total punchthrough probability of 100 GeV/c positive kaons and 100 and 300 GeV/c protons, magnet M1 off.

Iron eq. (m)	100 GeV/c K^+	100 GeV/c proton	300 GeV/c proton
0.15	0.99994 ±0.00004	0.999999±0.000005	1.000000±0.000002
0.19	0.99974 ±0.00008	0.999999±0.000005	1.000000±0.000002
0.23	0.9994 ±0.0001	0.999999±0.000005	0.99999 ±0.00002
0.27	0.9989 ±0.0002	0.999999±0.000005	0.99997 ±0.00003
0.31	0.9984 ±0.0002	0.99999 ±0.00001	0.99997 ±0.00003
0.35	0.9980 ±0.0002	0.99997 ±0.00002	0.99997 ±0.00003
0.39	0.9976 ±0.0002	0.99995 ±0.00003	0.99997 ±0.00003
0.43	0.9970 ±0.0003	0.99987 ±0.00004	0.99997 ±0.00003
0.47	0.9964 ±0.0003	0.99956 ±0.00008	0.99995 ±0.00004
0.51	0.9952 ±0.0003	0.9990 ±0.0001	0.99993 ±0.00005
0.55	0.9940 ±0.0004	0.9982 ±0.0002	0.99990 ±0.00006
0.59	0.9886 ±0.0005	0.9960 ±0.0002	0.99988 ±0.00006
0.63	0.9833 ±0.0007	0.9901 ±0.0004	0.99980 ±0.00008
0.71	0.9779 ±0.0007	0.9805 ±0.0005	0.9996 ±0.0001
0.79	0.953 ±0.001	0.9614 ±0.0007	0.9986 ±0.0002
0.87	0.918 ±0.001	0.915 ±0.001	0.9936 ±0.0005
0.95	0.882 ±0.002	0.853 ±0.001	0.9855 ±0.0007
1.03	0.831 ±0.002	0.772 ±0.002	0.9731 ±0.0009
1.11	0.790 ±0.002	0.686 ±0.002	0.947 ±0.001
1.19	0.715 ±0.002	0.609 ±0.002	0.912 ±0.002
1.27	0.620 ±0.002	0.508 ±0.002	0.862 ±0.002
1.35	0.525 ±0.003	0.426 ±0.002	0.789 ±0.002
1.43	0.451 ±0.003	0.356 ±0.002	0.705 ±0.003
1.51	0.376 ±0.002	0.287 ±0.002	0.621 ±0.003
1.59	0.269 ±0.002	0.199 ±0.002	0.506 ±0.003
1.69	0.197 ±0.001	0.141 ±0.001	0.390 ±0.003
2.29	0.0521 ±0.0007	0.0298 ±0.0007	0.099 ±0.002
2.89	0.0150 ±0.0004	0.0073 ±0.0003	0.0274 ±0.0009
3.49	0.0068 ±0.0003	0.0030 ±0.0002	0.0119 ±0.0006
5.29	0.0040 ±0.0002	0.0013 ±0.0001	0.0061 ±0.0004

Table B.8: Total punchthrough probability of 100 GeV/c positive kaons and 100 and 300 GeV/c protons, M1 field 3 T.

Iron eq. (m)	100 GeV/c K^+	100 GeV/c proton	300 GeV/c proton
0.15	0.99978 ±0.00007	1.000000±0.000001	0.99998 ±0.00002
0.19	0.99955 ±0.00009	1.000000±0.000001	0.99998 ±0.00002
0.23	0.9992 ±0.0001	1.000000±0.000002	0.99998 ±0.00002
0.27	0.9987 ±0.0002	0.99998 ±0.00002	0.99998 ±0.00002
0.31	0.9984 ±0.0002	0.99997 ±0.00003	0.99998 ±0.00002
0.35	0.9980 ±0.0002	0.99994 ±0.00004	0.99998 ±0.00002
0.39	0.9975 ±0.0002	0.99986 ±0.00006	0.99998 ±0.00002
0.43	0.9970 ±0.0002	0.9995 ±0.0001	0.99996 ±0.00003
0.47	0.9961 ±0.0003	0.9990 ±0.0001	0.99996 ±0.00003
0.51	0.9946 ±0.0003	0.9980 ±0.0002	0.99995 ±0.00003
0.55	0.9930 ±0.0004	0.9968 ±0.0003	0.99994 ±0.00004
0.59	0.9851 ±0.0005	0.9935 ±0.0004	0.99993 ±0.00004
0.63	0.9772 ±0.0007	0.9852 ±0.0006	0.99979 ±0.00007
0.71	0.9694 ±0.0008	0.9726 ±0.0008	0.9995 ±0.0001
0.79	0.937 ±0.001	0.947 ±0.001	0.9987 ±0.0002
0.87	0.894 ±0.001	0.892 ±0.001	0.9929 ±0.0004
0.95	0.851 ±0.002	0.822 ±0.002	0.9830 ±0.0006
1.03	0.795 ±0.002	0.734 ±0.002	0.9678 ±0.0009
1.11	0.753 ±0.002	0.647 ±0.002	0.940 ±0.001
1.19	0.675 ±0.002	0.574 ±0.002	0.901 ±0.001
1.27	0.581 ±0.002	0.483 ±0.002	0.846 ±0.002
1.35	0.488 ±0.002	0.392 ±0.002	0.769 ±0.002
1.43	0.415 ±0.002	0.321 ±0.002	0.678 ±0.002
1.51	0.341 ±0.002	0.250 ±0.002	0.587 ±0.002
1.59	0.232 ±0.002	0.160 ±0.002	0.456 ±0.002
1.69	0.1637 ±0.0008	0.105 ±0.001	0.340 ±0.002
2.29	0.0431 ±0.0005	0.0188 ±0.0006	0.085 ±0.001
2.89	0.0112 ±0.0003	0.0036 ±0.0003	0.0197 ±0.0007
3.49	0.0049 ±0.0002	0.0014 ±0.0002	0.0079 ±0.0004
5.29	0.0028 ±0.0001	0.0005 ±0.0001	0.0036 ±0.0003

Table B.9: Total punchthrough probability of 30, 100 and 300 GeV/c negative pions and 100 GeV/c positive pions, M1 field 1.5 T

Iron eq. (m)	30 GeV/c π^-	100 GeV/c π^-	300 GeV/c π^-	100 GeV/c π^+
0.15	0.9969 ±0.0002	0.99992 ±0.00003	0.99998 ±0.00003	0.9990 ±0.0001
0.19	0.9939 ±0.0003	0.99977 ±0.00006	0.99997 ±0.00003	0.9965 ±0.0002
0.23	0.9901 ±0.0004	0.99946 ±0.00009	0.99987 ±0.00006	0.9926 ±0.0003
0.27	0.9846 ±0.0004	0.9989 ±0.0001	0.99965 ±0.00010	0.9880 ±0.0004
0.31	0.9779 ±0.0005	0.9983 ±0.0001	0.9994 ±0.0001	0.9852 ±0.0005
0.35	0.9705 ±0.0006	0.9976 ±0.0002	0.9992 ±0.0001	0.9838 ±0.0005
0.39	0.9595 ±0.0007	0.9967 ±0.0002	0.9989 ±0.0002	0.9820 ±0.0005
0.43	0.9423 ±0.0008	0.9955 ±0.0002	0.9987 ±0.0002	0.9803 ±0.0005
0.47	0.9224 ±0.0009	0.9940 ±0.0003	0.9984 ±0.0002	0.9786 ±0.0006
0.51	0.894 ±0.001	0.9914 ±0.0003	0.9979 ±0.0002	0.9760 ±0.0006
0.55	0.861 ±0.001	0.9887 ±0.0004	0.9974 ±0.0003	0.9733 ±0.0006
0.59	0.818 ±0.001	0.9813 ±0.0005	0.9965 ±0.0003	0.9662 ±0.0007
0.63	0.767 ±0.001	0.9723 ±0.0006	0.9954 ±0.0004	0.9576 ±0.0008
0.71	0.701 ±0.002	0.9564 ±0.0007	0.9937 ±0.0004	0.9422 ±0.0009
0.79	0.632 ±0.002	0.915 ±0.001	0.9892 ±0.0005	0.902 ±0.001
0.87	0.544 ±0.002	0.871 ±0.001	0.9828 ±0.0007	0.860 ±0.001
0.95	0.443 ±0.002	0.806 ±0.001	0.9715 ±0.0009	0.798 ±0.002
1.03	0.329 ±0.002	0.739 ±0.002	0.954 ±0.001	0.733 ±0.002
1.11	0.260 ±0.002	0.691 ±0.002	0.938 ±0.001	0.686 ±0.002
1.19	0.216 ±0.001	0.610 ±0.002	0.900 ±0.002	0.606 ±0.002
1.27	0.166 ±0.001	0.516 ±0.002	0.850 ±0.002	0.510 ±0.002
1.35	0.124 ±0.001	0.417 ±0.002	0.777 ±0.002	0.419 ±0.002
1.43	0.097 ±0.001	0.349 ±0.002	0.696 ±0.002	0.352 ±0.002
1.51	0.0719 ±0.0009	0.280 ±0.002	0.614 ±0.003	0.284 ±0.002
1.59	0.0423 ±0.0007	0.186 ±0.001	0.485 ±0.003	0.191 ±0.002
1.69	0.0236 ±0.0002	0.1224 ±0.0006	0.391 ±0.001	0.1206 ±0.0009
2.29	0.0047 ±0.0001	0.0283 ±0.0003	0.108 ±0.001	0.0276 ±0.0005
2.89	0.0016 ±0.0001	0.0077 ±0.0002	0.0278 ±0.0006	0.0076 ±0.0003
3.49	0.0009 ±0.0001	0.0036 ±0.0002	0.0104 ±0.0004	0.0038 ±0.0002
5.29	0.00043 ±0.00010	0.0015 ±0.0001	0.0040 ±0.0003	0.0020 ±0.0002